Numéro d'ordre : 2016LYSEC23 Année : 2016

THÈSE DE DOCTORAT DE
l'ECOLE CENTRALE DE LYON

Spécialité

Mécanique

École doctorale Mécanique, Energétique, Génie Civil et Acoustique (Lyon)

Présentée par:

Clara OLIVER SERNA

Pour obtenir le grade de

DOCTEUR de l'ECOLE CENTRALE DE LYON

Sujet de la thèse :

Vibroacoustic analysis of car door and window seals.

Soutenue publiquement le 6 septembre 2016 devant le jury composé de:

Zouhir Abbadi	Docteur, Groupe PSA Vélizy-Villacoublay	Examinateur
Christophe BaillY	Professeur, École Centrale de Lyon - LMFA	Président
Sébastien Besset	MCf HDR, École Centrale de Lyon - LTDS	Co-encadrant
Louis Jézéquel	Professeur, École Centrale de Lyon - LTDS	Directeur de thèse
Antoine Legay	MCf HDR, CNAM, Paris - LMSSC	Rapporteur
Charles Pézerat	Professeur, Université du Maine, Le Mans LAUM	Rapporteur
François Van Herpe	Docteur, Groupe PSA Vélizy-Villacoublay	Examinateur

Al pare.

Remerciements

J'aimerais tout d'abord remercier mon directeur de thèse Louis Jézéquel, qui m'a accueilli dans son laboratoire, non seulement pendant mes trois années de thèse, mais aussi pendant l'année et demie précédente. Je vous remercie de m'avoir trouvé d'abord un stage, puis un CDD et finalement ce sujet de thèse, avec lequel j'ai pu grandir professionnellement. J'aimerais également remercier mon autre encadrant, Sebastien Besset, pour sa disponibilité et son implication pendant ces années. Merci d'abord pour ta patience lors de mes questions, malgré ma difficulté à les exprimer dans quelque chose qui ressemble à la langue française, et merci pour le temps que tu à pris pour m'expliquer les réponses. Ton soutien scientifique, ta pédagogie et ta bonne humeur ont été indispensables pour la réussite de cette thèse. Je tiens à remercier ensuite les responsables de mon encadrement industriel, François Van Herpe et Zouhir Abbadi. Merci pour votre disponibilité, même si télématique, votre support moral, et vos efforts pour trouver des solutions à mes problèmes scientifiques ou administratifs. Merci aussi pour le temps passé à corriger tous mes documents, la tâche à dû s'avérer pénible parfois. Je suis donc très contente d'avoir pu travailler en équipe avec vous.

Je tiens également à remercier Bernard Jean-Pierre et Stéphane Lemahieu, sans leur savoir-faire et leur disponibilité, la partie expérimentale de ma thèse n'aurait pas été possible. Ainsi, je remercie Isabelle Tixier pour son temps et son professionnalisme lors de toutes mes démarches administratives. Enfin, je tiens à remercier Olivier Dessombz pour son aide pour la résolution de mes problèmes informatiques hebdomadaires, sa patience, et sa bonne humeur.

D'un coté plus personnel, j'aimerais remercier tous les maîtres de conférence, techniciens, personnel administratif, doctorants et post-doctorants de l'équipe Dysco/D2S pour m'avoir offert cette ambiance légère et fun, qui a rendu les journées de travail plus agréables. J'aimerais remercier ensuite tous mes copains du LTDS: de l'aquarium, du G8 et du coin repas du H10. C'est de vous que je garde le meilleur souvenir, des blagues à répétition, des débats philosophiques sans conclusion, des cafés interminables et des moments à pleurer de rire. Je vous remercie pour votre accueil, votre patience à attendre que j'arrive à m'exprimer, et votre aide, ainsi que pour les bons moments qu'on à passé lors des soirées, les repas et les barbecues. C'est pour cela que je tiens à envoyer mes remerciements les plus chaleureux à Irene V., Pierre G., Alexia C., Stéphanie L., Paula U., Alexa D., Colas J., Kevin S., Antoine G., Adalberto P., Josselin P., Marième F., Istvan J., Guillaume D., Jérôme L., Xingrong H., Rita T., Christophe D., Adrien M., Antoine M., Nicolas G., Cécile D.,

Laura G. et David L.

Un remerciement particulier à Irene, pour toutes les pauses café, toutes les soirées gourmandes et pour son amitié en générale. Merci pour ta générosité, ton énergie et ta bonne humeur. Tu as été une partie importante de ma vie en France, et je suis très heureuse d'avoir pu partager ces moments avec toi.

Je ne veux pas oublier mon frère de thèse, Pierre, qui m'a accueilli même quand je ne disais pas bonjour le matin. Je te remercie pour ton aide pendant ces 3 années de thèse, pour ton répertoire de blagues et vidéos, et pour mon apprentissage du français correct. Tu as été vraiment attentif avec moi, et j'en garderai toujours le souvenir.

Un remerciement particulier aussi a mes copines de la course, Stéphanie et Alexia, sans qui mes journées auraient été beaucoup plus longues. Le repas à midi ou le café avec vous à été souvent le meilleur de ma journée au labo. Merci pour écouter mes plaintes pendant les jours les plus difficiles, et pour vos mots gentils pour adoucir mon chagrin. Merci aussi pour nos moments de rigolade ou des discussions complices. Je suis seulement désolée de ne vous avoir pas rencontré un peu plus tôt.

Je ne pourrais pas poursuivre sans remercier du fond du cœur la personne la plus importante avec laquelle j'ai partagé ces dernières années, Antoine. Tu as été ma famille ici, mon soutien au quotidien, et je n'aurais pas pu m'embarquer dans cette aventure sans toi. Merci d'avoir supporté ma mauvaise humeur, et de tous les efforts que je sais que tu as fait pour me rendre plus heureuse.

Merci également à ta famille, qui m'a accueilli comme si j'étais une des leurs depuis le premier moment, qui s'est intéressée à moi et qui m'a apporté son support moral tout au long de ces dernières années.

Enfin, je ne pourrais pas conclure ces remerciements sans un mot pour ma famille. Ma mère, mon père, Albert et Alba, qui se sont intéressés à moi au quotidien, même quand mon quotidien n'était pas très intéressant. Qui m'ont soutenu comme ils ont pu, à distance. Je sais que pour vous aussi ça été difficile. Mais c'est grâce à votre support inconditionnel, à nos coups de fil ou messages, et a nos rencontres tous les quelques mois que j'ai pu terminer cette thèse.

Ici, je veux quand même rajouter un petit texte pour la personne à qui je dois le tout de cette thèse: Mon père. Tu m'as tout appris dans la vie, mais particulièrement tu m'as transmis cette curiosité pour comprendre, celle qui m'a poussé vers le monde scientifique, et celle grâce à laquelle j'écris ce manuscrit aujourd'hui. Ton soutien constant, dans ma vie comme dans ma carrière professionnelle, ont été indispensables pour ma réussite. Cette thèse est donc, pour toi. Gràcies.

Résumé

Les joints de porte et de vitrage des voitures jouent un rôle très important dans la réduction du bruit d'origine aérodynamique, à la fois par transmission directe et de par son rôle en tant que condition limite des autres éléments transmetteurs (portes et fenêtres). Par conséquent, sa conception est fondamentale pour l'optimisation du confort de passager. Néanmoins, la méthode traditionnelle pour sa conception, basée sur une approche par tâtonnement de tests en soufflerie, est très couteuse et insuffisante. Une approche différente est envisagée dans ce manuscrit, par la création d'un modèle capable de prédire la transmission du bruit jusqu'à la cavité du véhicule, qui puisse être appliqué ultérieurement dans une routine d'optimisation.

La modélisation des joints de vitrage et des fenêtres fait face à plusieurs difficultés. La fermeture de la porte subie par le joint de porte avant d'être soumis à l'excitation acoustique, ainsi que le comportement hyperélastique du caoutchouc, mènent à des déformations non-linéaires. Ce comportement change les propriétés (telles que la rigidité) du joint comprimé lors qu'il est soumis a l'excitation acoustique. De plus, l'interaction du son transmis par les joints avec la cavité du véhicule doit être prise en compte. Néanmoins, la taille réduite et la géométrie complexe du joint appellent à une approche telle que la méthode EF, tandis que la grande taille de la cavité véhicule nécessite d'une approche plus grossière, pour ne pas aboutir sur un modèle trop lourd.

La solution proposée dans ce manuscrit implique la création d'un modèle hybride capable de modéliser le joint et la cavité séparément, avec l'approche la plus adaptée à chaque cas, et de les coupler dans un seul modèle. Les comportements hyperélastique et viscoélastique des joints, avant et durant l'excitation acoustique, sont modélisés à l'aide du code commercial ABAQUS, tandis qu'une méthode énergétique appelée Méthode Énergétique Simplifiée est utilisée pour la propagation du son depuis les joints jusqu'au reste de la cavité. Cette méthode, adapté aux besoins de l'application souhaitée, et couplée aux résultats du modèle EF, permet l'obtention rapide et locale du niveau de pression acoustique en n'importe quel point de la cavité.

Finalement, des campagnes expérimentales sont mises en ouvre pour la validation des modèles. Les mises en place et les résultats sont détaillés dans ce manuscrit.

Mots clés : vibroacoustique, joints, réduction de bruit, Méthode Énergétique Simplifiée, (MES), rayonnement acoustique, industrie automobile, déformation non-linéaire, viscoélasticité, hyperélasticité, comportement matériau du caoutchouc.

Abstract

Car door and window seals have been proven to be of utmost importance to reduce aerodynamic noise, both through direct transmission and through their role as boundary conditions of the other transmitting elements (car doors and windows). As consequence, their design has become of great relevance when it comes to passenger comfort optimization. However, the traditional method for their conception, based on a trial and error approach through wind-tunnel testing, has been found to be insufficient and costly. A different approach is contemplated in this dissertation, through the development of a model capable of predicting sound transmission through seals and into the vehicle cavity, for its subsequent application into an optimization procedure.

Several difficulties arise from the modeling of car door and window seals. Indeed, the door closure imposed on the door seal before any acoustic excitation, as well as the hyperelasticity of the rubber lead to a non-linear deformation behavior. This behavior changes the seal properties (e.g. stiffness) which have to be modeled under acoustic excitation. Additionally, the interaction of the transmitted sound with the vehicle cavity must be taken into account. However, the small, precise geometry of the seal would call for an approach such as FE method, whereas the big dimensions of a vehicle cavity demand a much coarser approach so that the problem doesn't become unmanageable in size.

The solution that is proposed in this dissertation, implies the creation of an hybrid model capable of modeling the seal and the vehicle cavity separately, with the most adequate approach to each case, and coupling them afterward into a single model. As consequence, the hyperelastic and viscoelastic behaviors of the seals, prior to and during the acoustic excitation, are modeled through FE software ABAQUS, whereas an energy method called Méthode Énergétique Simplifiée is used for the propagation of the sound from the seal to the rest of the cavity. This method, improved to better suit the requirements of the discussed application, and coupled to the results of the FE model, allows a fast and local computation of the sound pressure level at any point inside the cavity.

Finally, some experimental tests are put in place for the validation of the models. The different setups and results are detailed in this dissertation.

Keywords: vibroacoustics, seals, sound reduction, Simplified Energy Method (MES), acoustic radiation, automotive industry, non-linear deformation, viscoelas-

ticity, hyperelasticity, rubber material behavior.

Contents

Remerciements **i**

Résumé **iii**

Abstract **iv**

Contents **vi**

List of Figures **x**

List of Tables **xvi**

Introduction **1**
0.1 Bibliography . . . 9

1 Static Model **11**
1.1 Materials . . . 11
1.1.1 Hyperelasticity . . . 12
1.1.2 Neo-Hookean hyperelastic model . . . 15
1.1.3 Choice of a hyperelastic model . . . 18
1.2 Implementation of the Finite Element Static Model . . . 21
1.2.1 Door Seal FE model . . . 24
1.2.2 Window Seal FE model . . . 28
1.3 Experimental Validation . . . 30
1.4 Influence analysis . . . 41
1.5 Conclusions . . . 47
1.6 Expansions . . . 47
1.7 Bibliography . . . 48

2 Dynamic Acoustic Transmission Model **51**
2.1 Acoustic Theory . . . 51
2.1.1 General Equations for acoustic-structural interaction . . . 52
2.1.2 Acoustic Transmission and Radiation . . . 55
2.1.3 Sommerfeld condition with infinite elements . . . 59
2.1.4 The diffuse field . . . 61
2.2 Materials . . . 62
2.2.1 Viscoelasticity . . . 63

2.2.2 Coupling of viscoelasticity with hyperelasticity 63
2.2.3 Models of linear viscoelasticity 64
2.2.4 Experimental determination of viscoelastic coefficients 70
2.3 Implementation of the Finite Element acoustic model 75
2.3.1 Simplified Transmission Model 76
2.3.2 Door Seal Transmission Model 79
2.3.3 Window Seal transmission model 81
2.3.4 Window Transmission Model 85
2.4 Experimental Validation 88
2.4.1 The test bench 88
2.4.2 Experimental results 94
2.4.3 Numerical Transmission Model for experimental validation . . 96
2.4.4 Comparison of the experimental and numerical transmission loss curves 97
2.5 Conclusions 100
2.6 Expansions 101
2.7 Bibliography 101

3 Acoustic Propagation Model 103
3.1 Simplified Energy Method (MES) 104
3.1.1 Theory and assumptions 104
3.1.2 Directivity 109
3.1.3 Visibility 110
3.2 Implementation of the improved MES and coupling with the Transmission Model 111
3.2.1 Directivity improvement: equivalent source 112
3.2.2 Visibility solution 115
3.2.3 Equivalent FE model 115
3.3 Validation of the improved MES and comparison to an equivalent FE model 116
3.4 MES application to the studied elements and excitation influence . . . 119
3.4.1 Door seal MES 120
3.4.2 Window seal MES 120
3.4.3 Window MES 121
3.5 Conclusions 126
3.6 Expansions 126
3.7 Bibliography 127

General Conclusions and Expansions 131

A Dynamic material data 135

B Calibration of the viscoelastic material characterization setup 137

C Experimental prototype for door seal transmission loss **139**

D Visibility solution **145**

List of Figures

0.1 V-cycle schematics 2
0.2 Different kinds of car seals 4
0.3 Perpendicular Section of the upper frame of the chosen vehicle 5
0.4 Door Seal material distribution 5
0.5 Insertion and compression phases of door seals 6
0.6 Door Seal material distribution 8

1.1 Uniaxial compression curves for some hyperelastic material models . . 19
1.2 Uniaxial compression curves for stable hyperelastic models 20
1.3 Volumetric compression curves for stable hyperelastic models 21
1.4 Reaction force on door throughout seal compression for several material models 22
1.5 Elements needed for only the static step and additional acoustic elements for a static+acoustic model 24
1.6 Schematics of the Transmission Model 25
1.7 Door seal mesh 26
1.8 a) Staggered contact between the lips and the frame. b) The upper and lower frames accompany the deformation of the lips which leads to easier convergence. 27
1.9 Different states of vertical compression 28
1.10 Numerical results of the door seal after each phase 29
1.11 Numerical results of the door seal for each level of compression 29
1.12 Resulting window seal mesh 30
1.13 Window insertion 30
1.14 Resulting window seal stress 31
1.15 First experimental setup for the validation of the Static Model 32
1.16 Modified numerical model for experimental validation 33
1.17 Chosen representative points for deformation validation 33
1.18 Numerical and physical seals with their equivalent geometric elements 34
1.19 a) Non-coincident seal geometries. b) Non-coincident equivalent vertices 35
1.20 a) Displacement of control points throughout compression. b) Displacement of control points throughout compression with shifted initial coordinates 36
1.21 Experimental setup for stress validation 37
1.22 Seal profile and seal section definitions 38
1.23 Results of experimental tests for stress validation. Different profiles and sections 38

1.24 Repeatability tests on P2S2 . . . 39
1.25 Experimental reaction force vs numerical reaction force . . . 39
1.26 Original (left) and modified (right) geometries of the door seal . . . 40
1.27 Comparison of experimental results for different seal sections with and without the use of lubricant . . . 42
1.28 Results for reaction force when the door incident angle is tilted using the new seal geometry . . . 42
1.29 Comparison of experimental and numerical reaction force with a friction coefficient of 0.4 when the door incident angle is tilted . . . 43
1.30 Comparison of numerical reaction force for different friction coefficients 44
1.31 Geometry modifications tested for their influence on the final seal reaction force . . . 45
1.32 Reaction force for each modified seal . . . 45
1.33 Comparison of reaction force between initial and final modified geometry 46
1.34 Numerical results of the door seal with modified geometry for each level of compression . . . 46

2.1 Acosutic-excited plate vibrating between 2 media . . . 56
2.2 Coincidence phenomenon between two media . . . 57
2.3 Typical TL curve for a finite plate . . . 60
2.4 Implementation of IE in truncated infinite domain . . . 61
2.5 Infinite element mapping . . . 61
2.6 Waves impinging from different directions create a diffuse field . . . 62
2.7 Maxwell model . . . 66
2.8 Standard Linear Solid model . . . 66
2.9 Generalized Maxwell model . . . 67
2.10 Influence of g_1^p and τ on G^* . . . 69
2.11 Detail of the influence on the magnitude of G^* . . . 69
2.12 Cut and tested section of the seal . . . 70
2.13 Rubber and aluminum sandwich-like structure for the experimental determination of the viscoelastic parameters . . . 71
2.14 Experimental setup for the calibration of the Prony Series coefficients 72
2.15 A small piece is simulated over the sandwich-like element to account for additional mass and rigidity of the experimental sensors . . . 72
2.16 Final numerical model for the determination of the viscoelastic parameters . . . 72
2.17 Magnitude of the moduli for $g_1^p/k_1^p = 0.8$ and$\tau_1 = 0.0025$. The value is considered constant for frequencies higher than $f_0 = 400Hz$, since from this value onwards the magnitude only varies from 0.79 to 0.8 . . . 73
2.18 Final values of the dynamic complex modulus E^* of the EPDM on the door seal . . . 75
2.19 Benchmark case used for comparison . . . 76
2.20 Simplified model of a plate vibrating between 2 media . . . 77
2.21 Transmission Loss for a single wave excitation incident at 45° . . . 78

2.22 Transmission Loss for a diffuse field excitation 79
2.23 Door seal Transmission Loss model 80
2.24 Boundary conditions on the door seal transmission model 81
2.25 Door seal TL for 20-wave diffuse field 82
2.26 Window Seal Transmission Loss model 83
2.27 Boundary conditions on the Window Seal Transmission Model 83
2.28 TL for the window seal 84
2.29 The seal's effect can be characterized by an equivalent dynamic stiffness 86
2.30 Values of $1/K_{dyn}$ for the equivalent seal 86
2.31 Values of TF for the window seal 87
2.32 Values of TF for the window seal model and equivalent model 87
2.33 Window Transmission Loss model 88
2.34 Boundary conditions on the window Transmission Model 89
2.35 TL for the window, with replaced boundaries. 89
2.36 Acoustic cabin 90
2.37 Receiving microphone placement. View from the top of Figure 2.36 . 91
2.38 Experimental assembly for acoustic tests 92
2.39 a) Several elements are added in order avoid unwanted radiation b)Nitto and mastic are used to prevent leakage 93
2.40 Example of the results in the outputted excel file for J3S1 H3 94
2.41 Experimental TL curves for H1 compression for each seal section . . . 95
2.42 Experimental TL mean curves of all seal sections for each compression level 96
2.43 Numerical model for comparison with experimental results. Each red point corresponds to a microphone 97
2.44 Experimental TL curve for J2S2H1 vs. numerical curves for the 4 "microphones" and its mean value 99
2.45 Experimental TL curve vs. numerical microphones mean TL, per octave band 99

3.1 Energy balance in an elementary volume 105
3.2 The total intensity and power in one point are the sums of their direct and reverberant field components 109
3.3 The reverberant field is assimilated to the direct field of secondary sources 109
3.4 Diffuse reflection (Lambert's emission law) 110
3.5 Self-obstruction 110
3.6 Obstruction to another element 110
3.7 Pressure distribution caused by the excited seal at 7144Hz 111
3.8 Pressure P(φ) is measured for all points in a half-circle of the Transmission Model boundary 112
3.9 The seal is replaced by a single equivalent element with a point source with a specified directivity 113

3.10 The window is replaced by a single equivalent element with a point source with a specified directivity 114
3.11 Schematics of the equivalent source method 115
3.12 Whole cavity equivalent FE model. Infinite elements in orange 116
3.13 Directivity values for frequency band between 3564 and 4490Hz. a)Directivity comparison for different values of R_{arc}. b)Directivity for $R_{arc} = 40$ for $\varphi = [0, \pi]$ 118
3.14 Comparison of MES with converged $R_{arc} = 1200mm$ against FE equivalent model for frequency band 3564-4490Hz. Values are in dB of W . 118
3.15 Comparison of MES with small $R_{arc} = 40mm$ against FE equivalent model for frequency band 3564-4490Hz. Values are in dB of W 119
3.16 Comparison of MES with small $R_{arc} = 40mm$ and lambertian directivity against FE equivalent model for frequency band 3564-4490Hz. Values are in dB of W 120
3.17 L_p for a point 20 cm away from the door seal, obtained through the improved MES 121
3.18 Whole cavity L_p distribution for door seal radiation, plotted using improved MES. Values are in dB of W 122
3.19 L_p for a point 20 cm away from the window seal, obtained through the improved MES 123
3.20 Whole cavity L_p distribution for window seal radiation, plotted using improved MES. Values are in dB of W 123
3.21 L_p for a point 20 cm away from the window, obtained through the improved MES 124
3.22 Whole cavity L_p distribution for window radiation, plotted using improved MES. Values are in dB of W 124
3.23 L_p curves for a single wave, with different equivalent stiffness parameters for the window model 125
3.24 L_p curves for a single wave, with different equivalent damping parameters for the window model 125

A.1 Dynamic material data for incompressible EPDM 136

C.1 Sketch of the plate-like part for the acoustic experiments with main dimensions 140
C.2 Sketch of the part simulating the door for the acoustic experiments with main dimensions 141
C.3 Sketch of the part simulating the frame for the acoustic experiments with main dimensions 142
C.4 Sketch of the door part guides for the acoustic experiments with main dimensions 143

D.1 First condition examples. Case where element E obstructs the energy flow between P and M (left) and case where it does not (right) 146

D.2 First condition examples. Case where element E obstructs the energy flow between P and M (left) and case where it does not (right) 147

List of Tables

0.1 Available material data before study 9

1.1 Hyperelastic material models 15
1.2 Time cost of seal compression simulation for each material model . . . 21
1.3 Material information for static analysis 22

2.1 Experimental(black) and Numerical(blue) modes correlation for different beam lengths and Prony series parameters $\mu_1 = 0.75, \lambda_1 = 0.9, \tau = 1.85$ 74
2.2 Material information for dynamic analysis 74

3.1 Time comparison for both approaches. All calculations have been achieved through a system of 32 CPU and 264Go of RAM 118

B.1 Experimental modes for the excitation of a single beam 137
B.2 Experimental(black) and Numerical(blue) modes correlation for 200mm beam test 138

Introduction

In the last decade, noise reduction has become an important criterion for vehicle design. Car manufacturers put an important effort to reduce sources of noise, and their transmission to the interior of the vehicle. These sources can be of various natures. At elevated speeds ($80km/h$) aerodynamic noise overtakes the other kinds of noise. A turbulent flow develops on the exterior of the vehicle, creating a fluctuating pressure field that impacts the walls and other elements of the car, which transmit the noise into the vehicle interior.

PSA Group internal studies show that an important amount of this aerodynamic noise is transmitted through windows and car door and window seals, especially for high frequencies. Additionally, seals have a double role in noise transmission:

- From a **structural** point of view, they define the boundary conditions of the elements they are supporting, doors and windows. Given that the latter are known to be important transmission paths, optimizing the mechanical properties of window seals is relevant for sound reduction.
- From an **acoustic transmission** point of view, the seals themselves are excited by the aerodynamic and aeroacoustic fields, and constitute another transmission path for noise.

The optimization of these kinds of elements is nowadays often achieved through trial and error, from wind tunnel testing experiments. These tests, as well as the several necessary prototypes to carry them out, have an important cost. Additionally, they can only take place in the last phase of conception, not satisfying the V-cycle procedure, and consequently not being able to deliver optimal solutions.

The V-cycle is a methodology used in product conception, which describes the different phases that should be taken into account when creating a product (see Figure 0.1). One of these phases, called "functional requirements", implies the determination of the optimal value for the desired functionality of the product (such as the sound transmission loss factor). The next phase in the cycle, "element specification", uses these optimal values as criteria for the optimization of the element parameters that play a role in these functionalities (such as the compression of the seal or its materials). This allows the optimization to take into account all the parameters as a whole achieving an optimal combination.

For these reasons, manufacturers have started investing in the development of numerical models allowing seal optimization, both in acoustic performance and cost,

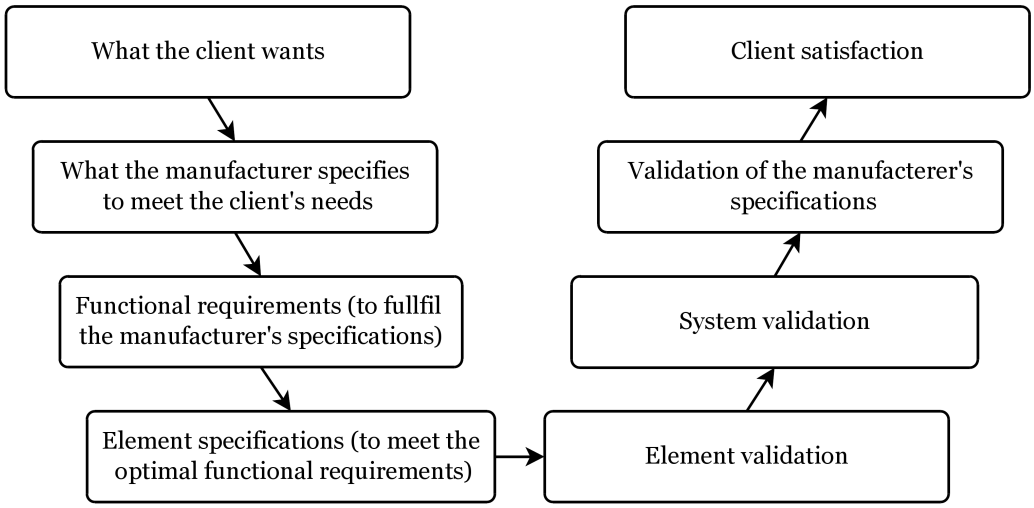

Figure 0.1: V-cycle schematics

earlier in the conception cycle. However, these numerical models are often complex, due to the non-linear behavior of the seals. This complexity goes from hyperelastic materials to frequency or amplitude-dependent dynamic properties.

The first difficulty is to take into account static the pre-compression of door seals when the car door closes. This causes a pre-deformed and pre-stressed state, which modify the dynamic properties of the seal, such as stiffness. This will have an influence over their dynamic response when an acoustic perturbation is applied later on, hence on its sound-reducing properties. In consequence, a static modeling of this pre-compression is necessary before being able to simulate the seal's response to any acoustical excitation ([ACDM08] [SMD04]).

Since these kinds of seals are usually made of rubber, they often enter the large-deformation zone when compressed, especially car door seals. Thus, a non-linear model, which takes into account this hyperelasticity, must be considered and used to determine the seal properties when the door is closed.

The second difficulty is the introduction of damping in the model. When submitted to dynamic excitations, rubber presents a supplementary viscous behavior, which can be dependent on the frequency as well as on the amplitude of the excitation (Payne effect) ([SMSD06] [SMSD08]). In consequence a choice of a viscoelastic model, capable of representing these non-linearities, should be made.

However, even if the material model choices are done right, the acoustical information that we can obtain from a model of the seal is limited. If the goal is passenger comfort, we should be able to predict noise perceived by someone sitting inside the

vehicle cavity, whereas the model of the seal alone only gives information of noise levels 2 or 3 centimeters away from the seal walls, and only its free-field component, without taking into account the surrounding elements. Therefore the model should include the whole vehicle cavity, or at least a big enough part of it. From a computational point of view this presents yet another issue: given the range of frequencies participating in an aeroacoustic excitation (400-1000Hz), the problem including both seal and vehicle cavity would ask for a statistical approach, such as an energy method. A BEM approach could also be considered. However, due to this method's difficulties in taking into account complex geometries and the appearance of spurious modes, it is mainly only used in free-field acoustics. This, together with the fact that at such high frequencies the phase is irrelevant, makes the statistical energy method a more suitable choice. However, the complex geometry of this kind of seal and its material non-linearities require that it be modeled using a fine mesh, as in the finite element method. Nonetheless, a fine mesh applied to the entire vehicle cavity for the desired range of frequencies, would imply hundreds of thousands of degrees of freedom, which would lead to heavy simulations. Hence, the problem requires the first kind of model (statistical) for the vehicle cavity, whereas the second kind (FE) would be more suited for the modeling of the seal.

In consequence, this problem calls for the combination of a FE model of the seal (hereafter called the "Transmission Model") with an energy model of the cavity (from here on the "Propagation Model") into one single model (the "Total Model").

Finally, the resulting Total Model should be as light as possible, so that it can be included in the desired optimization procedure.

Seal choice

As stated earlier, previous studies have shown a strong influence of window panes and seals, as well as door seals, in the transmission of aerodynamic noise into the interior of the vehicle cavity. A lot of work has already been done in the modeling of plate-like elements such as window panes. In consequence, although these elements will also be taken into account, our main interest will be the modeling of the seals. These come in several geometries and materials, depending on the type of vehicle they are integrated in, their desired performance, etc. Hence, a choice for each type of seal has to be made that can represent the whole of window and door seals, of enough complexity that its modeling can be adapted to the majority of the other seals, but easy enough that it doesn't become an unmanageable problem.

Car seals have 4 main goals: impermeability, window/door closing, aerodynamics, and noise reduction. This leads to a very wide range of different seals, with very disparate geometry, materials, and size, according to their function and the needs of the future user. The general geometries are represented in Figure 0.2. The simpler

door seals (simple tube) are designed for less strict applications such as in the case of trucks, where aerodynamic sources are a minor issue compared to other noise sources, or to be combined with more complex seals in order to improve the overall sound or water isolation.

Car seals are usually made from a combination of several materials; however, excluding metal reinforcement, these often come from the same 2 material families:

- Ethylene Propylene Diene Monomer (EPDM), usually used for car door seals where some compression is expected.
- Thermoplastic Elastomers (TPE) often used for window seals.

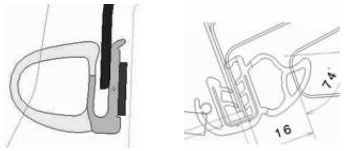

Simple tube Double tube

Door Seals



Simple lip Double lip Triple lip

Window Seals

Figure 0.2: Different kinds of car seals

According to the needs of PSA Group, the seals used in the new Peugeot 208 have been chosen for this study. All four doors and all four windows have the same seal geometry. Figure 0.3 shows the perpendicular section of the upper frame, where we can see both seals and their position regarding the surrounding elements. These geometries are extruded into long tube-like elements, and in the case of door seals the extremes are joined into a loop of constant section. This tubular geometry allows the consideration of using 2D modeling for simplification, instead of the entire 3D structure.

Door Seal

The modeling of door seals is usually more complex than that of window seals. The fact that the former have rubbers with different compressibility, and that the pre-

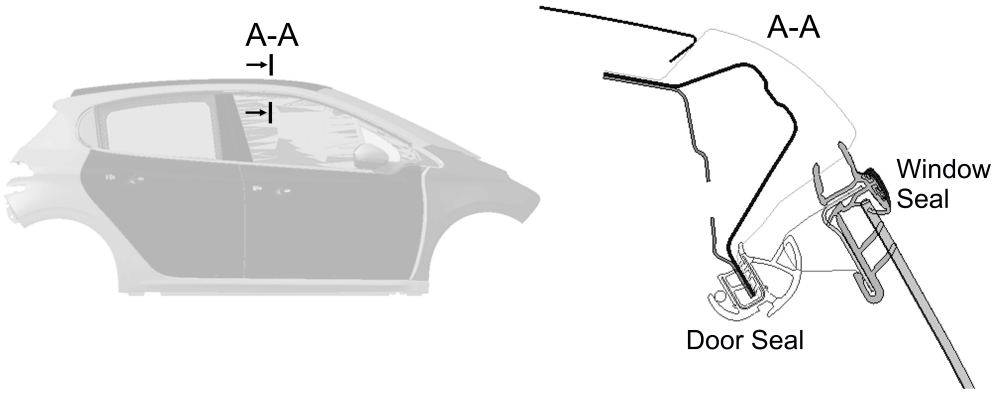

Figure 0.3: Perpendicular Section of the upper frame of the chosen vehicle

stressed state has to be modeled through a large deformation door-closure step, yield them more interesting than the latter. In Figure 0.4 we can see the geometry of this seal as well as the distribution of its materials.

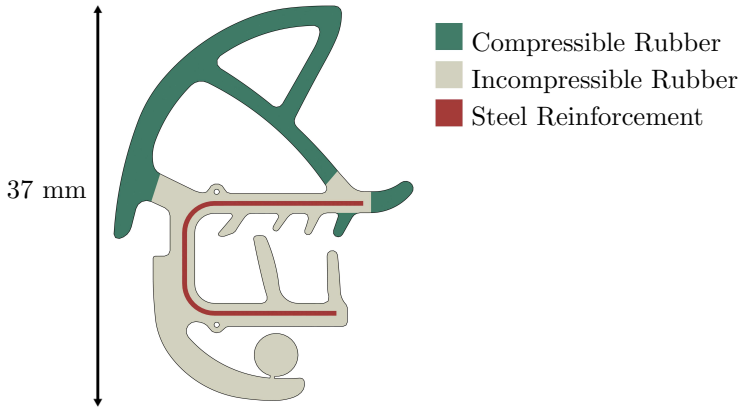

Figure 0.4: Door Seal material distribution

The lower part is made from a simple EPDM incompressible rubber. It contains the lips with which the seal clamps onto the edge of the frame and is kept in place. The upper part is made of EPDM foam rubber; hence, its compressible nature has to be taken into account. When the door pictured in Figure 0.5.b is closed, it compresses this part of the seal. This zone has some perforations every few centimeters along its extruded profile, in order to ensure that there is no increase of the pressure level inside the interior cavities, so that the door can be well closed easily, avoiding leakage. It is also this zone that is exposed to the sound waves from the exterior, through the small cavity left between the frame of the car and the door, when the latter is closed. Consequently, a correct modeling of this part of the seal is of high

importance. Finally, a steel spine is embedded into the incompressible EPDM to provide a stiffer grip of the lips into the edge. Contrary to the other two materials, this one is not continuous along the entire length of the extruded seal. This confers the seal the ability to be bent into the necessary shape along its extruded axes so that it can be built into the contour of front or rear door frames. However, this discontinuity also adds a certain amount of incertitude to its modeling.

To determine the real stress distribution inside the seal, all the phases it goes through have to be taken into account.

- **Insertion**: In the first place, the seal, in a relaxed state (zero internal stress), is fixed onto the frame. This is achieved by pushing the seal so that the lips are clamped around the edge of the frame. This is equivalent to saying a force is applied onto the seal until it's well attached. The resulting state can be seen in Figure 0.5.a.
- **Relaxation**: After insertion, the force that was being applied is released, and so the efforts balance themselves into an equilibrium position, where internal stress is no longer equal to zero.
- **Compression**: Next, the door is closed. This compresses the EPDM foam mentioned earlier and generates a new state of internal stress.
- **Acoustic excitation**: Finally, the car is started and running, and the aerodynamic sources resulting from the speed excite the compressed foam.

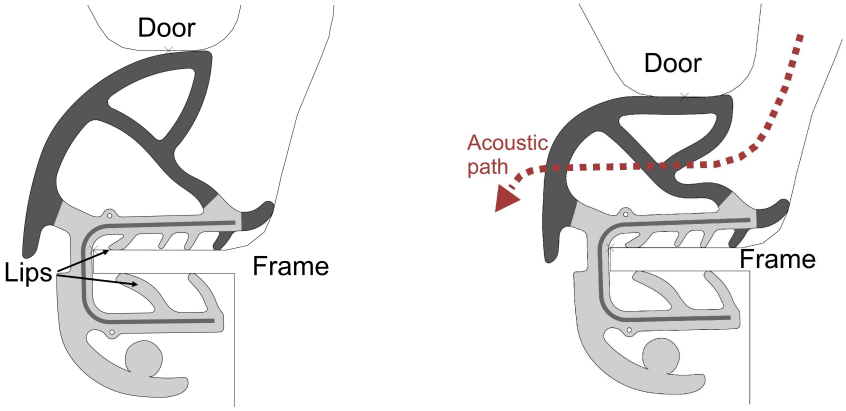

a) Door seal after its insertion into the frame

b) Door seal after compression

Figure 0.5: Insertion and compression phases of door seals

Since the door folds and unfolds around its hinge in the part of the door frame closest to the front of the car, the direction of the compression of the seal is uneven

throughout its length. Closest to the hinge, the seal will be compressed in a diagonal direction with respect to the frame, whereas in the frame zone farthest from the hinge it will be compressed in an almost vertical direction, as in Figure 0.5.b. For simplicity, we have chosen the last case for our reference seal door model.

Finally, door seals have a double function. They are a path for acoustic transmission but they also act as a boundary condition to doors. However, because doors are not as important for sound reduction as windows, they are not part of this study, and the door seals' role on their sound transmission is not considered.

Because of its geometrical and material complexities, as well as the fact that there are more phases to be taken into account, the door seal has been chosen as the reference case for modeling. The same techniques leading to the desired functioning model that will be used for door seals will be applied later on to window seals, with some additions to include the latter's singularities.

Window Seal

The chosen window seal is a complex combination of several materials, mainly TPE's. However, we do not have access to the precise properties of these materials. Nevertheless, an internal PSA Group study determines the average homogenized behavior of a window seal similar to the one used for this study, using a linear Hooke's law, damped model. Because window seals don't go through deformations as large as those found in a door seal after compression, we assume using a linear model is legitimate for these seals and we will use these values for our modeling. However, the same internal study shows that the Young's modulus and damping of the material have been proven to have a slight influence over the dynamic response at mid to high frequencies, hence, a more detailed material configuration should be taken into account for more precise results.

Unlike door seals, window seals don't have a metallic reinforcement, but they have 2 sets of lips (see Figure 0.6). The first set is designed to be adapted to the shape of the window when it's closed, so as to ensure sealing between the pane and the door. The second one acts as a second obstacle for sound in the door-frame cavity. However, for simplicity, we have only taken the first set into account, since sound coming through the door-frame gap is mainly damped by the door seal. The window seal is clamped to the door edge through a simple clamp.

In the same way as for the door seal, all the phases have to be taken into account in order to obtain good results.

- **Seal Insertion**: As for the door seal, the first step for window seals is their insertion into the door frame.
- **Seal Relaxation**: The force applied for the insertion of the seal is released.

- **Window Insertion**: In the same way as for seal insertion, the window is pushed into the lips of the seal when closed. However, unlike for door seal insertion, the movement of the window is imposed and maintained, so there is no release of the force and posterior relaxation of the seal. After this step the internal stresses are different than 0.
- **Acoustic excitation**: Finally, the car is started and running and the aerodynamic sources resulting from the speed excite the seal and the window.

Additionally to their role in sound transmission, window seals play a relevant role as boundary conditions in window panes, as door seals do for doors. However, unlike the latter, window panes are fairly relevant in sound reduction strategies. Consequently the impact of the boundary conditions imposed on them by window seals, when submitted to structural vibrations of different frequencies, has to be characterized.

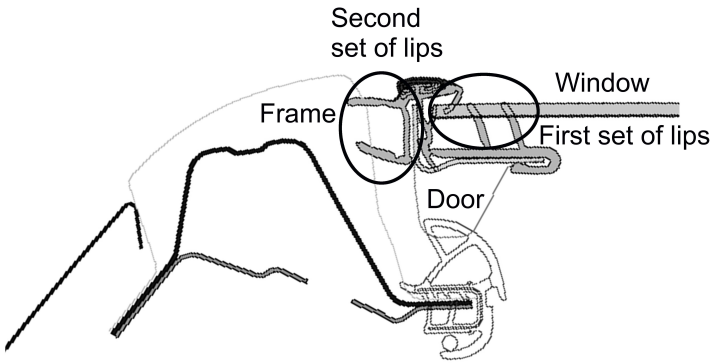

Figure 0.6: Door Seal material distribution

Materials

The different materials used in the seals have been named above. As explained, in the case of the window seal, the averaged material behaviors of several similar seals, obtained from an internal PSA Group study, has been used. This will be represented by Hooke's law model, under the assumption that the deformation in this type of seal is small enough for the material to be considered linear. In the case of the door seal, there are only 3 materials, one of which is steel, the parameters of which are easily extracted from the bibliography. For the two types of rubber, however, the data we have is incomplete. Table 0.1 summarizes the information that we have on every seal and every material for static and frequency dependent modeling.

Door Seal			Window Seal
Compressible EPDM	Incompressible EPDM	Steel	Homogenized TPE
Static: Uniaxial and Volumetric data	**Static**: Neo-Hookean coefficients	**Static**: Hooke's Law values E, υ	**Static**: Hooke's law values E, υ
Dynamic: No data	**Dynamic**: Experimental data	**Dynamic**: Structural damping η	**Dynamic**: Structural damping η

Table 0.1: Available material data before study

Model Structure

For the reasons mentioned above and explained in detail throughout this dissertation the problem is separated into 2 models:

- The Transmission Model: This model attempts to represent the capacity of the seal to transmit or block sound incoming from one side, to the other, regardless of the shape and properties of the receiving side. This modeling will only take into account the seals or windows and its immediate surroundings, and will be simulated as an exterior problem propagating into an infinite space. For reasons that will be explained in Chapter 1, this model has to be divided into 2 sub-models:
  - The Static Model that models only the static steps of the seals, previous to the acoustic excitation and outputs the stress and deformation of the seals.
  - The Acoustic Transmission Model that inputs the state of deformation and stress resulting from the previous static model (if any) and applies a static excitation to determine the blocking capacity of the elements.
- The Propagation Model: This model takes the energy output from the previous transmission model and determines how it is going to propagate into the receiving end, that is, the vehicle cavity. This modeling takes into account the geometry of the receiving cavity, the absorption of the walls, and the position of the calculated point in relation to the source. A simplified energy model will be used and ameliorated for this matter.

0.1 Bibliography

[ACDM08] B. Andro, S. Chaigne, A. Diallo, and M. Mermet. Prediction of sound transmission through automotive door seal systems. In *Proceedings - European Conference on Noise Control*, pages 3819–3824, 2008.

[SMD04] A. Stenti, D. Moens, and W. Desmet. Dynamic modeling of car door weather seals: A first outline. In *Proceedings of the 2004 International Conference on Noise and Vibration Engineering, ISMA*, pages 1249–1261, 2004.

[SMSD06] A. Stenti, D. Moens, P. Sas, and Wim Desmet. Development of a numerical modelling methodology for the NVH behaviour of elastomeric line connections. In *International Conference on Noise and Vibration Engineering*, 2006.

[SMSD08] A. Stenti, D. Moens, P. Sas, and W. Desmet. Low-frequency dynamic analysis of automotive door weather-strip seals. *Mechanical Systems and Signal Processing*, 22(5):1248–1260, 2008.

Chapter 1

Static Model

This chapter describes in detail the techniques used in the intention of the Static FE Model for window and door seals.

As stated in the Introduction, both studied seals have a static step that needs to be taken into account before the introduction of the acoustic excitation ([ACDM08], [DB06], [SMSD06], [SMD04], [SMSD08] and [WMGK97]). This chapter explains the need to separate this static step from the acoustic excitation into two separate models.

For modeling the static part, a numerical material model has to be chosen for each material case, depending on the data at hand and on the complexity of the said material. In the case of compressible rubber, and due to the sort of information available, the procedure to the obtainment of the correct material model is explained, and the choice is justified and compared to other model choices.

We describe in detail how modeling of this static step is achieved using commercial software ABAQUS, which requires bypassing the restrictions implied in using a finite element software for this kind of problem. Later on, the experimental method used for the validation of the entire FE model is explained and the results compared to those of the numerical model.

1.1 Materials

It has been previously mentioned that both seals are made of several types of rubber that, although distinct, share a common elastic behavior. Both are subject to large deformations in their static phases and in consequence, their stress-strain relationship might no longer be linear but already in its hyperelastic regime. In consequence, a method being able to describe non-linear hyperelastic material deformation must be implemented in the models. In this analysis we will not consider the Mullins effect, which accounts for a significant reduction of stress for a given applied strain after successive loading and unloading conditions ([DB06]).

1.1.1 Hyperelasticity

For some materials, linear elastic models cannot accurately represent the material's behavior. The stress-strain relationship can be non-linearly elastic and thus a model different than Hooke's model is required. A hyperelastic material is a type of elastic material for which the stress-strain relationship derives from the strain energy density function. This is the case for the rubber used in the fabrication of some seals, such as the ones studied throughout this dissertation.

General equations in terms of the invariants

The general equations for an hyperelastic material start with the definition of the second Piola-Kirchoff stress tensor $\mathbf{S}$ obtained from the derivation of the strain energy density function W ([Bow09],[WMGK97]):

$$\mathbf{S} = 2\frac{\partial W}{\partial \mathbf{C}} \tag{1.1}$$

with $\mathbf{C} = \mathbf{F^T F}$ the right Cauchy-Green deformation tensor and $\mathbf{F}$ the deformation gradient. The Cauchy stress is given by

$$\boldsymbol{\sigma} = \frac{1}{J}\mathbf{F S F^T} = \frac{2}{J}\mathbf{F}\frac{\partial W}{\partial \mathbf{C}}\mathbf{F^T} \tag{1.2}$$

$$J = det(\mathbf{F}) \tag{1.3}$$

If we introduce the three first invariants of $\mathbf{C}$, I_1,I_2 and I_3 :

$$\frac{\partial W}{\partial \mathbf{C}} = \frac{\partial W}{\partial I_1}\frac{\partial I_1}{\partial \mathbf{C}} + \frac{\partial W}{\partial I_2}\frac{\partial I_2}{\partial \mathbf{C}} + \frac{\partial W}{\partial I_3}\frac{\partial I_3}{\partial \mathbf{C}} \tag{1.4}$$

Since $\mathbf{C}$ is symmetric, the derivatives of its invariants are:

$$\begin{aligned} \frac{\partial I_1}{\partial \mathbf{C}} &= \mathbf{I} \\ \frac{\partial I_2}{\partial \mathbf{C}} &= I_1\mathbf{I} - \mathbf{C} \\ \frac{\partial I_3}{\partial \mathbf{C}} &= \frac{det\mathbf{C}}{\mathbf{C}} = \frac{I_3}{\mathbf{C}} = I_3\mathbf{F^{-1}}(\mathbf{F^T})^{-\mathbf{1}} \end{aligned} \tag{1.5}$$

And hence from equations 1.2 and 1.5:

$$\begin{aligned} \boldsymbol{\sigma} &= \frac{2}{J}\mathbf{F}\left[\frac{\partial W}{\partial I_1}\mathbf{I} + \frac{\partial W}{\partial I_2}I_1\mathbf{I} - \frac{\partial W}{\partial I_2}\mathbf{F^T F} + \frac{\partial W}{\partial I_3}I_3\mathbf{F^{-1}}(\mathbf{F^T})^{-\mathbf{1}}\right]\mathbf{F^T} \\ &= \frac{2}{J}\left[(\frac{\partial W}{\partial I_1} + \frac{\partial W}{\partial I_2})\mathbf{B} - \frac{\partial W}{\partial I_2}\mathbf{BB} + \frac{\partial W}{\partial I_3}I_3\mathbf{I}\right] \end{aligned} \tag{1.6}$$

Where $\mathbf{B} = \mathbf{F F^T}$ is the left Cauchy-Green deformation tensor.

Given that $I_3 = J^2$ the previous equation becomes:

$$\boldsymbol{\sigma} = \frac{2}{\sqrt{I_3}}\left[(\frac{\partial W}{\partial I_1} + \frac{\partial W}{\partial I_2})\mathbf{B} - \frac{\partial W}{\partial I_2}\mathbf{B}\mathbf{B}\right] + 2\sqrt{3}\frac{\partial W}{\partial I_3}\mathbf{I} \tag{1.7}$$

Equation 1.7 is the general form of the Cauchy stress for hyperelasticity. If the material is incompressible $I_3 = 1$ and so $W = W(I_1, I_2)$. Then

$$\frac{\partial W}{\partial \mathbf{C}} = \frac{\partial W}{\partial I_1}\frac{\partial I_1}{\partial \mathbf{C}} + \frac{\partial W}{\partial I_2}\frac{\partial I_2}{\partial \mathbf{C}} \tag{1.8}$$

and equation 1.7 becomes:

$$\boldsymbol{\sigma} = \frac{2}{\sqrt{I_3}}\left[(\frac{\partial W}{\partial I_1} + \frac{\partial W}{\partial I_2})\mathbf{B} - \frac{\partial W}{\partial I_2}\mathbf{B}\mathbf{B}\right] + p^*\mathbf{I} \tag{1.9}$$

Here p^* is an undetermined pressure working as a Lagrange multiplier to enforce in-compressibility.

Equations in terms of the isochoric deformation gradient

Another way to develop these equations is using the isochoric deformation gradient defined as $\overline{\mathbf{F}} = J^{-1/3}\mathbf{F}$. This leads to $\overline{\mathbf{F}}$ having a determinant of 1. Using this, one can represent the strain energy density function as $W = (\overline{I}_1, \overline{I}_2, J)$

$$\begin{aligned}
\overline{\mathbf{B}} &= J^{-2/3}\mathbf{B} \\
\overline{I}_1 &= J^{-2/3}I_1 \\
\overline{I}_2 &= J^{-4/3}I_2 \\
\overline{I}_3 &= 1
\end{aligned} \tag{1.10}$$

The derivatives of these new parameters are:

$$\begin{aligned}
\frac{\partial W}{\partial I_1} &= J^{2/3}\frac{\partial W}{\partial \overline{I}_1} \\
\frac{\partial W}{\partial I_2} &= J^{-4/3}\frac{\partial W}{\partial \overline{I}_2} \\
\frac{\partial W}{\partial I_3} &= \frac{\partial W}{\partial \overline{I}_1}\frac{\partial \overline{I}_1}{\partial I_3} + \frac{\partial W}{\partial \overline{I}_2}\frac{\partial \overline{I}_2}{\partial I_3} + \frac{\partial W}{\partial J}\frac{\partial J}{\partial I_3} \\
&= -\frac{1}{3}J^{-2}\left(\overline{I}_1\frac{\partial W}{\partial \overline{I}_1} + 2\overline{I}_2\frac{\partial W}{\partial \overline{I}_2}\right) + \frac{1}{2}J^{-1}\frac{W}{J}
\end{aligned} \tag{1.11}$$

Substituting this in equation 1.6, we obtain

$$\boldsymbol{\sigma} = \frac{2}{J}\left[\frac{1}{J^{2/3}}(\frac{\partial W}{\partial \overline{I}_1} + \frac{\partial W}{\partial \overline{I}_2})\mathbf{B} - \frac{1}{J^{4/3}}\frac{\partial W}{\partial \overline{I}_2}\mathbf{B}\mathbf{B}\right] + \left[\frac{\partial W}{\partial J} - \frac{2}{3J}\left(\overline{I}_1\frac{\partial W}{\partial \overline{I}_1} + 2\overline{I}_2\frac{\partial W}{\partial \overline{I}_2}\right)\right]\mathbf{I} \tag{1.12}$$

And for incompressible materials

$$\boldsymbol{\sigma} = 2\left[(\frac{\partial W}{\partial \bar{I}_1} + \frac{\partial W}{\partial \bar{I}_2})\mathbf{B} - \frac{\partial W}{\partial \bar{I}_2}\mathbf{B}\mathbf{B}\right] - p^*\mathbf{I} \tag{1.13}$$

All hyperelastic models need to be consistent with the linear elasticity theory for infinitesimal strains. Hence, the parameters of an equivalent Hooke's Law can be found for $\varepsilon \ll 1$. For this, the previous equations need to be expressed in terms of the principal stretches of $\mathbf{C}$, thus the strain energy density function becomes $W(\lambda_1, \lambda_2, \lambda_3)$.

Equations in terms of the principal stretches

Recalling the derivatives of the stretches

$$\frac{\partial \lambda_i}{\partial \mathbf{C}} = \frac{1}{2\lambda_i}\mathbf{N_i} \otimes \mathbf{N_i} = \frac{1}{2\lambda_i}\mathbf{R^T}\mathbf{n_i} \otimes \mathbf{n_i}\mathbf{R} \tag{1.14}$$

Where $\mathbf{N_i}$ is the eigenvector related to eigenvalue λ_i^2 of $\mathbf{C}$ and $\mathbf{n_i}$ is the eigenvector related to eigenvalue λ_i^2 of $\mathbf{B}$. $\mathbf{R}$ is the rotation tensor result of the polar decomposition of $\mathbf{F}$. Let us remind that the outer product of two vectors is expressed as

$$u \otimes v = uv^T = \begin{pmatrix} u_1 \\ u_2 \\ u_3 \\ u_4 \end{pmatrix} \begin{pmatrix} v_1 & v_2 & v_3 \end{pmatrix} = \begin{pmatrix} u_1v_1 & u_1v_2 & u_1v_3 \\ u_2v_1 & u_2v_2 & u_2v_3 \\ u_3v1 & u_3v2 & u_3v_3 \\ u_4v_1 & u_4v_2 & u_4v_3 \end{pmatrix} \tag{1.15}$$

Applying the chain rule we obtain

$$\begin{aligned} \frac{\partial W}{\partial \mathbf{C}} &= \frac{\partial W}{\partial \lambda_1}\frac{\partial \lambda_1}{\partial \mathbf{C}} + \frac{\partial W}{\partial \lambda_2}\frac{\partial \lambda_2}{\partial \mathbf{C}} + \frac{\partial W}{\partial \lambda_3}\frac{\partial \lambda_3}{\partial \mathbf{C}} \\ &= \mathbf{R^T}\left[\frac{1}{2\lambda_1}\frac{\partial W}{\partial \lambda_1}\mathbf{n_1} \otimes \mathbf{n_1} + \frac{1}{2\lambda_2}\frac{\partial W}{\partial \lambda_2}\mathbf{n_2} \otimes \mathbf{n_2} + \frac{1}{2\lambda_3}\frac{\partial W}{\partial \lambda_3}\mathbf{n_3} \otimes \mathbf{n_3}\right]\mathbf{R} \end{aligned} \tag{1.16}$$

Using the known relation between $\mathbf{F}$, $\mathbf{R}$, and the left stretch tensor $\mathbf{V}$

$$\mathbf{F} = \mathbf{V}\mathbf{R} \tag{1.17}$$

Equations 1.2 and 1.19 become

$$\boldsymbol{\sigma} = \frac{2}{J}\mathbf{V}\left[\frac{1}{2\lambda_1}\frac{\partial W}{\partial \lambda_1}\mathbf{n_1} \otimes \mathbf{n_1} + \frac{1}{2\lambda_2}\frac{\partial W}{\partial \lambda_2}\mathbf{n_2} \otimes \mathbf{n_2} + \frac{1}{2\lambda_3}\frac{\partial W}{\partial \lambda_3}\mathbf{n_3} \otimes \mathbf{n_3}\right]\mathbf{V} \tag{1.18}$$

Using the spectral decomposition of $\mathbf{V}$

$$\mathbf{V}\mathbf{n_i} \otimes \mathbf{n_i}\mathbf{V} = \lambda_i^2\mathbf{n_i} \otimes \mathbf{n_i} \tag{1.19}$$

and

$$J = det(\mathbf{F}) = det(\mathbf{V})det(\mathbf{R}) = det(\mathbf{V}) = \lambda_1\lambda_2\lambda_3 \tag{1.20}$$

Model	Expression for Strain Energy Density function W	Fitting parameters
Polynomial	$W = \sum_{i,j=0}^{n} C_{ij}(\overline{I}_1 - 3)^i(\overline{I}_2 - 3)^j + \sum_{k=1}^{m} D_k(J-1)^{2k}$	$C_{ij}\ i,j = 1...n$ $D_k\ k = 1...m$
Reduced Polynomial	$W = \sum_{i=1}^{n} C_{i0}(\overline{I}_1 - 3)^i + \sum_{k=1}^{m} D_k(J-1)^{2k}$	$C_{i0}\ i = 1...n$ $D_k\ k = 1...m$
Ogden	$W = \sum_{i=1}^{n} \frac{\mu_i}{\alpha_i}(\lambda_1^{\alpha_i} + \lambda_2^{\alpha_i} + \lambda_3^{\alpha_i} - 3) \sum_{i=1}^{n} D_i(J-1)^{2i}$	$\mu_i, \alpha_i, D_i\ i = 1...n$
Arruda Boyce	$W = \mu \sum_{i=1}^{5} \frac{C_i}{\lambda_m^{2i-2}}\left(\overline{I}_1^i - 3^i\right) + D\left(\frac{J^2-1}{2} - \ln J\right)$ $C_1 = \frac{1}{2} \quad C_2 = \frac{1}{20} \quad C_3 = \frac{11}{1050} \quad C_4 = \frac{19}{7000} \quad C_5 = \frac{519}{673750}$	μ, λ_m, D
Van Der Waals	$W = \mu\left\{ -(\lambda_m^2 - 3)[\ln(1-\mu) + \mu] - \frac{2}{3}a\left(\frac{\tilde{I}-3}{2}\right)^{\frac{3}{2}}\right\}$ $+\frac{D}{2}\left(\frac{J^2-1}{2} - \ln J\right)$ $\tilde{I} = (1-\beta)\overline{(I_1)} + \beta\overline{I}_2 \qquad \mu = \sqrt{\frac{\tilde{I}-3}{\lambda_m^2-3}}$	$\mu, \lambda_m, \alpha, \beta, D$

Table 1.1: Hyperelastic material models

Equation 1.18 becomes

$$\boldsymbol{\sigma} = \frac{1}{\lambda_1\lambda_2\lambda_3}\left[\lambda_1\frac{\partial W}{\partial \lambda_1}\mathbf{n_1}\otimes\mathbf{n_1} + \lambda_2\frac{\partial W}{\partial \lambda_2}\mathbf{n_2}\otimes\mathbf{n_2} + \lambda_3\frac{\partial W}{\partial \lambda_3}\mathbf{n_3}\otimes\mathbf{n_3}\right] \tag{1.21}$$

The goal of hyperelastic models is to attempt to adequately approximate the expression of W in equations 1.7 and 1.9. Several models have been developed since the first Neo-Hookean and Mooney-Rivlin models proposed by Ronald Rivlin and Melvin Mooney in 1940-1948([Moo40], [Riv48]). Each one of these models expresses the strain energy density function W using a different form. Table 1.1 summarizes these expressions. More information on these models can be found in [DB06].

A look into the bibliography shows that the "Polynomial model" as well as the "Reduced polynomial" both of order 1 are predominant as choices for seal material modeling due to their simplicity ([SMD04], [WMGK97]).

1.1.2 Neo-Hookean hyperelastic model

A material model analysis detailed further down this document (Section 1.1.3) indicates that, among the models suggested above, the Neo-Hookean hyperelastic model is the best choice for the modeling of the door seal rubber. This model defines the material strain energy $W = W(\overline{I}_1)$ for compressible rubber in the following way:

$$\mathbf{W} = C_{10}(\overline{I}_1 - 3) + D_1(J-1)^2 \tag{1.22}$$

The value C_{10} is an empirically determined material constant related to the distortional response, and D_1 is a material constant related to the volumetric response. From the previous equation we get

$$\begin{aligned} \frac{\partial W}{\partial \overline{I}_1} &= C_{10} \\ \frac{\partial W}{\partial \overline{I}_2} &= 0 \\ \frac{\partial W}{\partial J} &= 2D_1(J-1) \end{aligned} \tag{1.23}$$

And equation 1.12 becomes

$$\boldsymbol{\sigma} = \frac{1}{J}\left[\frac{2}{J^{2/3}}C_{10}\mathbf{B} - \frac{2}{3}C_{10}\overline{I}_1\mathbf{I} + 2D_1(J-1)\right] \tag{1.24}$$

The Cauchy stress is decomposed into its volumetric pressure p, and its deviatoric stress $\mathbf{S}$

$$\boldsymbol{\sigma} = \mathbf{S} - p\mathbf{I} \tag{1.25}$$

where p can be developed for the Neo-Hookean model into

$$p \overset{\text{def}}{=} -\frac{1}{3}tr(\boldsymbol{\sigma}) = -\frac{\partial W}{\partial J} = -2D_1(J-1) \tag{1.26}$$

The final form of the Neo-Hookean equation for Cauchy Stress is

$$\boldsymbol{\sigma} = \frac{1}{J}\left[-p\mathbf{I} + \frac{2}{J^{2/3}}C_{10}\mathbf{B} - \frac{2}{3}C_{10}\overline{I}_1\mathbf{I}\right] \tag{1.27}$$

or

$$\boldsymbol{\sigma} = \frac{1}{J}\left[-p\mathbf{I} + 2C_{10}\overline{\mathbf{B}} - \frac{2}{3}C_{10}\overline{I}_1\mathbf{I}\right] \tag{1.28}$$

If the material is incompressible, then $J = 1$ and $D_1 = 0$, hence

$$\begin{aligned} \boldsymbol{\sigma} &= 2C_{10}\mathbf{B} - \mathbf{p}^* \\ \mathbf{p}^* &= \frac{2}{3}C_{10}\overline{I}_1\mathbf{I} \end{aligned} \tag{1.29}$$

Linearization to Hooke's Law model

The Neo-Hookean model can be linearized around the point of relaxation, so that for small displacements it becomes equivalent to a Hooke's Law model. Considering Hooke's Law expression for Cauchy stress in terms of K and G (respectively the bulk and shear modulus)

$$\boldsymbol{\sigma} = 3Kvol(\boldsymbol{\varepsilon}) + 2Gdev(\boldsymbol{\varepsilon}) \tag{1.30}$$

With $vol(\boldsymbol{\varepsilon}) = tr(\boldsymbol{\varepsilon})/3\mathbf{I}$ and $dev(\boldsymbol{\varepsilon}) = \boldsymbol{\varepsilon} - vol(\boldsymbol{\varepsilon})$. From equation 1.27 and knowing that for infinitesimal strains

$$\begin{aligned} J &\approx 1 + tr(\boldsymbol{\varepsilon}) \\ B &\approx \mathbf{I} + 2\boldsymbol{\varepsilon} \end{aligned} \tag{1.31}$$

We get

$$\boldsymbol{\sigma} = 2D_1 tr(\boldsymbol{\varepsilon}) + \frac{4C_{10}}{J^{5/3}}(\boldsymbol{\varepsilon} - \frac{tr(\boldsymbol{\varepsilon})}{3}) \tag{1.32}$$

If the modeled material is fairly incompressible, then $tr(\boldsymbol{\varepsilon}) \ll 1$ and $J = 1 + tr(\boldsymbol{\varepsilon}) \approx 1$, and so the previous equation becomes

$$\boldsymbol{\sigma} \approx 2D_1 tr(\boldsymbol{\varepsilon}) + 4C_{10}(\boldsymbol{\varepsilon} - \frac{tr(\boldsymbol{\varepsilon})}{3}) = 2D_1(3vol(\boldsymbol{\varepsilon})) + 4C_{10}dev(\boldsymbol{\varepsilon}) \tag{1.33}$$

If we assimilate this equation to that of a linear Hooke's model (1.30), then

$$\begin{aligned} K &= 2D_1 \\ G &= 2C1 \end{aligned} \tag{1.34}$$

Using the known relationships between K and G and the Young's Modulus E and Poisson's ratio υ, we get for a compressible Neo-Hookean material

$$\begin{aligned} E &= \frac{9GK}{3K+G} = \frac{18C_{10}D_1}{3D_1 + C_{10}} \\ \upsilon &= \frac{3K-2G}{2(3K+G)} = \frac{3D_1 - 2C_{10}}{6D_1 + 2C_{10}} \end{aligned} \tag{1.35}$$

However, if the material is incompressible, K tends to infinity, and the previous equations cannot be used. In this case another approach is necessary [YZ09].
It is known that incompressible materials have a Poisson's ratio of $\upsilon = 0.5$. The only remaining parameter is hence E. The known expressions that relate the invariants and the principal stretches are

$$\begin{aligned} I_1 &= \lambda_1^2 + \lambda_2^2 + \lambda_3^2 \\ I_2 &= \lambda_1^2\lambda_2^2 + \lambda_1^2\lambda_3^2 + \lambda_2^2\lambda_3^2 \\ I_3 &= \lambda_1\lambda_2\lambda_3 \end{aligned} \tag{1.36}$$

and the conditions for uniaxial extension are

$$\begin{aligned} \lambda_{11} &= \lambda \\ \lambda_{22} &= \lambda_{33} = \sqrt{\frac{J}{\lambda}} \\ \sigma_{22} &= \sigma_{33} = 0 \end{aligned} \tag{1.37}$$

Supposing in-compressibility ($J = 1$) we can obtain the equivalent Young's modulus from equations 1.10,1.21, 1.22, and 1.36

$$\sigma_{11} - \sigma_{33} = \sigma_{11} = \lambda_1 \frac{\partial W}{\partial \lambda_1} - \lambda_3 \frac{\partial W}{\partial \lambda_3} = 2C_{10}\big(\lambda^2 - \frac{1}{\lambda}\big) \tag{1.38}$$

For small displacements $\varepsilon_{11} = \lambda - 1 \ll 0$ and the previous equation becomes

$$\lim_{\varepsilon \to 0} \sigma_{11} = 2C_{10}\left(\frac{\varepsilon_{11}^3 + 3\varepsilon_{11}^2 + 3\varepsilon_{11}}{\varepsilon_{11} + 1}\right) = 6C_{10}\varepsilon_{11} \tag{1.39}$$

Which finally leads to the Young's Modulus E determination

$$E = \frac{\sigma_{11}}{\varepsilon_{11}} = 6C_{10} \tag{1.40}$$

1.1.3 Choice of a hyperelastic model

Table 0.1 summarizes the information we have on the materials found in the seals for a static analysis. As it has already been explained and due to the lack of material information, the TPE in the window seals will not be modeled through a hyperelastic model but through its Hooke's law parameters.

Additionally, we can observe that the only information on the static behavior of the EPDM incompressible rubber is the coefficients of the Neo-Hookean material model. Because the part of the door seal that is made from this kind of material doesn't undergo very large deformations, we will assume that this hyperelastic model is sufficiently accurate.

Finally, the table shows that for the foam EPDM which, given that it endures the largest deformation, is the most important material in this seal, we only have experimental data. In consequence an appropriate hyperelastic model should be chosen among those shown in Table 1.1.

For this matter, a material model evaluating tool in ABAQUS has been used. This tool uses least-square regression to determine the coefficients needed in the strain energy density expressions found in Table1.1 that will better represent the behavior of the experimentally characterized material.

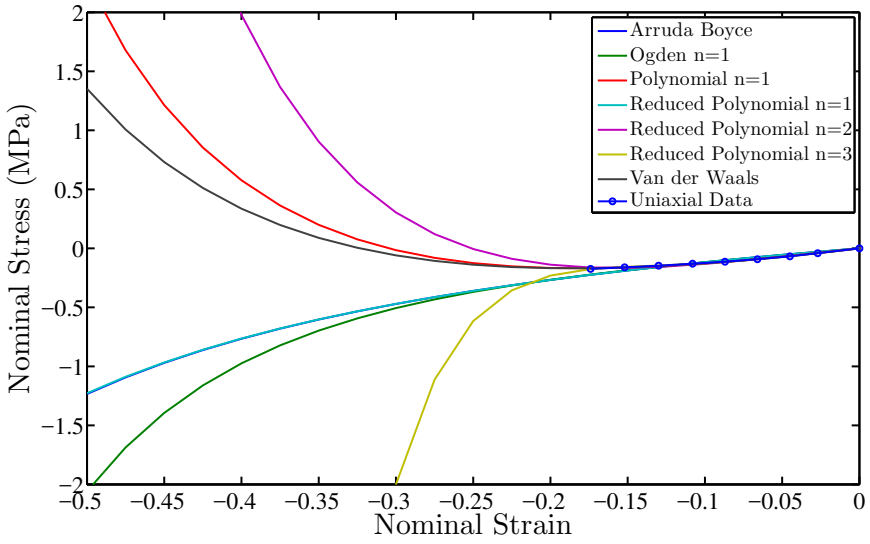

Figure 1.1: Uniaxial compression curves for some hyperelastic material models

Figure 1.1 shows the calculated strain-stress relationship found for some of these models. As we can see, some of the material models exhibit a strange behavior for high compression strains. When the material is uniaxially stretched (positive stress), it shrinks in the axial direction (negative strains). Due to the limited amount of experimental data points the material information is given only up to -0.2 MPa. The information for higher compressions must thus be predicted by fitting each material model's parameters, using a least-square regression over the experimental points. This leads to solutions that, as we can see, are not physically coherent. We call these material models "unstable" for the specific given material data. By, removing these "faulty" material models we reduce the number of possible models to 4.

- Reduced Polynomial with $n = m = 3$ (Also called Yeoh hyperelastic model)
- Reduced Polynomial with $n = m = 1$ (Also called Neo-Hookean hyperelastic model)
- Ogden $n = 1$
- Arruda Boyce

We observe a different behavior between the first of these models and the last three in the strain-stress and pressure-volume ratio curves of Figures 1.2 and 1.3. For volumetric compressions (Figure 1.3) the Yeoh model seems to coincide with the experimental data, while the other three, although they follow the tendency of the experimental curve, do not succeed in representing it accurately. When we focus on

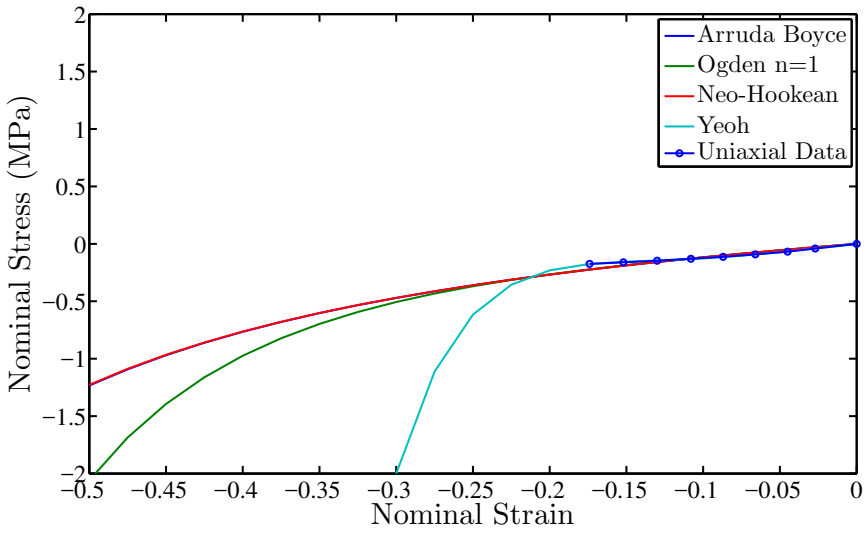

Figure 1.2: Uniaxial compression curves for stable hyperelastic models

the uniaxial compression in Figure 1.2 these last 3 models fit the data points in a similar way and only diverge slightly for high strains. The fit is fairly good but far from exact. The Yeoh model however, succeeds in representing the tendency of the experimental data points. Nevertheless, in this model we can observe that, because of the higher order polynomial fit, the predicted curve for high compression strains drops drastically to large compressive stresses. This again is due to the least-square regression of the experimental points, and experience tells us that this prediction is bound to be incorrect. To compare the effect of these models on our specific case, we model the seal using each one of these 4 options. For each modeling scenario we output the force applied by the door to the seal during compression. To these, we add the results for a linearized Hooke's Law, using the coefficients in Table 1.3 obtained through the procedure detailed earlier in this chapter. Figure 1.4 shows the comparison for resulting reaction forces using these material models. This analysis has been made with a 2D model for simplicity and, in consequence, the resulting reaction force is calculated over a section of only 1mm. As we can see, the differences between them are negligible. Additionally, the time cost of each model is summarized in Table 1.2.

As a result of this material model analysis, in a choice of the best accuracy-predictability-simplicity-cost balance we decide to use the Neo-Hookean model, which we consider fairly accurate, with only 2 coefficients and no sudden changes in stiffness, all the while being the fastest option.

Table 1.3 summarizes the complete material information used for the static study, including the calculated coefficients for the hyperelastic model and its linearization

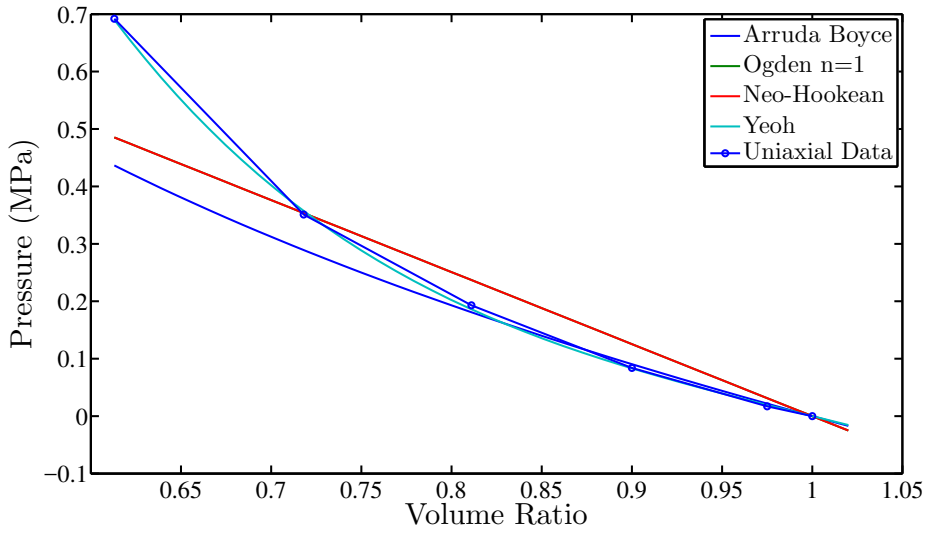

Figure 1.3: Volumetric compression curves for stable hyperelastic models

Material model	Time(s)
Yeoh	105
Ogden n=1	92
Arruda Boyce	89
Neo-Hookean	76
Hooke's Law	115

Table 1.2: Time cost of seal compression simulation for each material model

to a Hooke's Law model.

1.2 Implementation of the Finite Element Static Model

It has been explained earlier that, given its complex geometry, the seals need to be represented by a fine mesh. Given the tubular shape of the seals, we have decided to model every step in 2D, which will greatly reduce the number of dof, and hence, simulation cost. Note that this simplification doesn't consider the discontinuity of the steel reinforcement described in the Introduction, and implies not taking into account the out-of-plane acoustical radiation of the seal section. We believe that this description is however sufficient for cases where the interest is the general behavior of the seal, such as the optimization procedure considered here.

The seals have been modeled via the finite element software used by PSA Group

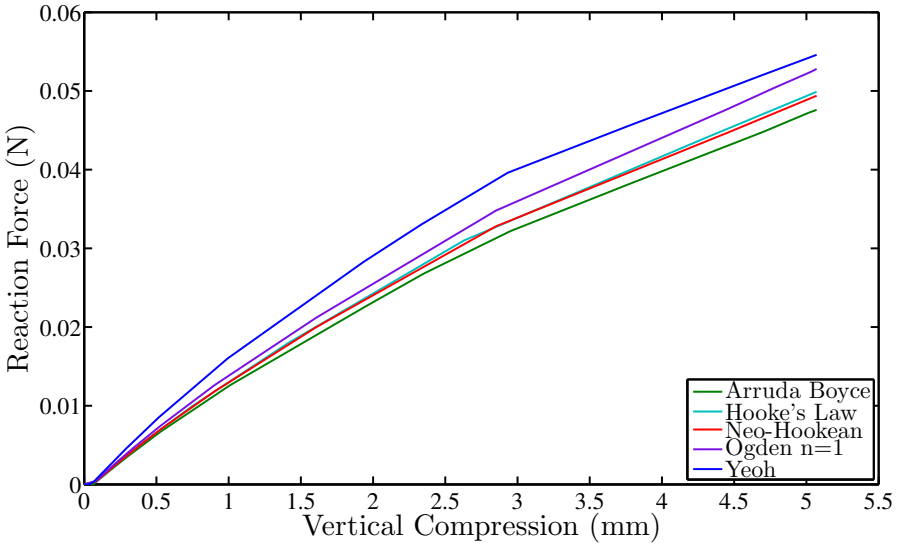

Figure 1.4: Reaction force on door throughout seal compression for several material models

ABAQUS, which can simulate both static non-linear deformation and acoustic excitation. However this software presents some limitations. It has already been stated that door and window seals go through several phases. First a static step, where seals are positioned on their respective frames and the conditions previous to the aerodynamic excitation are simulated (door compression, window insertion...), and later a dynamic step, where the acoustical sources are considered. Yet these two steps cannot be modeled together. As we can see in Figure 1.5 the acoustic excitation requires that the cavities inside the seal, as well as a section of the air before and after the seal in the acoustic transfer path, be represented and meshed with acoustic elements. In ABAQUS, all the meshed parts must be introduced at the beginning

	Incompressible EPDM	Compressible EPDM	Homogenized TPE	Steel
Density	1e-9 T/mm^3	6.7e-8 T/mm^3	1e-9 T/mm^3	7.7e-9 T/mm^3
Strain-Stress behavior	Neo Hookean: $C_1 = 0.8$ MPa $D_1 = 0$ MPa Hooke: E=4.8 MPa $\upsilon = 0.5$	Neo Hookean: $C_{10} = 0.175$ MPa $D_1 = 1.595$ MPa Hooke: E=1.01 MPa $\upsilon = 0.45$	Hooke: E=60 MPa $\upsilon = 0.48$	Hooke: E=2,1e5 MPa $\upsilon = 0.3$

Table 1.3: Material information for static analysis

of each model, and cannot be added later. Thus, if the static and acoustic steps are simulated in the same model, the parts that are only necessary in the acoustic step must be introduced and meshed from the beginning, in the static step. This introduces several problems, especially for door seals:

- It has already been explained that the seals have some perforations along their extruded axes, so that the air inside the interior cavities is not trapped inside these cavities during compression, creating a pneumatic pressure that could interfere with the seals' aptness to prevent leakage. However, since the modeling is done in 2D, these perforations are not represented. As a consequence in the model, the acoustic cavities inside the seal are not connected to the exterior air cavities, thus, when the compression takes place, the air is not leaked to the exterior and hence, the pneumatic pressure inside the cavities modify the resulting seal deformation and yield the model not representative of the 3D structure.

- The additional meshed parts lead to a relevant increase in number of dof, unnecessary to the Static Modeling of the seal

- When the door seal is compressed, an important deformation takes place and thus the nodes in the seal undergo relevant displacements. Some of those nodes are in contact with the fluid meshes, and as a consequence, the geometry of the air cavity changes, and so its mesh must change too. The acoustic elements in ABAQUS do not have mechanical behavior and, therefore, cannot model the displacement of the fluid when the structure undergoes large deformation. An adaptive Lagrangian-Eulerian mesh would be hence necessary. This approach would, at each seal compression increment, re-mesh the acoustic cavities with a mesh that uses the same topology as the original mesh, but with the nodal locations adjusted so that the deformation of the structural-acoustic boundary would not lead to severe distortion of the acoustic elements. However, the model resulting from the use of this method is difficult to converge and in doing so it leads to a severe increase in simulation cost. Additionally, the first point would still be problematic.

As a solution, the simulation is divided into a static model and an acoustic excitation model, which will be simulated one after the other. In the first one, only the parts necessary to the static step are modeled. Insertion, relaxation and compression are applied. The resulting deformed mesh and its stress distribution are then exported into the initial state of a new model, where the seal will already be deformed and under a constrained state. The acoustic parts are then meshed around and inside the already deformed geometry, bypassing all three of the issues described above. This approach is used for both window and door seals, and summarized in schema 1.6. However, even with this solution, ABAQUS doesn't allow re-meshing of the parts exported from the static simulation. In consequence, the seal imported into the acoustic model will have the same mesh as the one in the static step. This means

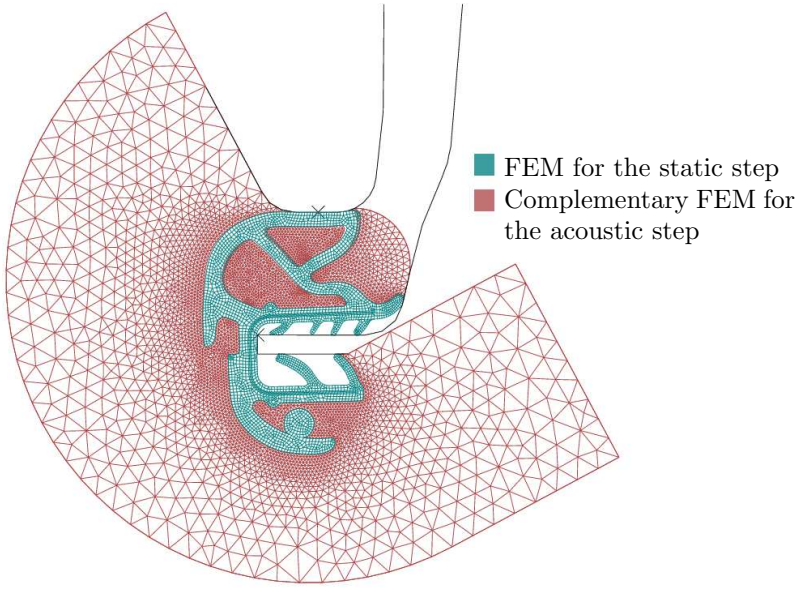

Figure 1.5: Elements needed for only the static step and additional acoustic elements for a static+acoustic model

that the choice of the correct mesh size for the frequencies of acoustic excitation must be taken into account from beginning of the static step. As a general approach, the correct size of an acoustic mesh is of, at least, 6 nodes per wavelength. Given that the speed of sound in rubber is of about 1610 m/s, and that the maximal frequency to which the seal is submitted for aerodynamic excitations is 10000Hz, the smallest wavelength is 161mm and the largest element size should not exceed 27mm.

1.2.1 Door Seal FE model

The modeling of the door seal starts with the importation of the geometry of this element into the software ABAQUS. Next, this geometry is meshed with mainly rectangular elements, which are recommended for mechanical problems, with linear interpolation. Given that the displacements during the seal compression are important in very deformed zones, such as the lips, and because some parts of the seal rotate importantly without deformation, the size of the elements must be small enough so that its nodes can follow these large displacements without compromising convergence. Additionally, the steel reinforcement is very thin and an extremely fine mesh is needed in order to be able to represent it with several elements along its width. However, such a fine mesh applied to the entire seal adds an important amount of dof to the model, and the cost of the simulation rises. As a solution, the general mesh size has been fixed at 0.6mm for the seal, and some refinement has been applied around and inside the steel reinforcement, as well as inside the lips, to facilitate convergence in these sensitive zones. From the mesh restrictions for the

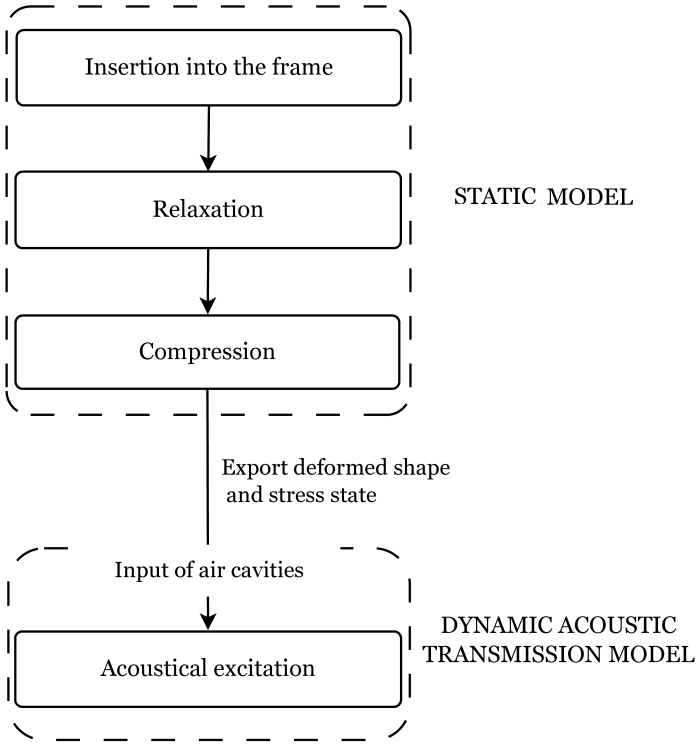

Figure 1.6: Schematics of the Transmission Model

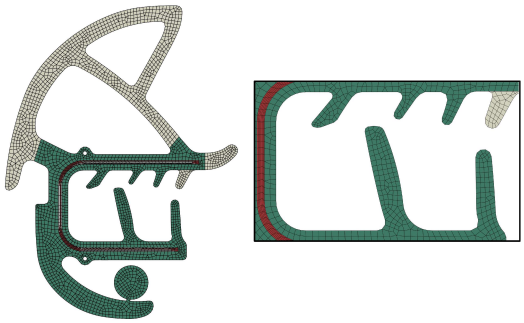

Figure 1.7: Door seal mesh

acoustical model described in the previous paragraph, we deduce that the element size is small enough for the acoustical mesh. The resulting mesh can be seen in detail in Figure 1.7.

Throughout the modeling of the different steps of the static part, we encounter several software limitations around which we have to build our way. The resulting process is described below.

Insertion

As explained in the Introduction, the first phase the seal undergoes is its insertion into the door frame. In reality, this is achieved by pushing the seal until it is clamped around the edge of the frame. However, numerically this implies that all its nodes have to move several centimeters throughout the insertion. Given that the general mesh size is of 0.6mm, this displacement implies an important amount of small increments for convergence. Consequently, the model is built so that it is the frame that advances to meet the seal instead of the other way around. The frame is modeled as a rigid solid, with only one node to drive its imposed displacement; hence this approach is much less costly.

The interaction between the frame and the lips of the seal has to represent that of a rubber-metal contact, where the tangential friction is fairly significant. This is done via a penalty contact, with an approximated friction coefficient of 0.5.

The real contact between the lips and the frame is staggered. That is, when the frame moves to meet the seal (to the left in Figure 1.8.a), it encounters each of the 6 lips from the side, one at a time. This yields the contact hard to manage, and the simulation becomes costly and converges with difficulty. To help with convergence, the frame is divided into its upper and lower parts. The former moves sideways [1]

[1] The orientation of the seals and window is different in each specific model for clearness. In general, when describing a model, the directions (vertical, horizontal, sideways....) are taken with respect

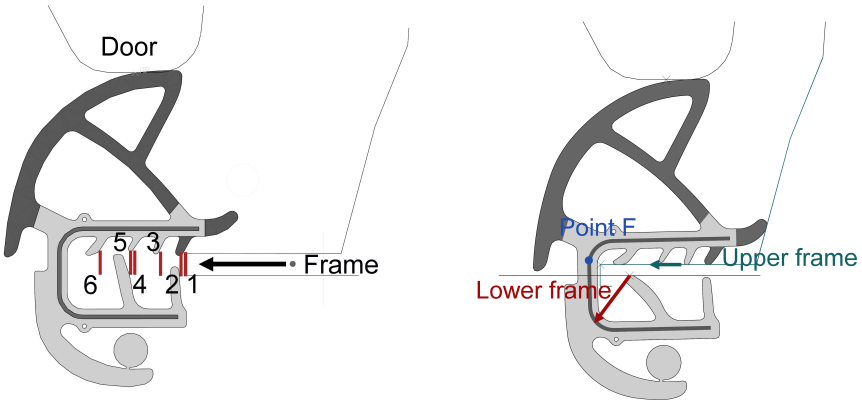

a) b)

Figure 1.8: a) Staggered contact between the lips and the frame. b) The upper and lower frames accompany the deformation of the lips which leads to easier convergence.

whereas the latter moves both sideways and downwards, pushing the seal downwards with it. This way, both upper and lower contact surfaces meet with their corresponding lips of the seal in a diagonal direction, instead of a purely horizontal one, and the simulation converges easily (Figure 1.8.b).

To prevent the seal from moving during insertion, the rotation and horizontal movement of the seal are fixed in point F (Figure 1.8). Only the vertical translation dof is free.

In prevision of the upcoming compression, which will be simulated in the same model, a rigid solid, driven by a reference node, is inserted simulating the door of the car. However, no displacements or interactions are applied on this solid until the compression phase.

Figure 1.10.a shows the stress distribution of the seal at the end of said phase.

Relaxation

After the insertion, the external forces should be released to allow the seal to reach an equilibrium state where the internal forces are balanced. For this, point F should be free. Without applying any external forces, stresses are redistributed and a state of equilibrium is achieved. In Figure 1.10.b we can observe this relaxation, mainly near point F, where the seal separates from the frame, and on the horizontal lip-like element that is compressed against the upper frame, which is what forces this

to the models coordinate system, not to the real orientation of the element in the car structure

separation.

Compression

The model is built to simulate 4 different states of vertical compression: the nominal (H1), the higher and lower tolerances (H2 and H3) and an extreme case (H4). Figure 1.9 summarizes these states.

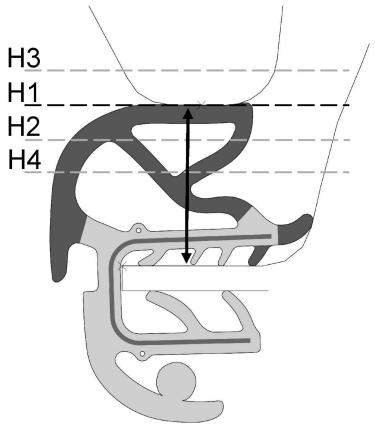

	Seal gap distance (mm)
H3	18.2
H1	16.2
H2	14.2
H4	12.2

Figure 1.9: Different states of vertical compression

The contact between the seal and the door, as in the case of the support, is rubber-metal. In consequence, the friction is modeled with the same penalty coefficient of 0.5, as in the case of the frame-seal contact.

In this step a vertical displacement is imposed on the door, its magnitude dependent on the case (H1, H2, H3 or H4). Figure 1.11 shows the compression results for H2, H3 and H4. We will hereinafter and for the remaining chapters focus on the modeling of the nominal case H1. Figure 1.10.c illustrates the deformation and stress state at the end of this step. It is this state that will be imported later on into the acoustic model.

1.2.2 Window Seal FE model

The process for the FE modeling of the window seal is similar to that of the door seal. Using the same element types and maximal mesh size as for the door seal, the chosen general size is of 0.7mm, and the resulting mesh is depicted in Figure 1.12. From the static phases described in in the Window Seal section of the Introduction we get:

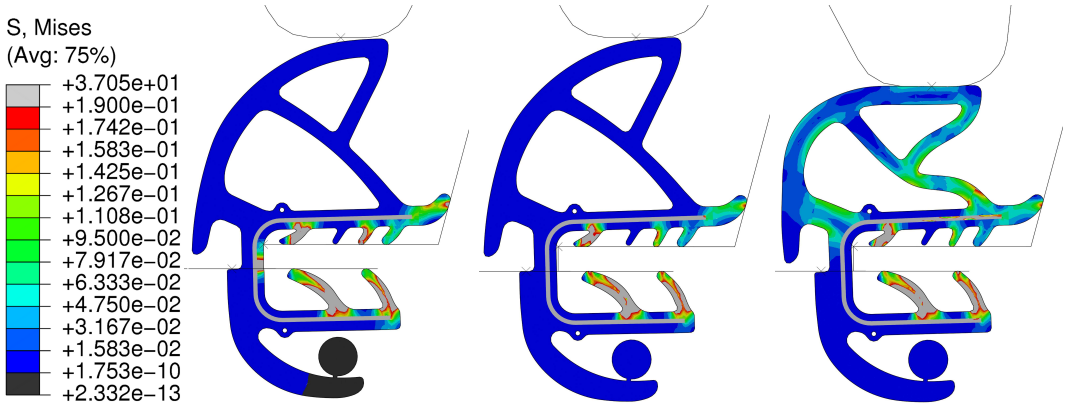

a) After insertion b) After relaxation c) After compression

Figure 1.10: Numerical results of the door seal after each phase

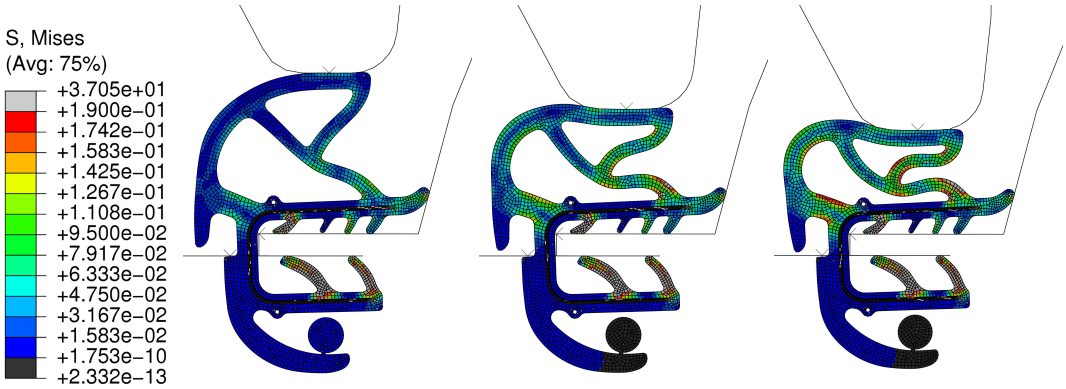

a) H3 compression b) H2 compression c) H4 compression

Figure 1.11: Numerical results of the door seal for each level of compression

Seal Insertion

Contrary to the door seal, the window seal doesn't have lips on the section where it is inserted onto the frame, and it behaves mainly as a rigid solid throughout its insertion. Hence, for simplicity this phase is not simulated in detail. Instead, some fixed boundary conditions are applied on the surfaces of the seal in contact with the frame, as depicted in Figure 1.13. Due to this simplification, the relaxation phase is omitted.

Window insertion

The lips on the window seal are used to accommodate the window inside the seal, so that there are no water or sound leaks when the window is rolled up. Similar

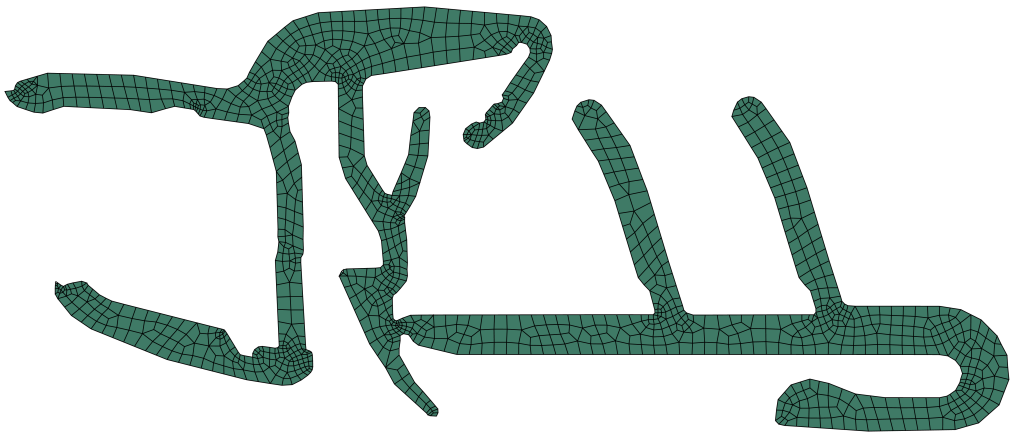

Figure 1.12: Resulting window seal mesh

to the door insertion, the window is pushed into the seal by applying an imposed horizontal displacement from right to left. In reality the other side of the window is subjected by an unknown element of the car. This element applies a momentum that (in approximation) prevents the window from moving vertically and from rotating. Therefore, in the model, the vertical and rotational dof of the window are blocked. The final state of the assembly is shown in Figure 1.14.

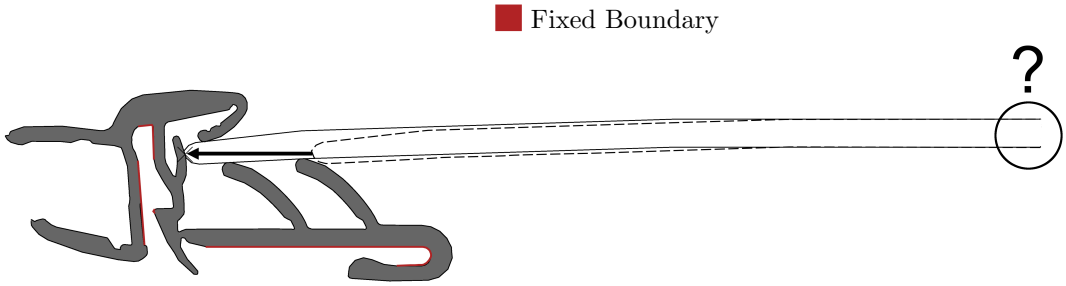

Figure 1.13: Window insertion

1.3 Experimental Validation

To ensure the accuracy of the previous resulting model, an equivalent experimental prototype must be tested, and its experimental results compared to the numerically obtained data. We have chosen to do these tests on the door seal, due to its additional compression phase and its non-linear material model. We assume that by validating

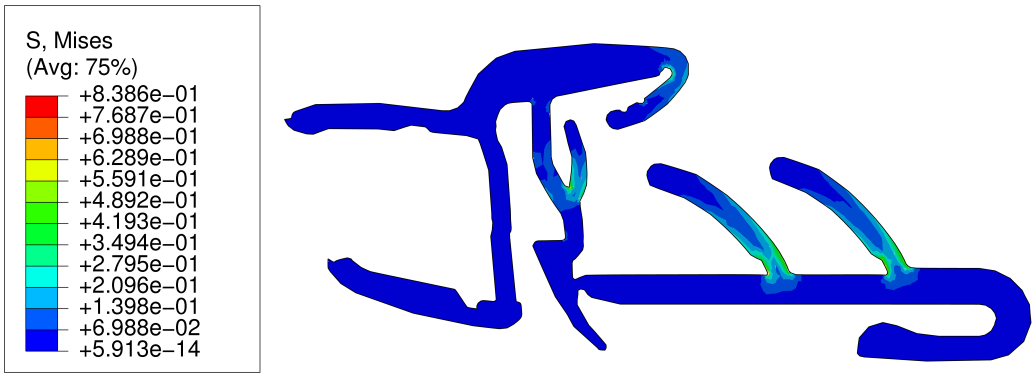

Figure 1.14: Resulting window seal stress

this model we also validate the modeling tools used in its conception, and thus the window seal model which is built using the same or similar tools. The set-up used for the experimental tests has been designed specially for this study. The geometry of the elements surrounding the seal in this setup (the door and the frame) is slightly different from the real seal-door-frame assembly. The original geometry is difficult to manufacture from metal, and thus some minor modifications have been made to facilitate the fabrication of the experimental setup. However, these tests are conceived to endorse the modeling choices made in the construction of the numerical model (contact modeling, material model choice, software-specific elements, etc.), and not to reproduce the exact behavior of the real seal-door-frame assembly. Thus, it suffices to adapt the geometry of the frame and the support in the numerical model to fit that of the experimental set-up, and these modeling choices can still be validated. Figure 1.16 illustrates the resulting numerical model.

Two forms of validation have been designed for this model. It has already been explained throughout this chapter that the compression of the door leads to a deformation of the seal as well as a new stress field inside its section. These are, hence, the two criteria for our validation. Deformation can be validated through the methodology used in [ZZHW03] and detailed in the next paragraph. For the stress field however, experimentally determining stress distribution on the entire studied section of the seal has proven highly difficult. Instead, the magnitude of the vertical component of the reaction force of the seal against the door during compression will be used.

The experimental set-up is depicted in Figure 1.15 and is made through subtractive manufacturing of aluminum. The upper part simulates the door. A section of the seal of 290 mm of length is placed on an intermediate part that simulates the frame and that is connected to a third, fix part called the base, through 4 springs. A displacement is imposed on the door by a screw system on top of the door part. When this happens, the door compresses and deforms the seal. The applied pressure is

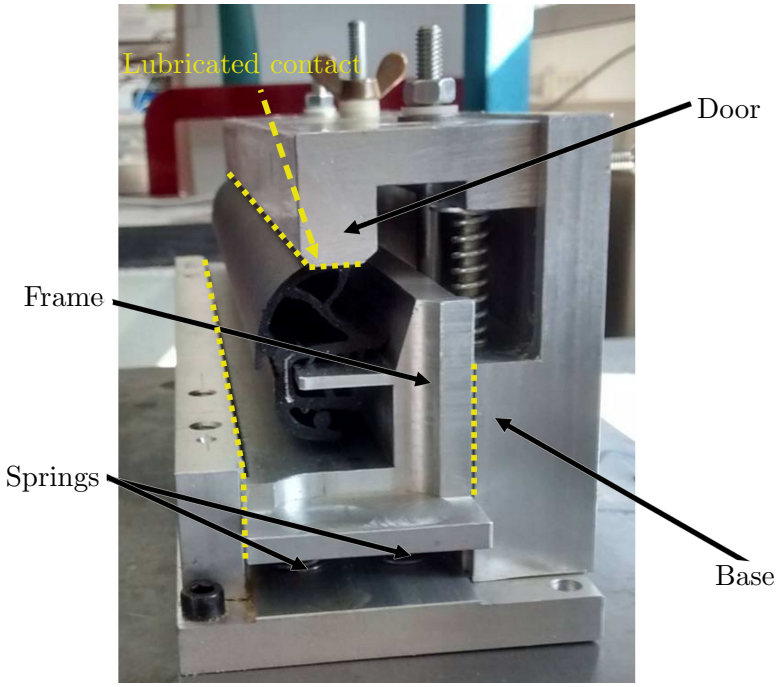

Figure 1.15: First experimental setup for the validation of the Static Model

transmitted onto the frame part through the seal, and the four springs shorten (Figure 1.15). These are the elements that will allow us to output the reaction force mentioned in the previous paragraph. To ensure that there are no vertical contact forces that can interfere with this measurement, all contact surfaces in-between the 3 parts are lubricated. Since we don't have the means to control the contact properties between the upper part of the seal and the door, the friction coefficient of the experimental setup is unknown. As a solution, this interface is lubricated also so that the contact can be simulated in the numerical model using a small coefficient for the penalty contact condition. Since the goal of the experimental test is only to validate the numerical model and not to represent the real conditions of the seal when it is placed in the car, this lubrication is not taken into account in the Static Model.

Deformation validation

In the first place, the level of deformation is validated by following the displacement of 10 points in the seal. These points are chosen to represent as well as possible the general geometry of the upper part of the seal, and are marked on one of the faces of a 290 mm section of the studied car door seal, as seen in Figure 1.17.

For every few mm of imposed displacement on the door, a photo is taken. These are later processed, and the coordinates of each point noted. The goal is to compare the displacement of these points to those of their equivalent counterparts in

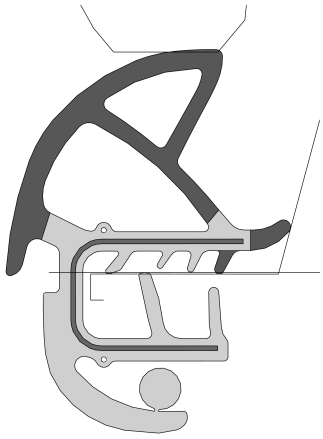

Figure 1.16: Modified numerical model for experimental validation

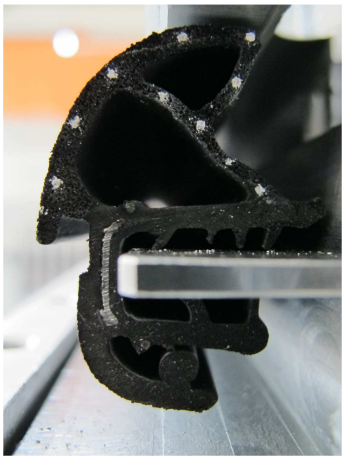

Figure 1.17: Chosen representative points for deformation validation

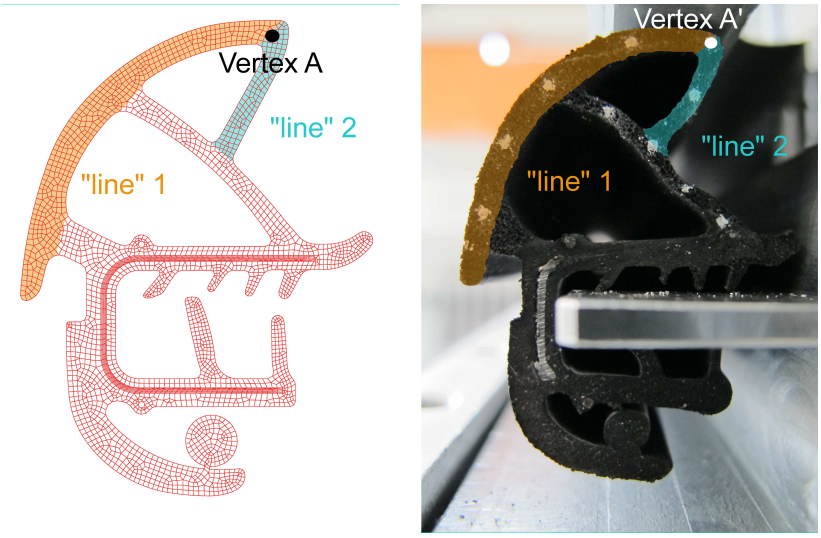

Figure 1.18: Numerical and physical seals with their equivalent geometric elements

the numerical model. However, due to the dispersion in fabrication, the geometry of the experimental seal doesn't correspond to that of the numerical model, as seen in Figure 1.19.a, making the choice of control points difficult. Hence we have decided to choose points in the numerical model similar to those on the physical seal, if not geometrically coincident. That is, points which we expect to have similar behavior.

As an example Figure 1.18 shows both the numerical and the physical seals. The part of the seal that is made of compressible rubber is formed by a series of rubber "arcs" or "lines". In the image we have shaded, in two different colors, two of these "lines" of the numerical seal as well as their equivalent sections in the physical seal. The point where these two "lines" meet, we have called a vertex. In the numerical seal, this vertex is marked in black and named vertex A, and in the physical seals, the equivalent vertex is marked in white and called vertex A'. Figure 1.19.b shows the superposition of the numerical and the physical seal with these two vertices, where we see that they are not coincident. However, we expect point A' on the physical seal to have the same behavior as point A in the numerical model, because they are both vertices of two geometrically equivalent zones of the experimental and numerical seals respectively. In the same way, the points at other intersections of "arcs" or "lines" on the seals will have the same behavior in the numerical model and in the physical setup. Using this "equivalent geometry" criterion, we can find points that behave in the same way, in the numerical model and physical setup, even if they are not exactly in the same physical coordinates when we superpose the two geometries.

The chosen points are monitored on the numerical model throughout the compression, and their trajectories are compared to the experimental results (Figure 1.20.b). Because of the differences in the geometries explained above, we can see that the

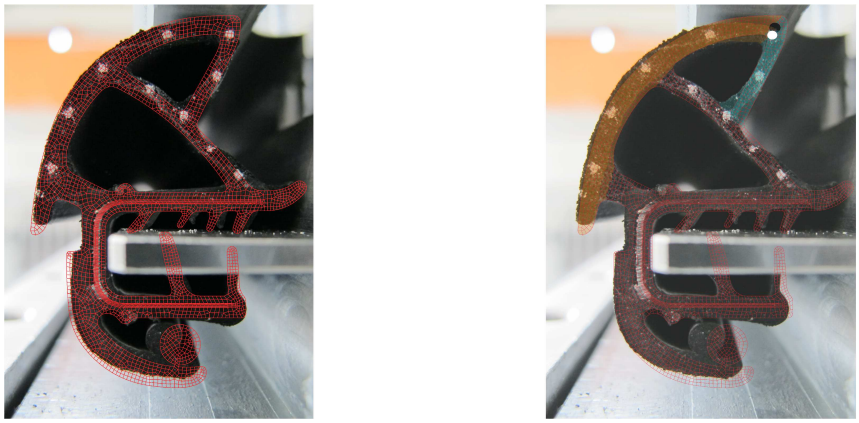

a) b)

Figure 1.19: a) Non-coincident seal geometries. b) Non-coincident equivalent vertices

trajectories of the chosen points don't superpose. To solve this, we shift the starting position of the numerical trajectories to fit that of their corresponding experimental data, for each one of the 10 control points in the seals. We get the results on Figure 1.20.b. We observe that the correlation between the numerical model and the experimental data is remarkably good. However, the points of the numerical model seem to descend further than those on the experimental data, even though the final compression is supposed to be the same. This is due to the fact that it is difficult to determine when the compression of the seal starts in the experimental set-up, when the door part is exactly aligned with the upper part of the seal without compressing it. As a consequence, even if we impose a displacement on the door of 7.5 mm, if door and seal are not in contact at the beginning, the first mm don't compress the seal, an thus the total displacement of the experimental control points is smaller. Nevertheless this doesn't invalidate the results, and hence we can conclude that the deformation of the seal when the car door is closed is well represented by the numerical model that we want to validate.

Stress validation

As explained earlier in this chapter, when the seal is compressed in the set-up it transmits the force onto the support, which results in the deformation of the 4 springs. The amount of deformation allows us to calculate the force applied to the door when a certain displacement is imposed, and consequently the reaction force that the seal has to apply back to reach static equilibrium. However, several tests have proven that the experimental setup, while fitting for the deformation validation, is not accurate in the determination of this reaction force. The experimental prototype is faulty, the lubricant between the different parts is not enough, and some unwanted friction, and eventually self-retention phenomena, appear between the sliding parts of the proto-

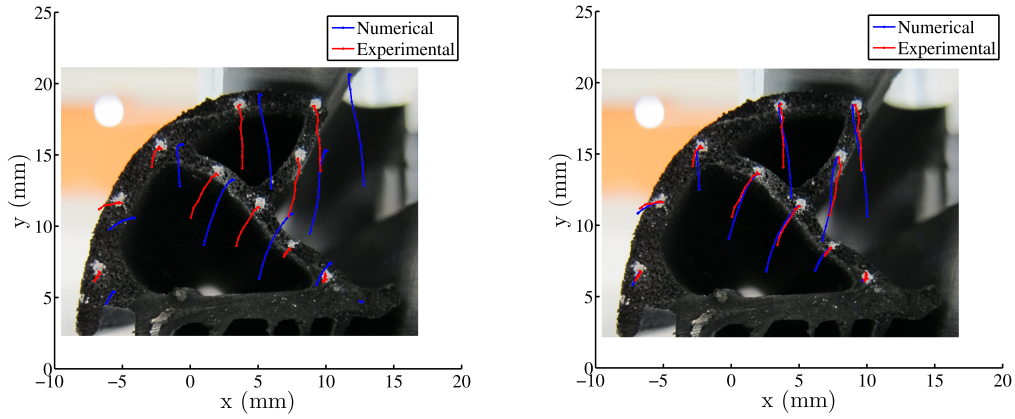

a) b)

Figure 1.20: a) Displacement of control points throughout compression. b) Displacement of control points throughout compression with shifted initial coordinates

type at high compressions (support-base contact). This generates an upward force to the part playing the role of the support, which counteracts part of the applied compression effort. As a result, the force on the springs between the base and the support is reduced, and smaller than the compression force that we want to measure, and so the measuring system is no longer valid. To solve this, the more efficient experimental set-up on Figure 1.21 has been designed. The new prototype is based on the same method: the door displacement is enforced by a turning screw, imposing a compression force on the seal. The latter deforms and transmits the effort onto the support, which at the same time transmits it to 4 springs located between its bottom and the base. However, this time the 3 elements (door, support, base) are connected through two long vertical axes and a system of linear bearings that minimizes friction and prevents blocking. Given that the model is 2D, the reaction force calculated from the deformation of the springs is multiplied by the length of the section of physical seal, that is, 290mm. As explained above, due to the unknown real coefficient on the door-seal experimental setting, the surface intervening on this contact has been lubricated as an attempt to yield the experiment numerically reproducible with small friction coefficients.

For the experimental validation we have tested several sections of different seal profiles (see Figure 1.22 for the definition of section and profile). Figure 1.23 shows the results of the tests on these sections, where the notation P1S2 references the tests on seal profile 1, section 2. As expected, we observe similar results for sections coming from different profiles, although some dispersion appears. The fact that two sections come from the same profile (J1S1, J2S2 and J2S1 J2S2) doesn't seem to imply similar results. This leads us to the consideration of experimental error. Some results

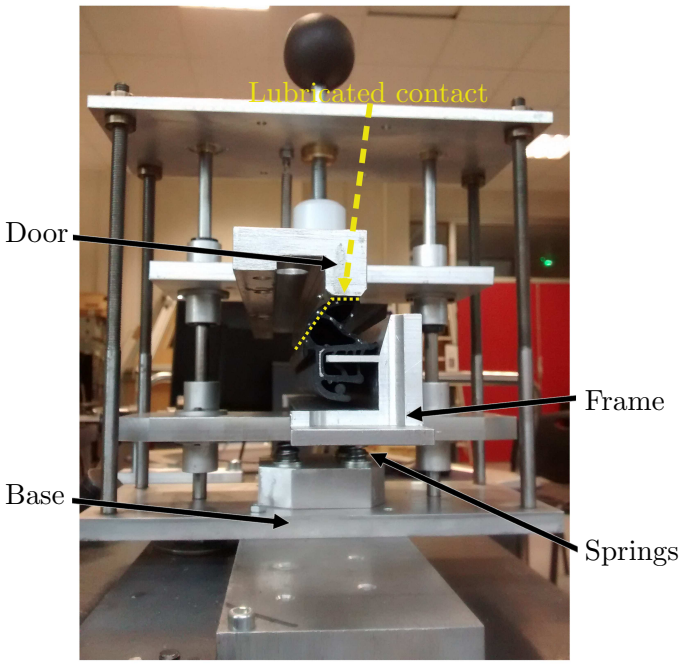

Figure 1.21: Experimental setup for stress validation

of repeatability are shown in Figure 1.24. As we can see, an important part of the small dispersion is due to experimental error, given the simplicity of the experimental set-up. The rest can be either from fabrication dispersion between seal profiles, or from the fact that, since the steel reinforcement is not continuous throughout the seal profile, the properties of the section will vary depending on where the cut was made. However, we still consider the dispersions as small enough for the curves to be representative of the behavior of the door seal.

These results need to be compared to those obtained from the numerical model. For simplicity, the mean of all the experiments will be used as a guide on what the shape of the reaction force should be, and the highest and lower experimental curves will define an interval on where the values of the curve should be found. These values and the comparison to the numerical reaction force are shown in Figure 1.25.

The resulting curves are neither of the same order nor have the same curvature. In the numerical model, stiffness is almost constant throughout the compression, while in the experimental the seal seems to soften with deformation. In a more meticulous analysis of the tests we observe 3 things:

- The geometry of the numerical seal provided by PSA Group doesn't exactly match that of the physical seal.
- When the seal is compressed it has an unpredicted counter-clockwise rotation.

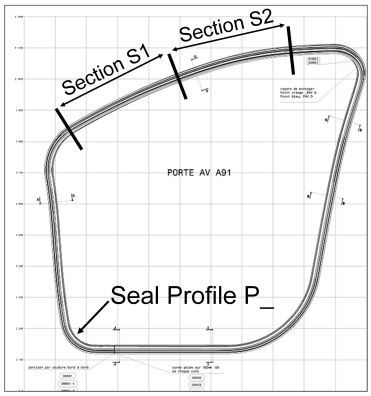

Figure 1.22: Seal profile and seal section definitions

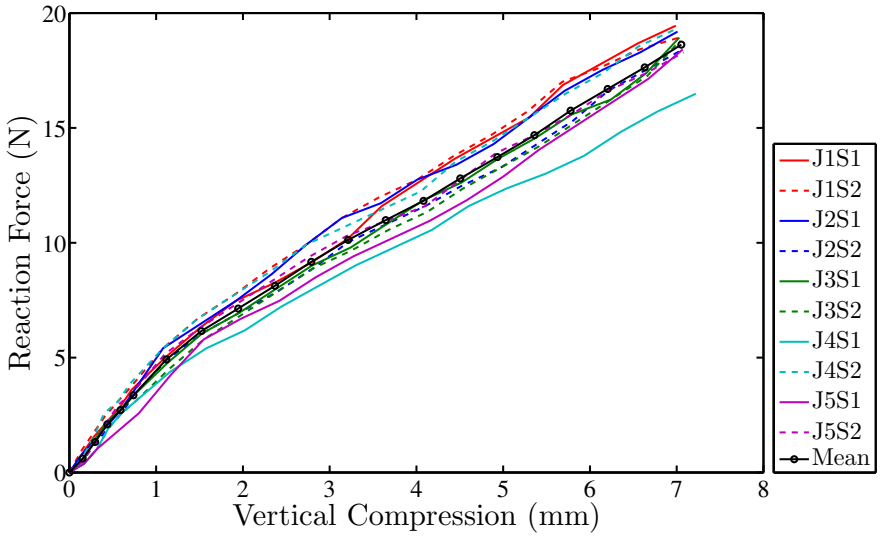

Figure 1.23: Results of experimental tests for stress validation. Different profiles and sections

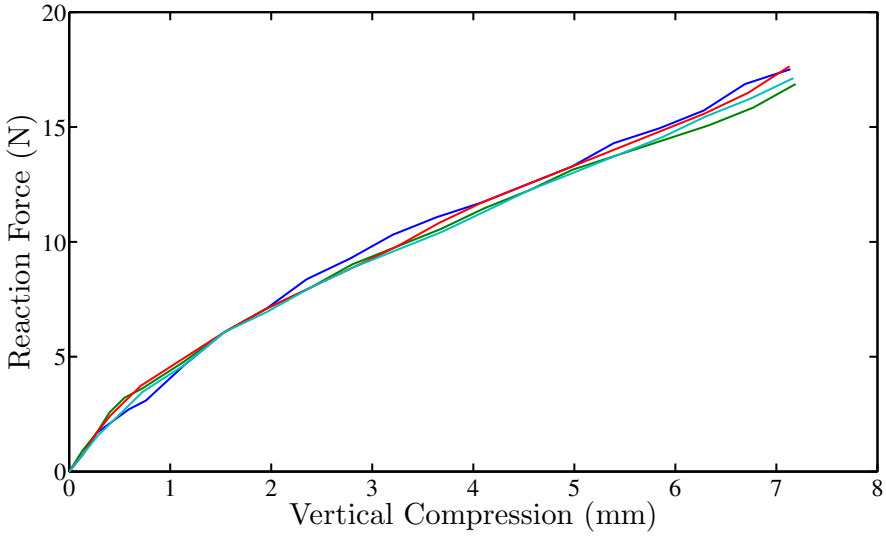

Figure 1.24: Repeatability tests on P2S2

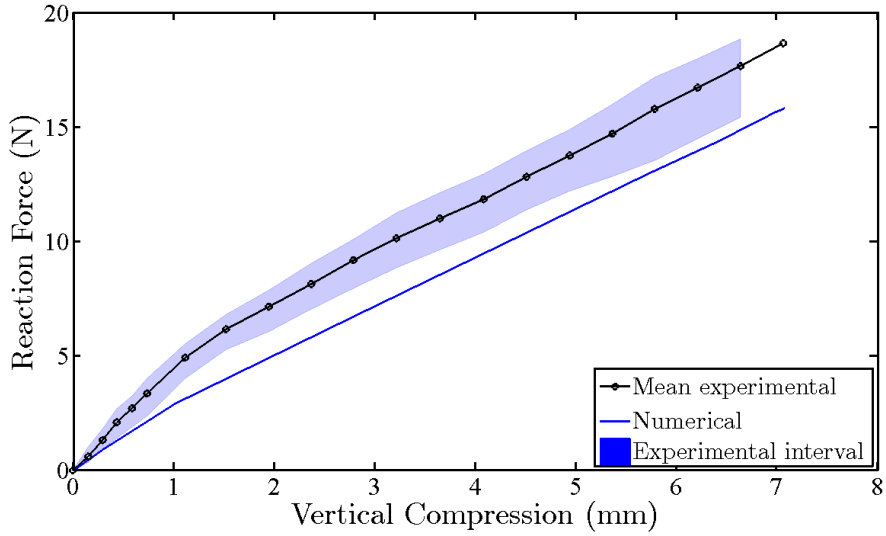

Figure 1.25: Experimental reaction force vs numerical reaction force

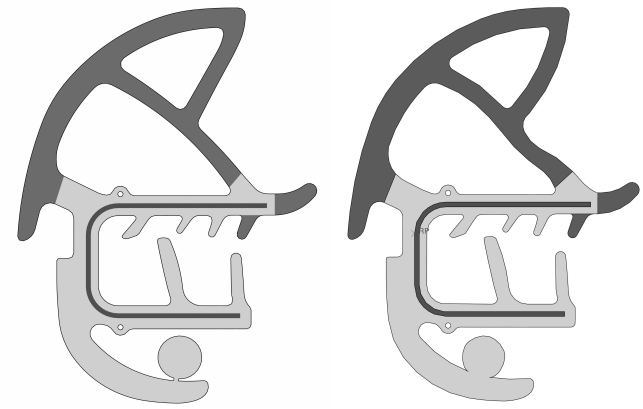

Figure 1.26: Original (left) and modified (right) geometries of the door seal

- The difference between tests with and without lubricant is of the same order than the difference between seal sections (Figure 1.27)

The first issue gives rise to a parametric analysis of the geometry of the seal, which we have described in detail later in this chapter. This leads to the redefinition of the seal geometry in the numerical model, so that it matches more accurately that of the physical seal (Figure 1.26). We will henceforth keep this modified geometry for all remaining models. The resulting reaction force for the modified numerical model is depicted in Figure 1.28.

The second issue is the rotation of the physical seal that takes place in the experimental tests, which is not predicted by our numerical model. Because the lips are very thin and small, the fabrication is imprecise and its dispersion high, yielding its modeling difficult. Being very thin makes them deform severely, this deformation determining the final position of the seal. Because of the inexact modeling of the lips, the rotation, due to their deformation, taking place in the experimental set-up is unaccounted for in the numerical model. To solve this, in the absence of a precise geometry of the lips, we have tried modifying the angle of the compression of the door. If the seal tilts counter-clockwise at an angle, its vertical axis will be tilted to the left, and unaligned with respect to the direction of the door compression. This is equivalent to tilting the door compression direction to the opposed angle, hence clockwise, as seen in Figure 1.28. This figure also shows the results for the numerical reaction force obtained when the door is tilted 10° to the right. We can see that the tilting modifies the shape of the curve, which resembles that of the experimental mean. Additional studies show that the more the door is tilted, the more convex the curve gets. However, the values are not yet inside the interval delimited by the experimental tests.

This brings us to the third issue. From the influence analysis in Figure 1.30, we

can see that the friction coefficient can significantly vary the slope of the reaction force curve, when modified from 0.1 to 0.5. However, Figure 1.27 suggests that in the experimental tests, the difference between the lubricated and non-lubricated sections is small. This leads to the conclusion that the lubrication is not enough to simulate small friction, and thus, that the contact coefficient in the lubricated seal tests is close to the contact without lubrication. The friction coefficient in the numerical model must thus be modified. Figure 1.29 shows the resulting numerical vs experimental reaction force comparison, for different levels of door rotation. As we can see, with the new friction coefficient, the resulting reaction force falls in the interval of the experimental curves. Additionally, we observe that the shape of the mean experimental curve is more convex than that of the numerical model with a 5° door rotation, but less than that of the 10° rotation model. This analysis leads to the conclusion that there is a rotation taking place when the seal is compressed of between 5 to 10° in this specific seal geometry case.

Because the experimental tests have been done in a straight section of 290mm instead of in the whole seal profile, we don't know if the observed rotation would take place when the entire seal is mounted. Additionally, as we have explained earlier, in some parts of the door and especially near the hinge, the compression is diagonal instead of vertical, and the effect of this unequal compression on the rotation of the seal cannot be predicted. Hence, all this should be taken into account by introducing this possible rotation as a source of uncertainty in the optimization procedure. By doing so, and looking not only for an optimal point but for a robust one also, we assure that this rotation, existent or not, doesn't prevent the obtainment of a suitable solution.

With this in mind we can, and will, continue to use vertical compression for all remaining modeling.

1.4 Influence analysis

Seeing how this model is conceived with the goal of being used in an optimization procedure, a brief influence analysis is in order. Due to the fact that sound reduction is not the main function of car door and window seals, and that the modification of some parameters (such as material stiffness) is limited by the non-existence of their optimal alternatives (such as the nonexistence of rubbers with a specific Young's modulus that would be optimal), the influence of only three different parameters is analyzed. Because the window seal doesn't have an important static step (no large deformation compression), the three parameters intervene only in the door seal model.

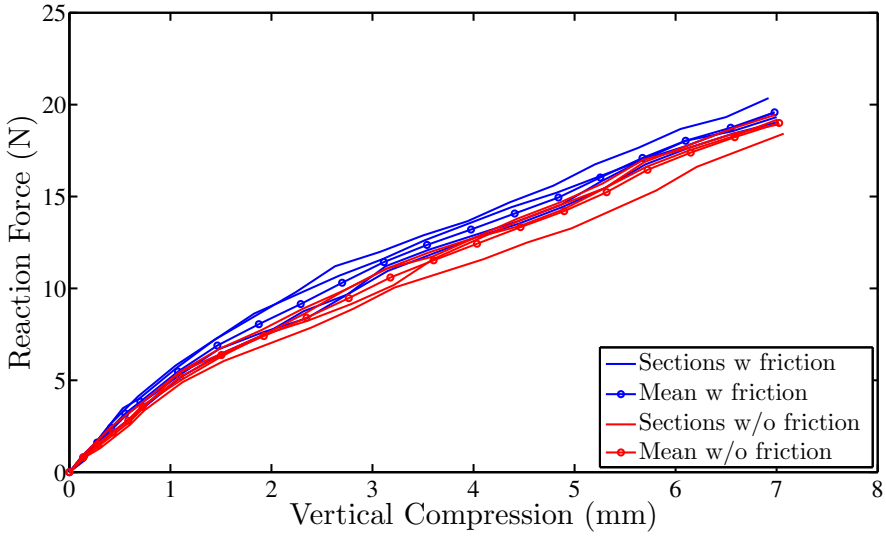

Figure 1.27: Comparison of experimental results for different seal sections with and without the use of lubricant

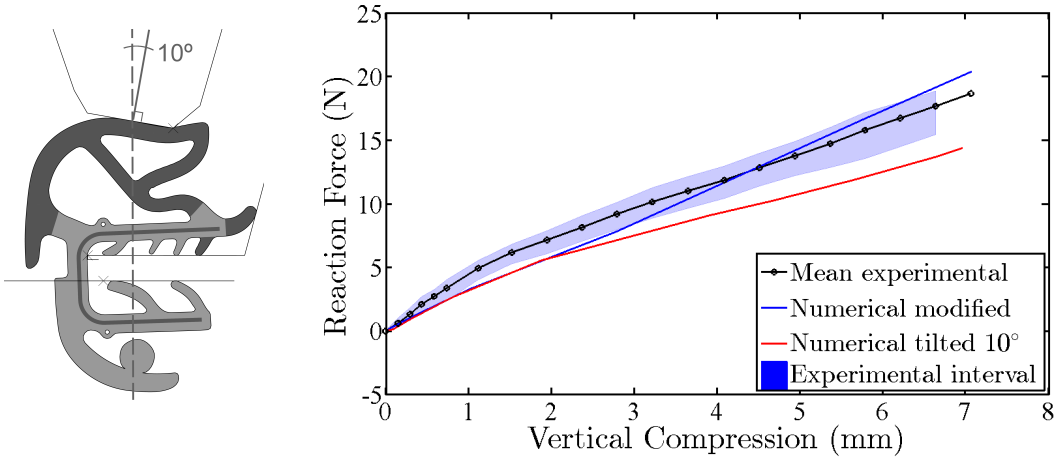

Figure 1.28: Results for reaction force when the door incident angle is tilted using the new seal geometry

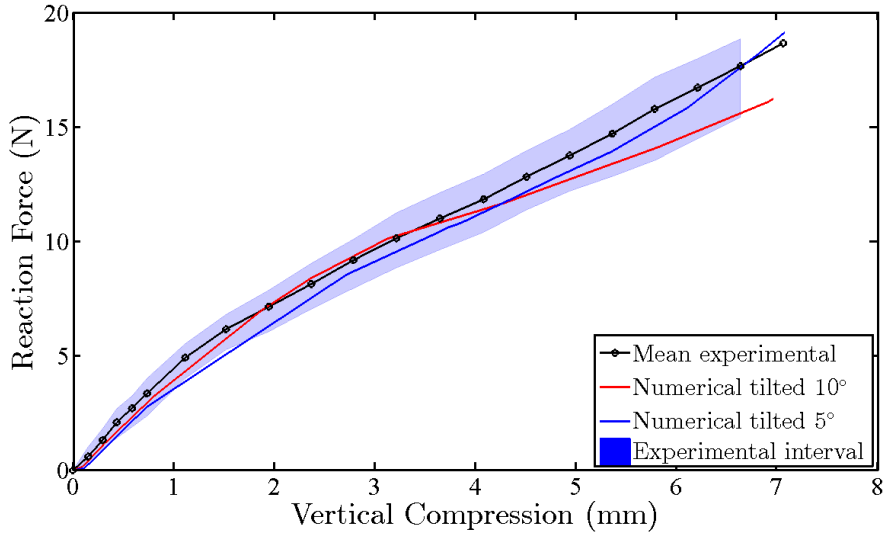

Figure 1.29: Comparison of experimental and numerical reaction force with a friction coefficient of 0.4 when the door incident angle is tilted

Contact

As we have explained in Section 1.2.1, the friction coefficient between metal and rubber is of about 0.5 with penalty contact. However, the roughness can be easily modified with a specific paint on the metal surface, or through machining. We have numerically studied the effect of different friction coefficients between the door and the seal on the reaction force in Figure 1.30. As we can see, the roughness of the contact can modify the slope of the curve, which means that the state of stress inside the seal section can be modified too.

Even though there is also contact in the window seal numerical model, and roughness could have a relevant effect on the static insertion of the window into the seal, it cannot be modified as easily as in door seals, since no paint can be applied and no machining is possible on the window.

Geometry

It is obvious that the initial geometry of the seal will have a great impact on its deformation throughout compression, and on its stress distribution. However, due to the mentioned alternative functions of the seal, and to the difficulty of a geometry optimization procedure, we cannot study the influence of the seal shape as a whole. Instead we have modified some areas one by one and looked at the resulting reaction force.

The choice of the areas to be modified comes from the realization explained in

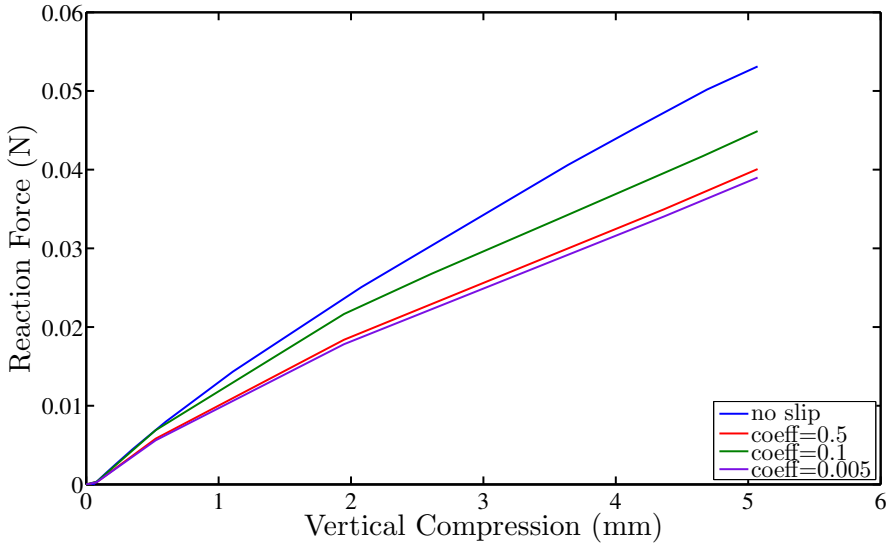

Figure 1.30: Comparison of numerical reaction force for different friction coefficients

the previous section, that the numerical geometry provided by PSA Group doesn't exactly match the physical one. Some zones that we consider could be influential are then modified one at a time to see the impact they have on the reaction force. Figure 1.31 shows these modifications and the resulting reaction force for each of them is depicted in Figure 1.32. Although the influence of each area seams small, we contemplate the possibility that the action of all the modifications as a whole can have a relevant effect on the final stress distribution. This hypothesis is corroborated in Figure 1.33, where we see that the difference between the reaction force of the initial numerical seal and that of the final modified one is relevant. We will therefore use this new geometry for the subsequent analysis.

Seal gap distance

We have pointed out all through this chapter that the seal gap distance will have a huge effect both in seal deformation and in stress distribution at the end of the compression step. This effect has been shown in Figure 1.11. However, due to the change of geometry explained in the previous paragraph, this analysis is no longer of value. Figure 1.34 shows the stress distributions at the end of compressions H2, H3, and H4 for the modified geometry.

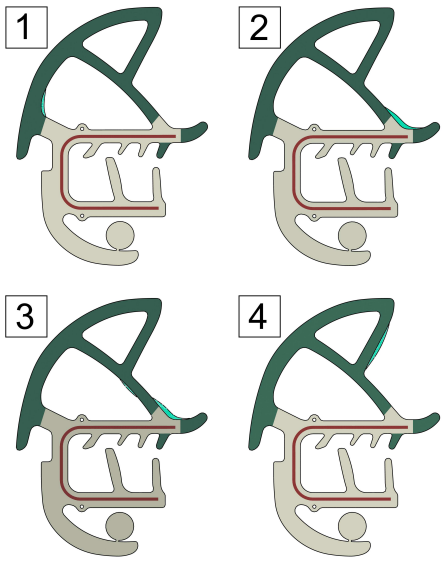

Figure 1.31: Geometry modifications tested for their influence on the final seal reaction force

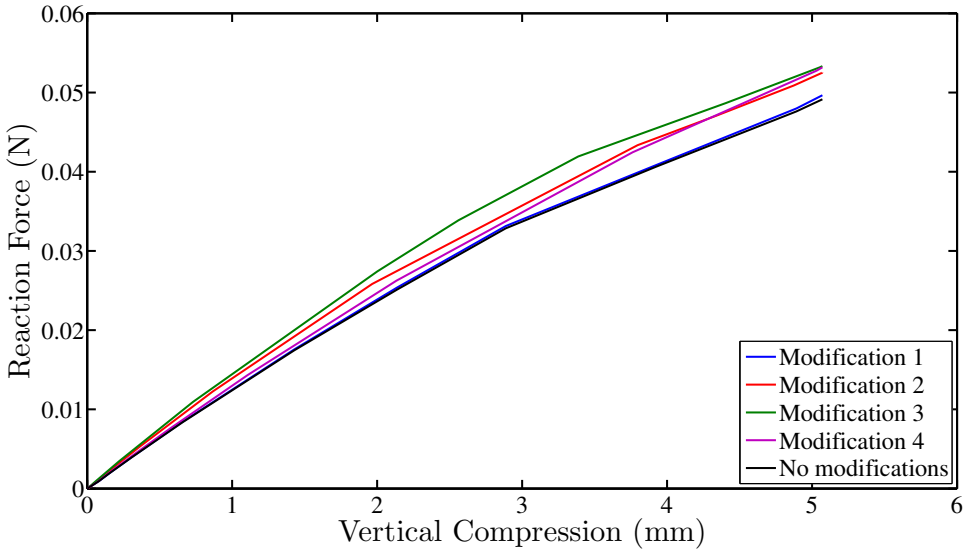

Figure 1.32: Reaction force for each modified seal

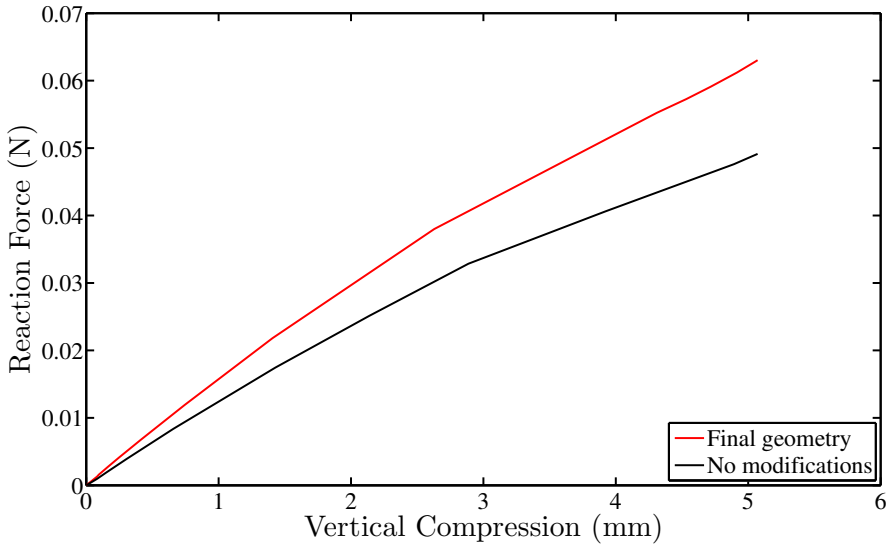

Figure 1.33: Comparison of reaction force between initial and final modified geometry

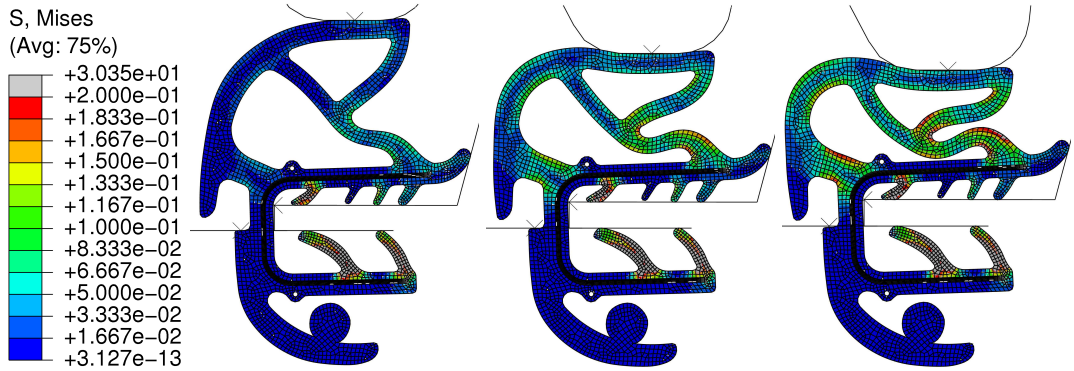

a) H3 compression b) H2 compression c) H4 compression

Figure 1.34: Numerical results of the door seal with modified geometry for each level of compression

1.5 Conclusions

In this chapter we have modeled the static behavior of the door and window seals using Finite Element software ABAQUS. Due to the incomplete information on the materials of the door seal, a preliminary material analysis of the compressible rubber was necessary before the modeling. A hyperelastic material model has been chosen among those available in ABAQUS, through the material evaluating tool in the software. From the provided experimental data, the coefficients of several models can be retrieved, as well as their strain-stress behavior. An analysis of these results has led us to consider the Neo-Hookean model as the most suitable for the case.

With all the material information, the modeling of all the phases undergone by both door and window seals is achieved. The details and workarounds are described in the chapter.

The modeling tools used for both seals are validated through a series of experimental tests on the door-seal. These allow comparing both the deformation and the reaction force of the seal, throughout compression of the resulting numerical model, to those of a physical section of the door seal. For this, two different experimental set-ups have been designed and built, which have lead us to the final conclusion that the numerical model is well suited for the description of the static behavior of the seal. However we have discovered that, due to fabrication unpredictability, a rotation unaccounted for in the numerical model can take place with the physical seals. As a consequence, this possibility needs to be considered in any subsequent optimization step as a source of uncertainty.

To conclude, and due to the fact that the model is conceived for an optimization procedure, an influence analysis is applied on 3 parameters of the door seal model (contact, geometry and seal gap distance), the three found relevant for the final deformation and/or stress state.

1.6 Expansions

The model resulting from this study is originally conceived for an optimization procedure. Here, the influence of only 3 possible optimization parameters is evaluated. For the future, we believe that it would be interesting to see a thorough analysis of the influence of the door seal geometry on its final state of deformation and stress after compression. Parameters such as the number of interior cavities, or the thickness of the seal's walls might have a relevant impact on its sound-blocking abilities. This analysis would, however, have to consider the other functions of the seal, such as its waterproofing capacity. Another possible extension of the work explained here revolves around the direction of the door compression. It has been explained that

the direction of the compression of the door seal changes depending on the distance to the door hinge. In this chapter, only vertical compression is considered, hence this expansion would increase the accuracy of the model.

The bulk of this chapter is centered on the door seal. In consequence, the accuracy of the window-seal model has been taken more lightly. Even though these seals are made of over 5 different elastomers, a single homogenized material, whose parameter values we have obtained from the bibliography, has been considered. The material properties of the seal affect, not only the transmission of sound through the seal itself, but also the response of the windows on which these seals act as boundary conditions. This is, thus, a main point of possible bettering of both window and window seal models.

1.7 Bibliography

[ACDM08] B. Andro, S. Chaigne, A. Diallo, and M. Mermet. Prediction of sound transmission through automotive door seal systems. In *Proceedings - European Conference on Noise Control*, pages 3819–3824, 2008.

[Bow09] A.-F. Bower. *Applied Mechanics of Solids*. CRC Press, October 2009.

[DB06] E. Dikmen and I. Basdogan. Experimental and numerical study for determining the mechanical properties of automobile weatherstrip seals. In *Proceedings of 8th Biennial ASME Conference on Engineering Systems Design and Analysis, ESDA2006*, 2006.

[DB08] E. Dikmen and I. Basdogan. Material characteristics of a vehicle door seal and its effect on vehicle vibrations. *Vehicle System Dynamics*, 46(11):975–990, November 2008.

[Gac07] H. Gacem. *Comportement visco-hyperélastique des élastomères: Viscoélasticté non linéaire, Application aux Multicouches [french]*. PhD thesis, Université Pierre & Marie Curie - Paris VI, 2007.

[Moo40] M. Mooney. A Theory of Large Elastic Deformation. *Journal of Applied Physics*, 11(9):582–592, September 1940.

[Riv48] R. S. Rivlin. Large Elastic Deformations of Isotropic Materials. IV. Further Developments of the General Theory. *Philosophical Transactions of the Royal Society of London A: Mathematical, Physical and Engineering Sciences*, 241(835):379–397, October 1948.

[Saa03] P. Saad. *Modélisation et identification du comportement non linéaire des cales en caoutchouc [french]*. PhD thesis, Ecole Centrale de Lyon, 2003.

[SMD04] A. Stenti, D. Moens, and W. Desmet. Dynamic modeling of car door weather seals: A first outline. In *Proceedings of the 2004 International Conference on Noise and Vibration Engineering, ISMA*, pages 1249–1261, 2004.

[SMSD06] A. Stenti, D. Moens, P. Sas, and Wim Desmet. Development of a numerical modelling methodology for the NVH behaviour of elastomeric line connections. In *Proceedings of the 2006 International Conference on Noise and Vibration Engineering*, 2006.

[SMSD08] A. Stenti, D. Moens, P. Sas, and W. Desmet. Low-frequency dynamic analysis of automotive door weather-strip seals. *Mechanical Systems and Signal Processing*, 22(5):1248–1260, 2008.

[WJZ12] Jin-Ting Wang, Feng Jin, and Chu-Han Zhang. Estimation error of the half-power bandwidth method in identifying damping for multi-DOF systems. *Soil Dynamics and Earthquake Engineering*, 39:138–142, August 2012.

[WMGK97] D.A. Wagner, K.N. Morman Jr., Y. Gur, and M.R. Koka. Nonlinear analysis of automotive door weatherstrip seals. *Finite Elements in Analysis and Design*, 28(1):33–50, 1997.

[YZ09] Y.-S. Yu and Y.-P. Zhao. Deformation of PDMS membrane and microcantilever by a water droplet: comparison between Mooney-Rivlin and linear elastic constitutive models. *Journal of Colloid and Interface Science*, 332(2):467–476, April 2009.

[ZZHW03] J.-C. Zhao, X.-S. Zhu, S.-J. Huang, and D. Wan. The Experimental Analysis for Compression Deformation of Automotive Door Seals. *Experimental Techniques*, 27(1):27–31, January 2003.

Chapter 2

Dynamic Acoustic Transmission Model

This chapter describes the methodology used in the Acoustic Transmission Model, which is to be coupled to the Static Model presented in the previous chapter. Due to the kind of excitation, this is all done in the frequency domain.

As explained in Section 1.2, some modeling issues have led us to separate the numerical analysis of the static and acoustic steps of the seals into two separate models. For the coupling of the two, the stress and deformation states at the end of the Static Model are input respectively as a predefined stress field and an initial geometry (orphan mesh) of the acoustic model.

The dynamic excitation introduces a new sort of material behavior and, as in the static case, the information available on this behavior is incomplete. For the compressible rubber the dissipative properties in this type of material must be taken into account, thus a viscoelastic material model is needed. In order to obtain the required information, some experimental tests are necessary.

Once all the materials have been characterized, the problem can be modeled using the acoustic tools in ABAQUS, which is the tool used by PSA Group. Only the transmission through the studied elements is taken into account in this chapter, leaving the propagation of the transmitted sound through the cavity for the flowing one. The suitability of ABAQUS modeling tools is validated, first through comparison with a benchmark case, and secondly by some experimental tests on the door seals. Once validated, the resulting acoustic modeling scheme is considered suitable for the transmission modeling of any element, and is thus applied to both door and window seals as well as the windows themselves. In this study, we consider the impact of each one of these elements separately, hence giving 3 different models. However, the coupling between the window seal model acting as boundary condition of window panes cannot be neglected. In consequence, the window seal model is used to characterize an equivalent simplified boundary on the window model.

2.1 Acoustic Theory

Before detailing the procedure through which the acoustic behavior of the seals have been modeled, some theoretical concepts must be introduced.

2.1.1 General Equations for acoustic-structural interaction

The acoustical problem analyzed in this chapter involves the transmission of sound through the seal into the air cavity inside the vehicle. The elastodynamic equations describing the dynamics on the rubber seal are commonly known, and the implementation of the specific viscoelastic material into these equations is explained below. However, the way the vibration is transmitted into the fluid media and how this energy is propagated through space is defined by a new set of equations ([MO92]). FE software ABAQUS allows several additional conditions at the surface of the acoustic medium, detailed for example in [Das14]. However in the following equations only the terms relevant to this specific study are kept.

For propagation in the fluid, the second law of Newton, on a volume of air where the particles are considered to have a constant velocity, leads to Euler's equation

$$\rho_f \frac{\partial^2 \mathbf{u}}{\partial^2 t} = -\nabla p \tag{2.1}$$

Where ρ_f is the fluid's density, $\mathbf{u}$ is the displacement and p is the pressure. Combining this equation with the mass conservation and the ideal gas laws ([Nun10]), we obtain the basic equation for wave propagation in air

$$\nabla^2 p - \frac{1}{c^2}\frac{\partial^2 p}{\partial t^2} = 0 \tag{2.2}$$

With c the speed of sound. In the frequency domain, equation 2.2 becomes the homogenous Helmholtz equation

$$\nabla^2 p + k^2 p = 0 \tag{2.3}$$

With $k = \omega/c$ the wave number. If we take the weak form of equation 2.3, using the test function δp over a volume V_f we get

$$\int_{V_f} \Big[\nabla^2 p \delta p + k^2 p \delta p\Big] dV = 0 \tag{2.4}$$

Green's theorem allows this to be written as

$$\int_{V_f} \Big[\nabla p \nabla \delta p - k^2 p \delta p\Big] dV + \int_S \mathbf{n}^- \nabla p \delta p dS = 0 \tag{2.5}$$

Where S is the boundary enclosing the acoustic volume V_f and $\mathbf{n}^-$ is the normal direction of surface S, interior to the fluid. Over this boundary, different conditions can be applied

- S_{fp} is the part of the boundary where the acoustic pressure is prescribed. It is on this surface that the acoustic waves are applied.

- S_{ft} is the boundary with prescribed normal derivatives of the acoustic medium. This will be the case for solid-structure interaction for rigid walls that don't vibrate.

- S_{fi} corresponds to the radiating acoustic boundary. In exterior problems, the acoustic media extends far enough from the source that they can be modeled as infinite in extent. In such cases the computational fluid region must be truncated, and a boundary condition applied to it to simulate waves passing exclusively in an outward direction.

- S_{fs} is the fluid-structure surface, where the motion of the air is coupled to the motion of a solid.

On S_{fp} the pressure is prescribed directly. By definition $\delta p = 0$, and so the surface integral in equation 2.5 disappears for this part of the boundary.

For the rest of the surface $S - S_{fp}$ the boundary conditions will be described in terms of $T(\mathbf{n}^-)$.

$$T(\mathbf{n}^-) = \nabla p \mathbf{n}^- \tag{2.6}$$

Where $\mathbf{u}^f$ is the displacement of the fluid. For S_{ft} the normal derivative is directly prescribed, thus $T_{ft}(\mathbf{n}^-) = T_0$. The only surface of this type that we will have is the case of rigid walls, where $T_0 = 0$ hence this term disappears.

On S_{fi} the Sommerfeld condition is applied.

$$\lim_{r\to\infty} \frac{\partial p}{\partial \mathbf{r}} - ikp = 0 \tag{2.7}$$

r representing the radius in spherical coordinates. This can be achieved in different ways, more details on the implementation of this surface condition are explained below. For the moment we will only reference to it as $T_{fi}(\mathbf{n}^-)$.

Finally, in S_{fs} where the fluid is in contact with a solid structure, equation 2.1 can be applied at the boundary.

$$\rho_f \mathbf{n}^- \frac{\partial^2 \mathbf{u^f}}{\partial t^2} = -\nabla p \mathbf{n}^- \tag{2.8}$$

On such a surface, the acoustic and structural media have the same displacement normal to the boundary, thus we can write

$$T_{fs}(\mathbf{n}^-) = \rho_f \omega^2 \mathbf{u^s} \mathbf{n}^- \tag{2.9}$$

Where $\mathbf{u^s}$ is the displacement of the solid boundary.

Introducing these definitions of the boundary into 2.5 and dividing by ρ_f we obtain

$$\frac{1}{\rho_f}\int_{V_f}\nabla p\nabla\delta p dV-\frac{k^2}{\rho_f}\int_{V_f}p\delta p dV+\int_{S_{fi}}\frac{1}{\rho_f}T_{fi}\delta p dS+\int_{S_{fs}}\omega^2\mathbf{u^s}\mathbf{n}^-\delta p dS=0 \quad (2.10)$$

The equation that describes the behavior of the solid media is defined by the virtual work equation

$$\int_{V_s}\delta\boldsymbol{\varepsilon}:\boldsymbol{\sigma}dV-\int_{V_s}\rho_s\omega^2\delta\mathbf{u^s}\mathbf{u^s}dV+\int_{S_{fs}}p\delta\mathbf{u^s}\mathbf{n}dS-\int_{S_t}\delta\mathbf{u^s}\mathbf{t}dS=0 \quad (2.11)$$

Where $\boldsymbol{\sigma}$ is the stress at a point in the structure, $\delta\boldsymbol{\varepsilon}$ the strain variation compatible with $\mathbf{u^s}$ and ρ_s the density of the solid material. $\mathbf{n}$ is the outward normal to the structure, which is the same as the inward normal to the fluid $\mathbf{n}^-$, and $\mathbf{t}$ is the surface traction applied to the structure.

Equations 2.10 and 2.11 define the variational problem for the coupled fields $\mathbf{u^s}$ and p. These can be discretized by introducing the interpolation functions

$$\begin{aligned}
p&=\boldsymbol{H^P p^P}, \quad P=1,2...\text{up to the number of pressure nodes}\\
\boldsymbol{u^s}&=\boldsymbol{N^M u^M}, \quad M=1,2...\text{up to the number of displacements dofs}\\
\delta p&=\boldsymbol{H^Q\delta p^Q}, \quad Q=1,2...\text{up to the number of pressure nodes}\\
\boldsymbol{\delta u^s}&=\boldsymbol{N^N\delta u^N}, \quad N=1,2...\text{up to the number of displacements dofs}
\end{aligned} \quad (2.12)$$

After discretization, the sum of these two equations becomes

$$\begin{aligned}
-\delta\mathbf{p^P}\{\omega^2[\mathbf{M_f^{PQ}}]-[\mathbf{K_f^{PQ}}]\}\mathbf{p^Q}-\boldsymbol{\delta p^Q}[\boldsymbol{P_{fi}^P}]+\boldsymbol{\delta p^P}\omega^2[\mathbf{S_{fs}^{PM}}]\mathbf{u^M}+\boldsymbol{\delta u^N}[\boldsymbol{I^N}]+\\
\boldsymbol{\delta u^N}\{-\omega^2[\mathbf{M^{MN}}]+\boldsymbol{\delta u^N}[\boldsymbol{S_{fs}^{QN}}]\boldsymbol{p^Q}-\boldsymbol{\delta u^N}[\boldsymbol{P^N}]=0
\end{aligned} \quad (2.13)$$

$$\begin{aligned}
[\mathbf{M_f^{PQ}}]&=\int_{V_f}\frac{1}{\rho_f c^2}\mathbf{H^P H^Q}dV\\
[\mathbf{K_f^{PQ}}]&=\int_{V_f}\frac{1}{\rho_f}\nabla\mathbf{H^P}\nabla\mathbf{H^Q}dV\\
[\mathbf{P_{fi}^P}]&=\int_{S_{fi}}\frac{1}{\rho_f}\mathbf{T_{fi}H^P}dS\\
[\mathbf{S_{fs}^{PM}}]&=\int_{S_{fs}}\mathbf{H^P}\mathbf{n}dS\\
[\mathbf{I^N}]&=\int_{V_s}\boldsymbol{\beta^N}\boldsymbol{\sigma}dV\\
[\mathbf{M^{NM}}]&=\int_{V_s}\rho_s\mathbf{N^N N^M}dV\\
[\mathbf{P^N}]&=\int_{S_{fs}}\mathbf{t}\mathbf{M^N}dS
\end{aligned} \quad (2.14)$$

With $\boldsymbol{\beta^N}$ the strain interpolation function that relates $\boldsymbol{\delta\varepsilon}=\boldsymbol{\beta^N\delta u^N}$.

2.1.2 Acoustic Transmission and Radiation

As we have stated previously, the model explained in this chapter is a transmission model, which seeks to describe the relationship between the incident sound and that inside the vehicle cavity. When a structure vibrates in a fluid medium, both elements can interact, and the vibrations of the structure propagate through the fluid, producing noise. Extended information on this phenomenon can be found in [Fah00].

As an example, let's imagine the thin, finite 2-dimensional bounded plate surrounded by air shown in Figure 2.1. If in the air on the left of the plate (referenced as 1 in said Figure) we consider the transverse movement of a wave of frequency ω, the dispersion relation leads to a wavenumber of $k_a = \omega/c$ with c the celerity of sound. Hence, a pressure wave in this medium would be described by

$$A(\mathbf{k_{a1}}, \mathbf{x}) = A_0 e^{i\mathbf{k_{a1}x}} \tag{2.15}$$

Whereas on the other side of the plate (referenced as 2) the equation characterizing a wave would give

$$B(\mathbf{k_{a2}}, \mathbf{x}) = B_0 e^{i\mathbf{k_{a2}x}} \tag{2.16}$$

Since we are working in a 2D case, $\mathbf{k_a} = (k_{ax}, k_{ay})$ and $\mathbf{x} = (x, y)$.

Analogously, the displacement of a transverse wave in the thin plate would be represented by

$$U(k_p, x) = U_0 e^{ik_p x} \tag{2.17}$$

Note that the plate is considered very thin, and so the y-propagating component of its wavenumber is not taken into account. k_p is in consequence not a vector but a scalar.

If we have an incident wave in fluid 1, with an incident angle θ, measured normal to the surface as seen in Figure 2.1, speed continuity implies that the speed normal to the contact surface between the air and the plate must be the same in both media for $y = 0$. Hence, equations 2.8, 2.15 and 2.17 give

$$\frac{\partial A}{\partial y}\Big|_{y=0} = A_0 i k_{ay1} e^{ik_{ax1}x} = \rho_f \omega^2 U_0 e^{ik_p x} = \rho_f \frac{\partial^2 U}{\partial t^2} \tag{2.18}$$

From which we deduce that $k_{ax1} = k_p$. As a consequence, the wave forces a vibration in the plate of the same wavenumber as k_{ax1}, which we will call the forced wavenumber k_{pf}. This vibration is transmitted to the fluid on the other side of the plate (fluid 2), in which a propagating wave of wavenumber appears, with $\mathbf{k_{ax2}} = \mathbf{k_{pf}} = \mathbf{k_{ax1}}$ and thus, since fluid 1 and fluid 2 have the same dispersion curve, $\mathbf{k_{ay2}} = \mathbf{k_{ay1}}$.

$$B_{forced} = B_{0forced} e^{i\mathbf{k_{a2}x}} \tag{2.19}$$

Additionally, the incidence of the forced vibrations on the plate's boundaries will create a new set of standing waves. These will be free bending waves, and their

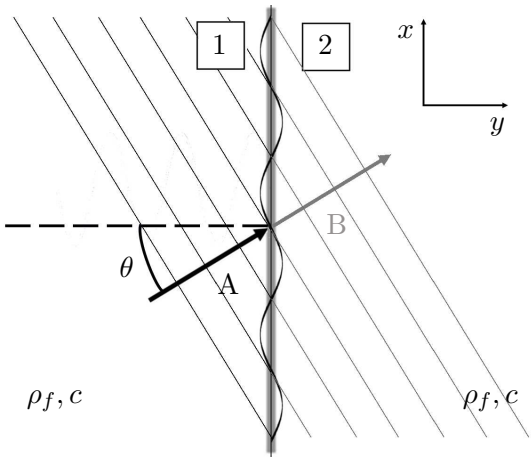

Figure 2.1: Acosutic-excited plate vibrating between 2 media

wavenumber will no longer be forced by the acoustic excitation (thus $k_{pf} \neq k_{ax1}$), but will instead follow the plate's dispersion curve

$$k_{pr}^2 = \omega\sqrt{\frac{\rho_p h}{D}} \tag{2.20}$$

With h the thickness of the plate, $D = Eh^3/12(1-\upsilon^2)$ the flexural rigidity and ρ_p the density. Again, from equation 2.18 we know that in fluid 2 this will create radiation waves with $k_{ax2} = k_{pr}$. Since the wavenumber in this fluid must still follow its dispersion curve $k_{a2} = \omega/c$, then

$$k_{ay2} = \sqrt{(k_{a2}^2 - k_{pr}^2)} \tag{2.21}$$

This relation introduces 3 sets of solutions

$$\begin{aligned} &k_{pr} > k_{a2}(\lambda_{pr} < \lambda_{a2}), \quad \omega < \omega_c \rightarrow \text{subsonic region} \\ &k_{pr} = k_{a2}(\lambda_{pr} = \lambda_{a2}), \quad \omega = \omega_c \rightarrow \text{critical region} \\ &k_{pr} < k_{a2}(\lambda_{pr} > \lambda_{a2}), \quad \omega > \omega_c \rightarrow \text{supersonic region} \end{aligned} \tag{2.22}$$

Where λ is the wavelength of wavenumber k, and ω_c is called the critical frequency, at which $k_{pr} = k_{a2}$.

$$\omega_c = \sqrt{\frac{\rho_p h}{D}} c^2 \tag{2.23}$$

- $\omega < \omega_c$ Subsonic region: From equation 2.21 $k_{ay2} \in \mathbb{I}$, the resonant modes in the plate produce waves in the form

$$B_{free} = B_{0free} e^{-|k_{ay2}|y} e^{ik_{ax}x} \tag{2.24}$$

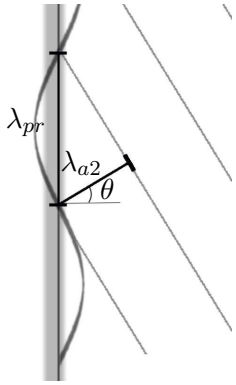

Figure 2.2: Coincidence phenomenon between two media

Which corresponds to a wave whose amplitude decreases with y. These are called evanescent waves and they don't propagate far away from the source. We say that the resonant modes radiate inefficiently. Note that they do slightly radiate due to the appearance of the wave's harmonics, some of which have wavenumbers k_{pr} smaller than k_{a2}, or to pseudo-coincidences ([NK03]). However, the largest part of the sound is coming from the forced waves, with wavenumber $k_{pf} = k_{ax} < k_{a2}$, the plate acting as an obstacle that resists to the imposed vibrations through an impedance. This is called non-resonant radiation. The wave in medium 2 is thus

$$B \approx B_{forced} \tag{2.25}$$

- $\omega > \omega_c$ Supersonic region: k_{ay2} is real, and thus the wave in fluid 2 propagates in both x and y directions

$$B_{free} = B_{0free} e^{ik_{ay2}y} e^{ik_{ax2}x} \tag{2.26}$$

The plate radiates effectively. Both forced waves and resonant modes can propagate through the air. However, the higher the frequency, the bigger the amount of vibrational energy in the plate transformed into heat, and the less generated noise. The angle of the radiated wave will depend on the relationship between k_{ay2} and k_{ax2}. This case can be observed in Figure 2.2.

The wave in medium 2 becomes

$$B = B_{forced} + B_{free} \tag{2.27}$$

- $\omega = \omega_c$ Critical region. $k_{ay2} = 0$. The resonant modes in the plate propagate through air parallel to the structure. As in the supersonic region, all the modes radiate, and thus both forced and free resonant vibrations are effectively transmitted into the receiving fluid.

$$B_{free} = B_{0free} e^{ik_{a2}x} \tag{2.28}$$

Giving

$$B = B_{forced} + B_{free} \tag{2.29}$$

The effective radiation of the free modes concerns the dispersion curves relating k_{a2} and k_{pr}. In the case of the forced waves, the plate is forced at $k_{ax1} = k_{a1} sin\theta$. The quotient between the incident wave A and the reflected forced wave B_{forced} depends highly on the relationship between k_{ax1} and k_{pr}, giving a maximal transmission when these two values are equal. This point is called the coincidence frequency ω_{co}, because there is spatial and frequency coincidence between the excitation and the plate. That is, the forced wavenumber corresponds to a natural wavenumber of the plate at its natural excitation frequency, and thus the plate vibrates almost freely, bounded only by its damping.

Since for a given $\mathbf{k_a}$ the value of $k_a x = k_a sin\theta$ depends on the incidence angle θ, so does ω_{co}. From the dispersion relation of the fluid $k_a = \omega/c$ and equation 2.20, the coincidence frequency is expressed as

$$\omega_{co} = \sqrt{\frac{\rho_p h}{D}} \frac{c^2}{sin^2\theta} \tag{2.30}$$

As we can observe, the lowest of these coincidence frequencies is for a grazing incident wave parallel to the plate, with $\theta = 90\,^\circ$, and is corresponds to the critical frequency in equation 2.23.

In summary, we find that the response of the bounded plate has 2 components. One where the plate is "forced" to travel at the wave speed imposed by the incident wave, and one where the waves caused by the forced incidence are reflected into the boundaries, producing free bending waves at a wavelength natural to the plate k_{pr}. The importance of each one of these components depends on the excitation frequency. When the excitation wavenumber coincides with the natural wavenumber of the plate, the latter vibrates strongly and there is an important peak in transmission. The position of this peak depends on the incidence angle of the incoming waves, and is minimal when they are parallel to the plate.

Acoustic intensity and Radiated Power

The expression for the acoustic intensity at a point in a fluid cavity is given by

$$I_a = \frac{1}{2\rho_f c} pp^* \tag{2.31}$$

Where p is the pressure at the said point.

Using equation 2.1, for a point in a fluid-structure interface, the radiated power deriving from this intensity for a vibrating structure is

$$W_{rad} = \frac{1}{2}\Re\left\{ \int_S p v_n^* dS \right\} \tag{2.32}$$

With p the pressure at the interface and v_n^* the complex conjugated value of the velocity of the same point normal to the surface.

Transmission Loss

The model built in this chapter is a transmission model, not a propagation one. That is, it attempts to model the capacity of the seal to transmit or block sound incoming from one side to the other, regardless of the shape and properties of the receiving side, in this case the interior of the cabin. As a consequence, the level of sound power alone, which is dependent on the absorbing properties of the room and the coordinates of the point where it is calculated, is not an appropriate criterion for the Transmission Model. A representative parameter of this "transmission capacity" is in order. The Transmission Loss (TL) is a good choice for this matter. It relates the total power incident on the excited side of the object (W_{inc}) to the total power transmitted to the other side (W_{trans}) through the following equation

$$TL = 20log\left(\frac{W_{inc}}{W_{trans}}\right) \tag{2.33}$$

Note that the higher the transmission loss curve, the less sound is transmitted. An example of a typical TL curve is depicted in Figure 2.3. As we can see, the coincidence phenomena can create significant dips in the blocking capacity of the seals and is in consequence relevant in any transmission study.

2.1.3 Sommerfeld condition with infinite elements

The Sommerfeld condition states that, when an object radiates in an unbounded domain, the waves scatter to infinity and, since there are no reflections at infinity, there can be no energy radiated back into the domain. If we consider a vibrating structure Ω^s delimited by a boundary Γ^N radiating sound in an unbounded domain Ω^e the problem can be expressed through the equations in 2.34.

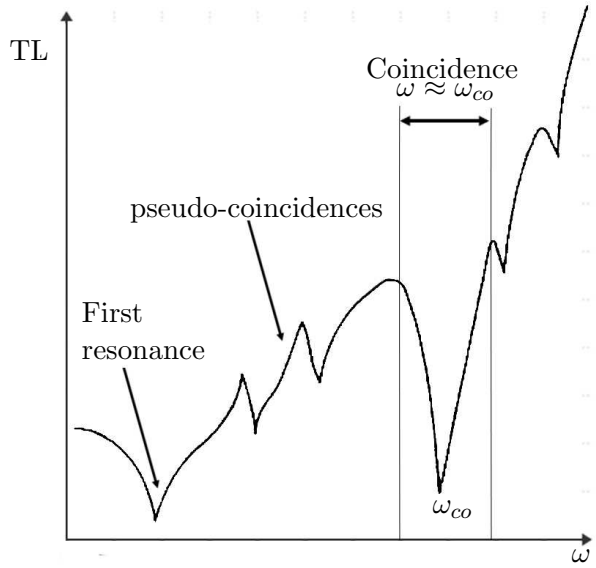

Figure 2.3: Typical TL curve for a finite plate

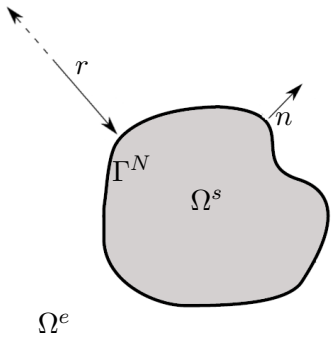

Helmholtz equation:

$$\nabla^2 p - K^2 p = 0 \quad \text{in} \quad \Omega^e$$

Neumann boundary conditions on the surface:

$$\frac{\partial p}{\partial n} \quad \text{in} \quad \Gamma^s$$

Sommerfeld's condition :

$$\frac{\partial p}{\partial r} - ikp = 0 \quad \text{when} \quad r \to \infty \tag{2.34}$$

Modeling this problem with FE would imply an infinite computational fluid in Ω^e, hence, infinite number of dof. To solve this, the unbounded domain must be truncated, and a condition equivalent to Sommerfeld's enforced at the artificial boundary Γ^{fi} (Figure 2.4). Several conditions can be applied on this boundary to satisfy the non-reflexion from infinity, such as fictitious absorbing layers (PML) or analytically calculated impedance (Dirichlet-to-Neumann operators). However, ABAQUS offers a precise solution to this problem with Infinite Elements. Using this method, the truncated domain can be smaller, thus reducing the number of dof and the time cost of the simulation. In this approach Ω^{ef} is meshed with Finite Elements, and the rest of the unbounded domain (Ω^e_e) is subdivided in radial infinite elements as seen in Figure 2.4, with shape functions capable of representing the waves from Γ^{fi} to infinity. A mapping transformation projects these elements into a standard finite

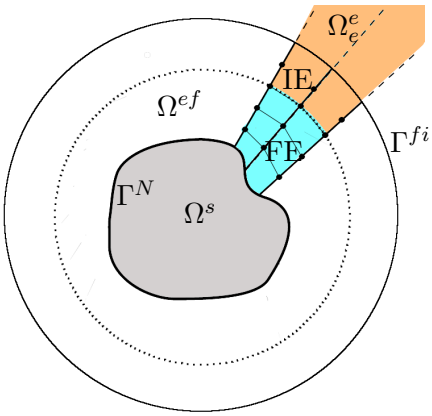

Figure 2.4: Implementation of IE in truncated infinite domain

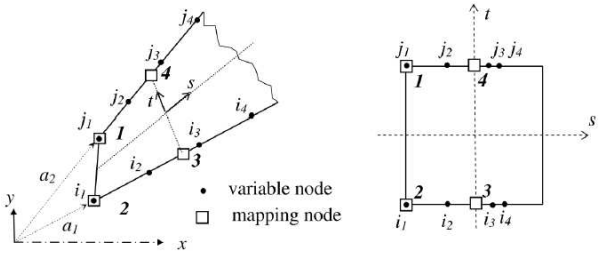

Figure 2.5: Infinite element mapping

parent space, as seen in Figure 2.5. For more information on this method, refer to [Ger00] [AM06] and [Das14].

2.1.4 The diffuse field

A diffuse field (or reverberant field) is one where the reflected sound dominates, resulting in the same Sound Pressure Level at all points. In this kind of fields, sound is completely random in phase, and appears to have no single source. The simulation of an aerodynamic excitation for experimental tests is complex and costly. In consequence, the validation of the numerical models is done by simulating the dynamic Transmission Models using a diffuse field excitation instead, and then comparing the results to those of an equivalent experimental procedure with the same kind of excitation, which can be easily created by using a reverberant room.

Numerically simulating a diffuse field excitation can be done by modeling a reverberant room and placing the object to be excited on one of the walls. However, this leads to somewhat heavy simulations with the chosen software (ABAQUS), since it needs the entire cavity to be meshed. Instead, from [Mös09] we know that an excitation of this kind is equivalent to the field created by uncorrelated sound-waves impinging uniformly from all directions of a half space, as depicted in Figure 2.6. If we consider only one of these waves, impinging into a structure at a certain angle θ measured normal to the surface of said element, the power flow onto this surface is related to the frequency-average value of the pressure in the half space of sources ($\tilde{p}$) by

$$W_{inc}(\theta) = \int_S \frac{\tilde{p}^2}{2\rho_f c} cos\theta dS \tag{2.35}$$

Considering all the possible values of θ in the half space, for a diffuse field $cos\theta$ ranges

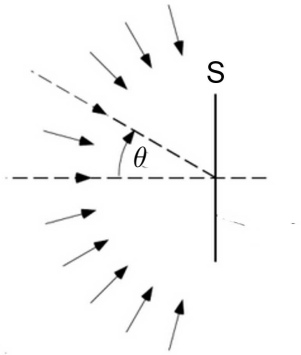

Figure 2.6: Waves impinging from different directions create a diffuse field

from 0 to 1, and equation 2.35 becomes

$$W_{inc} = S\frac{\tilde{p}^2}{4\rho_f c} \tag{2.36}$$

2.2 Materials

In Chapter 1, we characterized the rubber seal through a hyperelastic material, which can become non-linear for large strains, and we compressed it to a deformed state that we call pre-deformed or pre-stressed. The Cauchy Stress tensor resulting from this compression is noted $\boldsymbol{\sigma}|_0$. In the next step, this pre-deformed state is subjected to a linear perturbation arising from the acoustical field, which adds an oscillating factor $\Delta\boldsymbol{\sigma}$ to the total Cauchy Stress tensor ([Das14]).

$$\boldsymbol{\sigma} = \boldsymbol{\sigma}|_0 + \Delta\boldsymbol{\sigma} \tag{2.37}$$

We consider this perturbation to be small enough so that the hyperelastic behavior of the material model can be linearized around the pre-deformed state. With the dynamic perturbation, a viscoelastic frequency-dependent component appears, which needs to be introduced into the material model. As a consequence $\Delta\boldsymbol{\sigma}$ will have both an elastic factor $\Delta\boldsymbol{\sigma}^e$ and a viscoelastic participation $\Delta\boldsymbol{\sigma}^v$.

$$\Delta\boldsymbol{\sigma} = \Delta\boldsymbol{\sigma}^e + \Delta\boldsymbol{\sigma}^v \tag{2.38}$$

We can see in table 0.1 that the information that we have on the dynamic behavior of the materials in the seal previous to this study is incomplete.

For the window seal, the dissipative effects are represented by a simple structural damping obtained through the averaging of values in Thermoplastic Elastomer (TPE) window seals of the bibliography, thus no viscoelasticity parameters are needed. This

is not the case for the rubber in the door seal, that we have considered viscoelastic and that we will in consequence have to characterize. Part of this dynamic characterization we have already obtained from the providers (Hutchinson), in the form of experimental shear data on the incompressible Ethylene Propylene Diene Monomer (EPDM), listed in Appendix A). For the compressible EPDM however no data is provided, and some experimental tests of our own are necessary.

2.2.1 Viscoelasticity

Viscoelasticity is a property that describes materials that exhibit both viscous and elastic behavior when they undergo deformation. As a consequence of viscosity, these materials exhibit time-dependent strain when stress is applied and vice-versa. For the application of linear viscoelasticity to our material model, we will assume that the deviatoric and volumetric behaviors are independent. Hence, taking equation 1.25 we define the viscoelastic participation in the temporal domain

$$\begin{aligned} \Delta\mathbf{S}^v(t) &= \int_0^t 2G_R(t-t')\Delta\dot{\mathbf{e}}(t')dt' \\ \Delta p^v(t) &= \int_0^t K_R(t-t')\Delta\dot{\varepsilon}^{vol}(t')dt' \end{aligned} \tag{2.39}$$

Where G_R and K_R are respectively the time-dependent shear and bulk relaxation moduli, $\Delta\mathbf{e}$ is the additional deviatoric part of the strain tensor E after the pre-deformation, and $\Delta\varepsilon^{vol}$ is the additional volume strain also after pre-deformation, with $\varepsilon^{vol} = tr(\varepsilon)$.

Using the Fourier Transform we can translate these into the frequency domain

$$\begin{aligned} \Delta S^{v*} &= 2G_R^*\omega i\Delta\mathbf{e}^* \\ \Delta p^{v*} &= K_R^*\omega i\Delta\varepsilon^{vol*} \end{aligned} \tag{2.40}$$

More detailed information on viscoelasticity and its application in FE software ABAQUS can be found in [Das14].

2.2.2 Coupling of viscoelasticity with hyperelasticity

As we have explained at the beginning of this section, viscoelastic models take into account the frequency-dependent component of the material behavior. The non-frequency-dependent constituent is, however, represented by the same elastic law that describes the material when it undergoes a static effort.

When a dynamic excitation (small perturbation) is applied to an already pre-stressed material, whose long-term elastic response is non-linear, its elastic behavior can be linearized to a Hooke's law as in 1.30. However, because of the non-linearities, the shear and bulk moduli will depend on the state of pre-strain γ. The

linearized elasticity will then be represented by the long-term moduli $G_\infty = G_\infty(\gamma)$ and $K_\infty = K_\infty(\gamma)$. These quantities are automatically calculated by the software from the tangent elasticity matrix.

In an equivalent manner, the frequency-dependent component of the material behavior (viscoelasticity) is also conditioned by the level of pre-strain. To simplify, however, we will assume that the frequency behavior is independent from the magnitude of the pre-stress. In consequence, the complex viscoelastic shear and bulk moduli G_R^* and K_R^* described in 2.40 become

$$\begin{aligned} G_R^* &= G_\infty g^* \\ K_R^* &= K_\infty k^* \end{aligned} \tag{2.41}$$

Where g^* and k^* are respectively the non-dimensional complex shear and bulk relaxation functions.

Considering both frequency dependent and non-dependent material behavior, and from equations 1.30, 2.38, 2.40 and 2.41

$$\begin{aligned} \Delta\mathbf{S} &= 2G_\infty \Delta\mathbf{e} + 2G_\infty g^* \Delta\mathbf{e} \\ \Delta p &= K_\infty \Delta\varepsilon^{vol} + K_\infty h^* \Delta\varepsilon^{vol} \end{aligned} \tag{2.42}$$

From this equation we can define the total shear and bulk complex moduli G^* and K^* as

$$\begin{aligned} G^* &= G_\infty(1 + \omega g^*) \\ K^* &= K_\infty(1 + \omega k^*) \end{aligned} \tag{2.43}$$

The real and the elastic part of these complex values are called respectively the storage and loss moduli

$$\begin{aligned} G^* &= G_s(\omega) + G_l(\omega)i, \quad G_s = G_\infty(1 - \omega\Im\{g^*\}), \quad G_l = G_\infty\omega\Re\{g^*\} \\ K^* &= K_s(\omega) + K_l(\omega)i, \quad K_s = K_\infty(1 - \omega\Im\{k^*\}), \quad K_l = K_\infty\omega\Re\{k^*\} \end{aligned} \tag{2.44}$$

Additionally, the phase lag of the stress response δ is defined as:

$$\delta = tan^{-1}\left(\frac{G_l}{G_s}\right) \tag{2.45}$$

2.2.3 Models of linear viscoelasticity

Equations 2.42 to 2.44 relate the strain applied to a viscoelastic material to the resulting stress, using a Shear and a Bulk complex moduli. However the values of G^* and K^* remain unknown. In FE software ABAQUS, these frequency-dependent moduli can be defined in one of three ways: by a power law, tabular input, or Prony series expression.

Power-Law formula

Power-Law formula is the result of an expression used to fit experimental data from creep tests. Reformulated to describe relaxation functions in the frequency domain it gives

$$g* = g_1^* \frac{\omega}{2\pi}^{-a} \quad and \quad k* = k_1^* \frac{\omega}{2\pi}^{-b} \tag{2.46}$$

Where a and b are constants and g_1^* and k_1^* are complex constants.

Tabular input

The frequency domain response can alternatively be defined by giving the real and imaginary parts of ωg^* and ωk^*. Given the values of the storage and loss moduli these are

$$\begin{aligned} \omega\Re\{g^*\}) &= \frac{G_l}{G_\infty} \quad \omega\Im\{g^*\} = 1 - \frac{G_s}{G_\infty} \\ \omega\Re\{k^*\} &= \frac{K_l}{K_\infty} \quad \omega\Im\{k^*\} = 1 - \frac{K_s}{K_\infty} \end{aligned} \tag{2.47}$$

With G_∞ being the long-term modulus in the slice of experimentally tested material throughout the characterization test.

Prony Series Parameters

As we have explained above, viscoelastic materials present elastic and viscous behaviors, which are analogous respectively to springs and dashpots in a mechanical model. Various viscoelastic models attempt to find the linear combination of several of these elements that best represent the material's response under different loading conditions, each model differing from the others on the way these elements are arranged.

For the elastic components, modeled as springs of elastic constant E the formula that relates stress to strain is

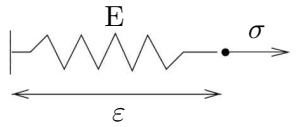

$$\sigma = E\varepsilon$$

The viscous elements represented by dashpots have the stress-strain relationship

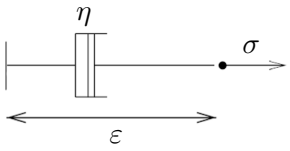

$$\sigma = \eta\dot{\varepsilon}$$

The Maxwell model seeks to represent viscoelastic behavior as a simple spring-dashpot system connected in series, as shown in Figure 2.7.

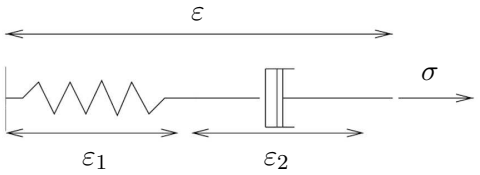

$$\sigma(t) = E\varepsilon_1(t)$$
$$\sigma(t) = \eta\dot{\varepsilon}_2(t)$$
$$\varepsilon(t) = \varepsilon_1(t) + \varepsilon_2(t)$$

Figure 2.7: Maxwell model

And so, the total associated complex relaxation function $E^*(\omega)$ is

$$\frac{\sigma(\omega)}{\varepsilon(\omega)} = E^*(\omega) = \frac{i\omega E}{\frac{1}{\tau} + i\omega} \tag{2.48}$$

Where $\tau = \frac{\eta}{E}$ is the relaxation time, which determines the time it takes for stress to relax in the viscoelastic material when a static strain is applied; the higher the value the longer it takes.

The Standard linear solid model or Zener model, combines the Maxwell element with a spring in parallel, assuring elasticity when $\omega = 0$

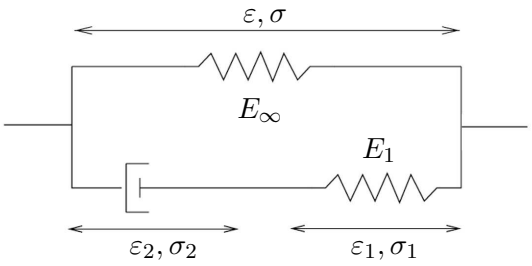

$$\sigma(\omega) = \sigma_1(\omega) + \sigma_2(\omega)$$
$$\sigma_1(\omega) = E_\infty\varepsilon(\omega)$$
$$\sigma_2(\omega) = E_1\varepsilon_1 = \eta\omega i\varepsilon_2$$

Figure 2.8: Standard Linear Solid model

The relaxation function $E^*(\omega)$becomes then

$$E^*(\omega) = \frac{\sigma}{\varepsilon} = E_\infty + \frac{E_1\omega i}{\frac{1}{\tau} + \omega i} \tag{2.49}$$

If we have N Maxwell branches in parallel with the spring, each one with its own E_i and η_i, equation 2.49 becomes

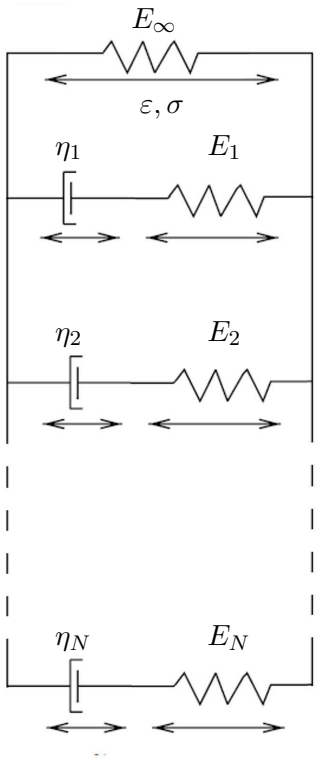

Figure 2.9: Generalized Maxwell model

$$E^*(\omega) = \frac{\sigma}{\varepsilon} = E_\infty + \sum_{j=1}^{N} \frac{E_j \omega i}{\frac{1}{\tau_j} + \omega i} \tag{2.50}$$

The term on the right of the equal sign in equation 2.50 is a Prony Series description of the relaxation function $E^*(\omega)$.

For the shear and bulk moduli complex relaxation functions in equation 2.43, respectively $G^*(\omega)$ and $K^*(\omega)$, expression 2.50 becomes

$$\begin{aligned} G^*(\omega) &= G_\infty + \sum_{j=1}^{N} \frac{G_j \omega i}{\frac{1}{\tau_j^g} + \omega i} \\ K^*(\omega) &= K_\infty + \sum_{j=1}^{N} \frac{K_j \omega i}{\frac{1}{\tau_j^k} + \omega i} \end{aligned} \tag{2.51}$$

ABAQUS, however, presents these equations in terms of the instant shear and bulk moduli, respectively G_0 and K_0

$$\begin{aligned} G_0 &= G_\infty + \sum_{j=1}^{N} G_j \\ K_0 &= K_\infty + \sum_{j=1}^{N} K_j \end{aligned} \tag{2.52}$$

So that equation 2.43 becomes

$$\begin{aligned} G^*(\omega) &= G_0\left(1 - \sum_{j=1}^{N} g_j^p\right) + G_0\left(\sum_{j=1}^{N} \frac{g_j^p \omega i}{\frac{1}{\tau_j^g} + \omega i}\right) \\ K^*(\omega) &= K_0\left(1 - \sum_{j=1}^{N} k_j^p\right) + K_0\left(\sum_{j=1}^{N} \frac{k_j^p \omega i}{\frac{1}{\tau_j^k} + \omega i}\right) \end{aligned} \tag{2.53}$$

With $g_j^p = G_j/G_0, k_j^p = K_j/K_0$.
In general, τ_j^g and τ_j^k do not have to be equal. However, FE software ABAQUS assumes that $\tau_j = \tau_j^g = \tau_j^k$. Since $G_\infty > 0$, we deduce from equation 2.53 that the sum of the Prony coefficients must be smaller than unity $\sum_{j=1}^{N} < 1$.

Multiplying and dividing the fraction on the right in equations 2.53 by the complex conjugate of the denominator we get

$$\begin{aligned} G_s &= G_0\left(1 - \sum_{j=1}^{N} g_j^p\right) + G_0\left(\sum_{j=1}^{N} \frac{g_j^p \omega^2 \tau_j^2}{1 + \tau_j^2 \omega^2}\right), \quad G_l = G_0\left(\sum_{j=1}^{N} \frac{g_j^p \omega \tau_j}{1 + \tau_j^2 \omega^2}\right) \\ K_s &= K_0\left(1 - \sum_{j=1}^{N} k_j^p\right) + K_0\left(\sum_{j=1}^{N} \frac{k_j^p \omega^2 \tau_j^2}{1 + \tau_j^2 \omega^2}\right), \quad K_l = K_0\left(\sum_{j=1}^{N} \frac{k_j^p \omega \tau_j}{1 + \tau_j^2 \omega^2}\right) \end{aligned} \tag{2.54}$$

In order to know the effect of the coefficients of each Maxwell branch on the Shear and Bulk moduli, we have plotted the values of the fraction in equation 2.53 depending on g_1^p and τ_1 (Figures 2.10 and 2.11).

We can see in the figures that for a Prony series, with only one Maxwell branch, the non-dimensional stiffness coefficient g_1^p has an influence only over the final magnitude of the modulus, whereas the time coefficient τ_1 governs the proportion of the modulus that is dissipative (imaginary) or non-dissipative (real). However, in all cases, for frequencies over a certain one (depending on the time coefficient), the modulus becomes constant and all non-dissipative.

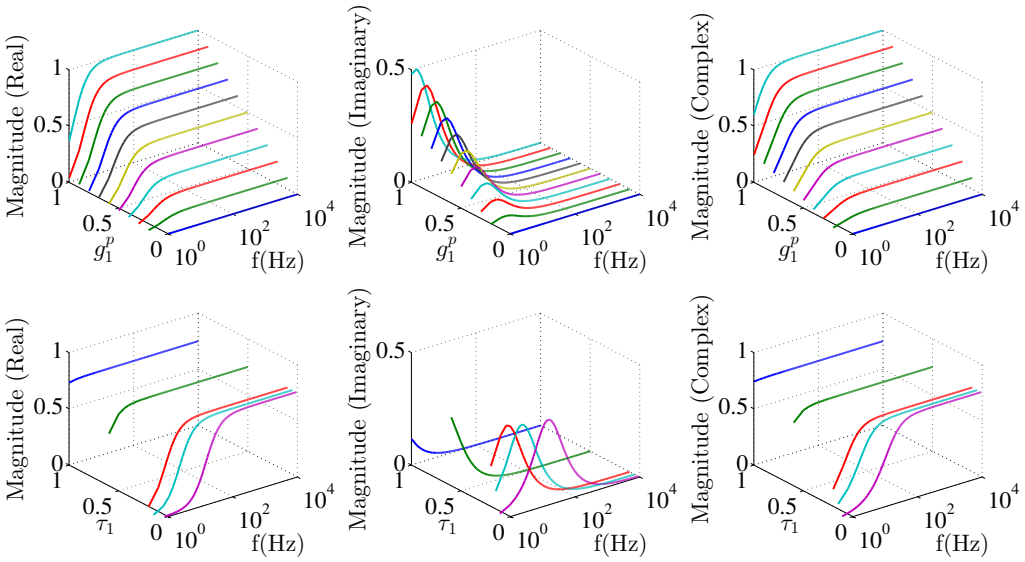

Figure 2.10: Influence of g_1^p and τ on G^*

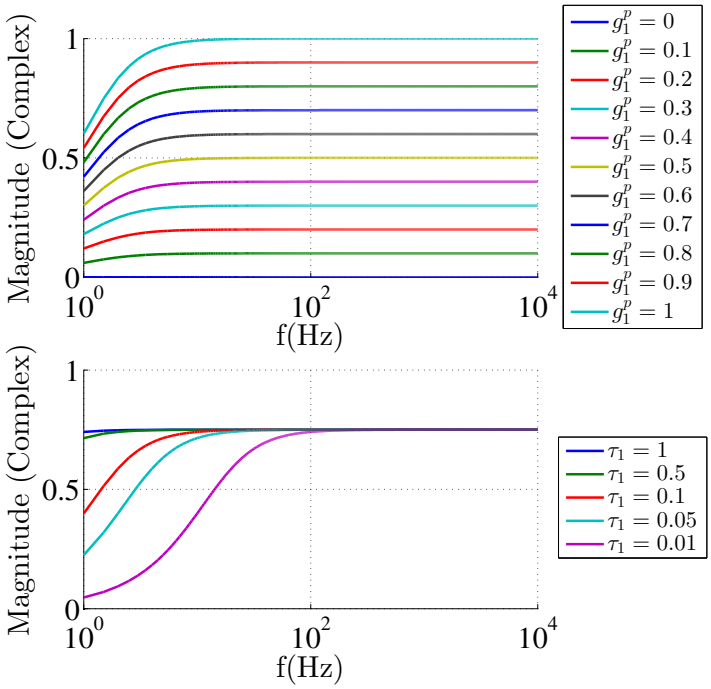

Figure 2.11: Detail of the influence on the magnitude of G^*

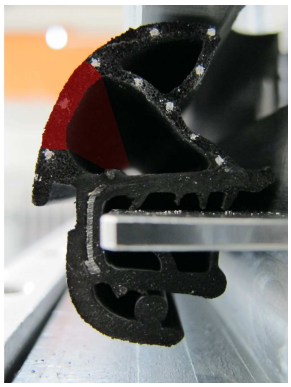

Figure 2.12: Cut and tested section of the seal

2.2.4 Experimental determination of viscoelastic coefficients

Due to the lack of information on the dynamic properties of the compressible rubber of the door seal, some experimental tests are needed. The results of these tests will be compared to a numerical model of the experiment, and the coefficients of the Prony Series explained above will be calibrated through the comparison.

The aim of these experiments is to excite a portion of rubber and compare the modal response of the material with the modes in a numerical model, by fitting the coefficients manually. Because rubber is flexible, gravity can easily deform it and so it cannot be excited directly. As a consequence, it needs to be put together with a stiffer material, such as aluminum, with known material properties. However, given that we are looking for both bulk and shear complex moduli, we need the experiment to involve both compressive and shear efforts. In order to do so, a section of the compressible EPDM in the upper part of the door seal (Figure 2.12) is placed in-between two simple thin aluminum beams (Figure 2.13). The touching surfaces are glued with a neoprene glue, which adheres well to the rubber. Although this kind of experiment would call for a much stiffer contact, the curvature of the rubber strip and the characteristics of this material make it difficult for any other glue to be used. However, we assume that since the surface to glue is small and the layer of adhesive is very thin, the contact will be stiff enough so that the viscosity of the glue doesn't interfere in the results. Since both aluminum beams can move independently, it is possible that they cause opposite tangential or normal efforts to the seal strip, thus, shear and compression.

The assembly is attached to a suspended shaker through an impedance head at its middle point (Figure 2.14). The impedance head has an accelerometer in its interior, from which we can output the magnitude of the vibrating force and the amplitude of the displacement. However, this sensor, as any other sensor, implies an additional mass on the beam that can interfere with its modal response. Additionally, its con-



Figure 2.13: Rubber and aluminum sandwich-like structure for the experimental determination of the viscoelastic parameters

tact with the upper aluminum beam stiffens the latter's middle section, which can also intervene in the observed modes. This information must be added to the numerical model so that the results are comparable to those of the experimental test.

The experimental tests are done considering 3 different sandwich assemblies, with 3 different beam lengths but same width and thickness. Since, with the accelerometer placed in the middle of the beam, we can only identify even modes, and all modes become more and more difficult to observe for high frequencies, only some 2 or 3 modes can be identified per assembly. Having 3 different assemblies gives us more points for the calibration of the Prony Series parameters. The final experimental setup is pictured in Figure 2.14 and the results of the tests are summarized in Table 2.1.

As we have explained above, the influence of the impedance head on the setup must be implemented in the numerical model. Since we cannot weight the accelerometer alone (because it is imbedded in the impedance head), we will obtain this information by testing only one aluminum beam without the rubber strip, the properties of which we know, and calibrating the values of an additional mass and a localized stiffness in the numerical model by comparison. This is done by adding a piece, with the same width as the impedance head, over the numerical beam (as seen in Figure 2.15) with a specific stiffness and mass. For simplicity, to account for the additional localized stiffness, we will consider that the piece is made of the same aluminum than the beams, with its density and stiffness, and an additional point mass will be calibrated manually to achieve the same modal behavior as the experimental tests on the beam. The results and details of this calibration can be found in Appendix B.

Once the values of the added mass and stiffness are known, we add the rubber strip and the inferior aluminum beam to the previous numerical model, as seen in Figure 2.16. The nodes in the contact surfaces are tied, and the glue in the experimental setup is not simulated directly. The purely elastic part of the rubber's material behavior is simulated with the hyperelastic model described in Chapter 1, and as it has already been said, the viscoelasticity is modeled through a Prony Series, the coefficients of which must be calibrated.

Given the simplicity of the experiments, it is difficult to calibrate more than one

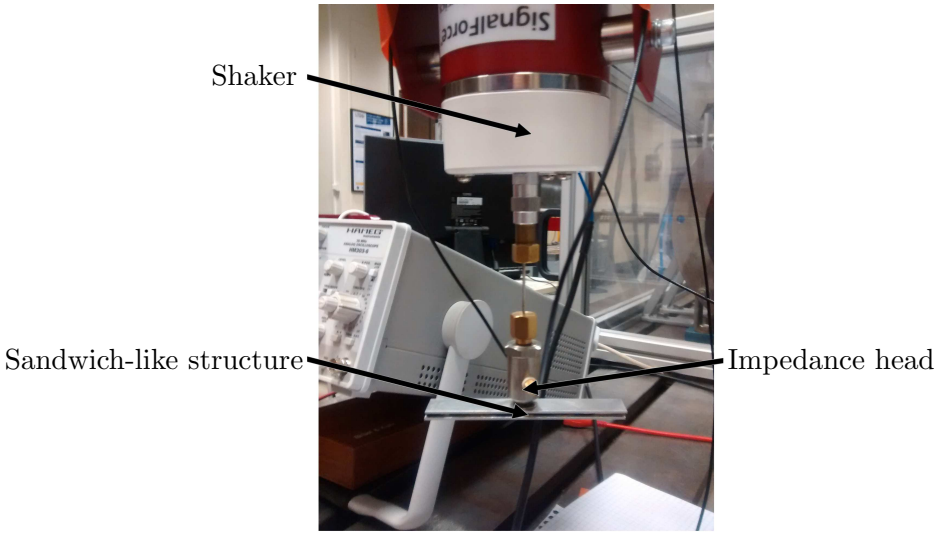

Figure 2.14: Experimental setup for the calibration of the Prony Series coefficients

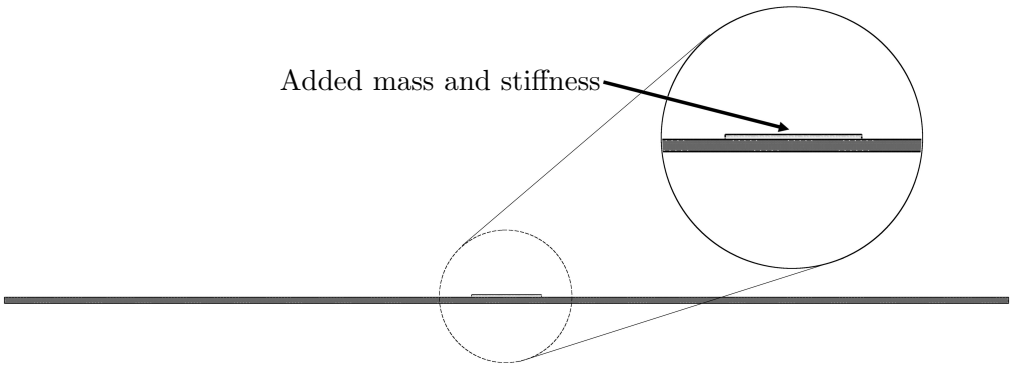

Figure 2.15: A small piece is simulated over the sandwich-like element to account for additional mass and rigidity of the experimental sensors



Figure 2.16: Final numerical model for the determination of the viscoelastic parameters

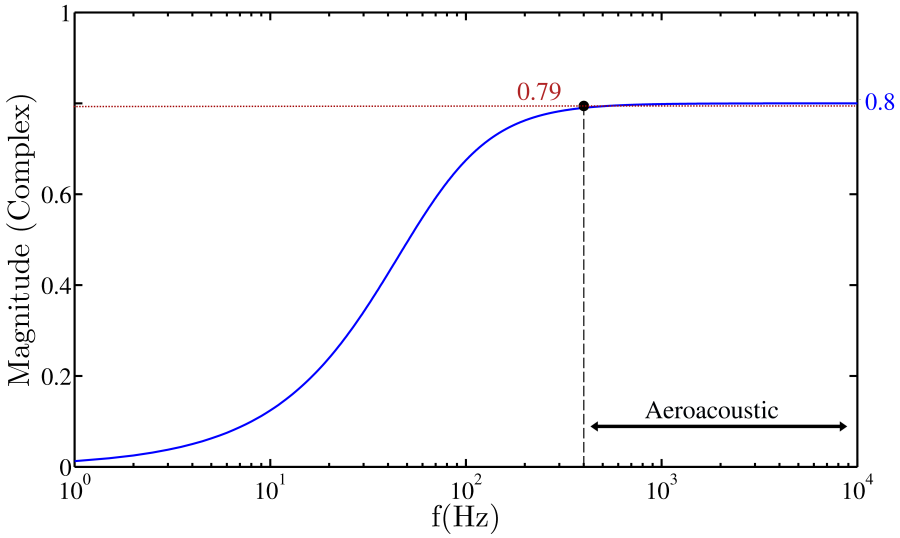

Figure 2.17: Magnitude of the moduli for $g_1^p/k_1^p = 0.8$ and$\tau_1 = 0.0025$. The value is considered constant for frequencies higher than $f_0 = 400Hz$, since from this value onwards the magnitude only varies from 0.79 to 0.8

Maxwell branch of the Prony Series model. In consequence, only one non-dimensional stiffness coefficient (g_1 and k_1) and one common relaxation time coefficient (τ_1) will be used for the determination of the Bulk and Shear moduli. Based on the parametric study in Figure 2.10, we know that for a given set of g_1, k_1 and τ_1, and for frequencies higher than a certain one (the value of this frequency depends on τ_1), the resulting moduli are constant. We can see in Figure 2.17 that for the viscoelasticity to be constant for frequencies on this study's range of interest (400-10000Hz), τ_1 must be over 0.0025s. Assuming the value of τ_1 is in fact bigger than this, the calibration to know the exact value is not of interest, since it will not have an effect on the moduli, that will remain constant over 400Hz. If we look into some bibliography ([Sch05] and [DB08]), the values of τ for EPDM blends and EPDM seals are at least over 1.85s. This is widely larger than 0.0025, and thus broadly sufficient to guarantee that the viscoelasticity in ABAQUS coincides with that of the seal. We thus take $\tau_1 = 1.85$.

A first numerical analysis shows that, compared to the Shear modulus, the Bulk modulus doesn't have an important impact on the modal behavior of the assemblies. Since the material properties are frequency-dependent, the modes have been identified in the numerical model by selecting the frequencies with maximal deformation in a frequency sweep. Given the moderate precision of the experiment, the small impact of the Bulk modulus becomes negligible, hence, since we know it to be only slightly compressive, we have chosen $k_1^p = 0.9$. With this information, only g_1^p is left to calibrate. This coefficient is manually modified, and the resulting modes compared to those obtained experimentally. The manual calibration leads to $g_1^p = 0.75$. With

the final coefficient set of $g_1^p = 0.75, k_1^P = 0.9, \tau_1 = 1.85$, Table 2.1 shows the comparison between the results from the experimental tests and those of the numerical model.

Table 2.2 summarizes the complete material information used for the dynamic step, including the Prony Series coefficients obtained from the above explained experimental procedure.

Deformation	Beam n°1 (L=100mm)		Beam n°2 (L=200mm)		Beam n°3 (L=300mm)	
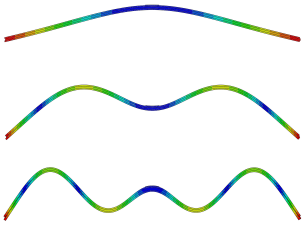	509 Hz	464Hz	138Hz	141Hz	79Hz	78Hz
	–	–	677Hz	654Hz	321Hz	319Hz
	–	–	–	–	820Hz	790Hz
Maximal error	$\approx 8,4\%$		$\approx 3\%$		$\approx 3,4\%$	

Table 2.1: Experimental(black) and Numerical(blue) modes correlation for different beam lengths and Prony series parameters $\mu_1 = 0.75, \lambda_1 = 0.9, \tau = 1.85$

Provided experimental material characterization for incompressible EPDM

Contrary to the compressible rubber, some information is provided previous to the study on the incompressible EPDM. This consists on the results of an experimental dynamic compression test, in the form of the magnitude of its Young's modulus E and its dissipation factor $tan(\delta)$. For an incompressible material, the relationship between these and the storage and loss moduli is

$$\begin{aligned} E_l/E_s &= tan(\delta) \\ G_s = E_s/3, \quad G_l &= E_l/3 \end{aligned} \tag{2.55}$$

	Incompressible EPDM	Compressible EPDM	Homogenized TPE	Steel
Dynamic behavior	Experimental tabular data	Prony coefficients: $g_1^p = 0.75$ $k_p^1 = 0.9$ $\tau_1 = 1.85s$	Structural damping $\eta = 5\%$	Structural damping $\eta < 1\%$

Table 2.2: Material information for dynamic analysis

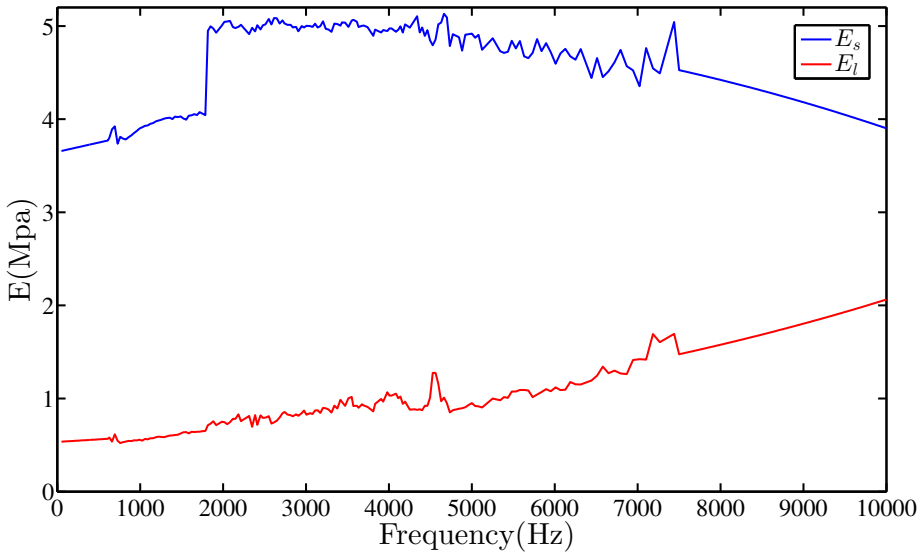

Figure 2.18: Final values of the dynamic complex modulus E^* of the EPDM on the door seal

Given the incompressibility of the material, $K_\infty \approx \infty$. The bulk coefficients in equation 2.47 are hence insignificant in comparison, and so they are ignored.

However, the information from these tests is insufficient since it is only given from 600 up to 7400 Hz. Considering the almost linear behavior of the data, the remaining frequencies (from 50-600Hz and from 7400-10000Hz) needed in Section 2.4 are extrapolated. Figure 2.18 shows the final values of E_l and E_s with said interpolations.

The experimental tests have been made around the uncompressed, undeformed state of the tested piece of material. In consequence, the hyperelastic law defined for this material in the previous chapter can be linearized around the unstressed state through equation 1.40. Through equation 2.55 this leads to the long-term modulus in equation 2.47 being equal to this linearized value $G_\infty = 2C_{10}$.

2.3 Implementation of the Finite Element acoustic model

The acoustic behavior of the seals is to be modeled with the acoustic tools in FE software ABAQUS. These are not commonly used, and given the complexity of the dynamic analysis we have decided to test them first on a simple model, for which there is a benchmark solution. By comparing our numerical model with the known solution, we are pre-validating the modeling tools for their subsequent application

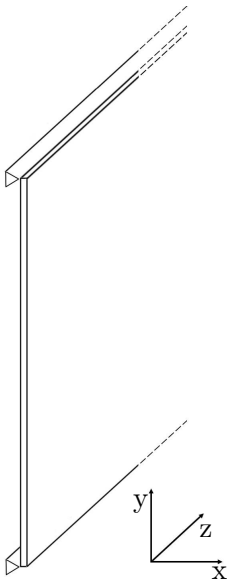

Figure 2.19: Benchmark case used for comparison

into the more complex seal models.

2.3.1 Simplified Transmission Model

The simplified Transmission Model, on which we test the acoustic modeling tools, reproduces the benchmark solution found in [PT12]. This example consists on a thin plate-strip, set in an infinitely rigid baffle with a width of 1m in one direction and infinite length in the other. The boundary conditions are assumed simply supported.

Since we seek to model the seals in a 2-D manner, the modeling tools should be tested in an also 2-dimensional model. Given that the plate is infinite in one direction, it can be modeled as a rectangular section with width and thickness in the 2-D plane, and infinite length in the z direction perpendicular to the 2-D model.

Both the solutions for a simple oblique wave excitation and a diffuse field are shown in the cited paper ([PT12]). This allows us to test our simplified model first for a very simple one-wave excitation and then, once this is validated, proceed to the application of a much more complex diffuse source.

To reproduce the benchmark case, the modeled plate is made of aluminum and is simply supported between two air regions. Its dimensions in the 2D x-y plane are of 1000mm in the y-direction and 6mm of thickness in the x-direction, as depicted in Figure 2.19.

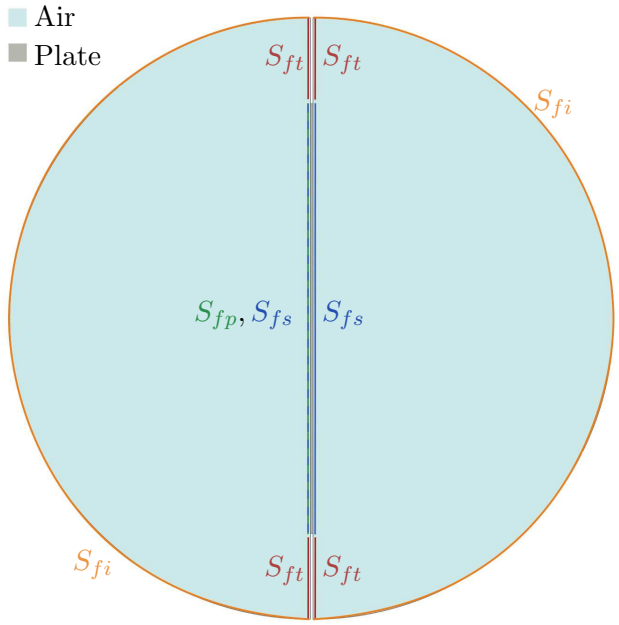

- Prescribed pressure from incident wave on S_{fp}
- Rigid wall conditions on S_{ft}
- Infinite elements on S_{fi} of 9^{nth} order
- Equal fluid-structure velocity S_{fs}

Figure 2.20: Simplified model of a plate vibrating between 2 media

For the construction of the 2-D simplified model, the geometry of the plate, as well as the air cavities surrounding it are introduced in ABAQUS. The latter are modeled as finite, with semicircular contours as shown in Figure 2.20. The material properties in given in the paper ([PT12]) are inputted, and the plate-air contact surfaces are tied together through imposing identical node velocities. Following the notation used in Section 2.1.1, Figure 2.20 displays the different surfaces of the model.

Following the rule explained in Section 1.2, the mesh size of the acoustic elements should not be bigger than 5.6 mm. Using the same methodology, the mesh in glass (speed of sound of 4540m/s) should be of a maximum size of 75mm. 9th-order infinite elements are used in S_{fi}. This is the highest order allowed by ABAQUS for this type of elements. Choosing the maximal value we ensure maximal accuracy for the Sommerfeld condition.

Since the incidence wave is known, and the excited surface is plane, we can calculate the power transmitted to the plate through

$$W_{inc} = S\frac{1}{2\rho_f c}p^2 cos\theta dS \tag{2.56}$$

Two types of acoustic excitations are applied to the model:

- Oblique incident wave (45°)
- Diffuse field

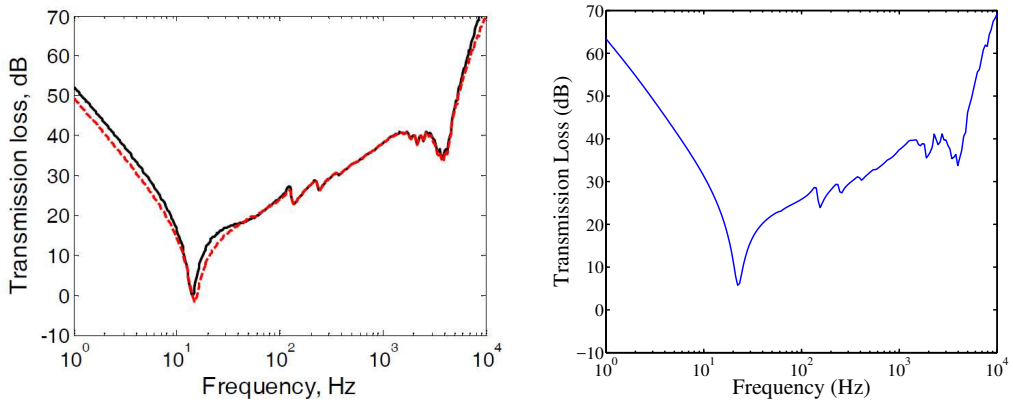

a)TL curve by I. Prasetiyo and D.J. Thompson

b)TL curve from simplified model

Figure 2.21: Transmission Loss for a single wave excitation incident at 45º

Since the incident wave is known, equations 2.35 and 2.36 can be used for the calculation of the incident power W_{inc} for both cases. The transmitted power is obtained through the pressure and velocity results outputted by ABAQUS in the right fluid-structure interface, using 2.32. The TL in 2.33 is then calculated and compared to that of the paper.

The comparison of the results of this model with those of the referred paper for the first wave is shown in Figure 2.21. As we can see, the figures are very much alike. The only difference we seem to find is that the TL from the simplified model seems to be shifted some 100Hz to the right with respect to the benchmark results, and has slightly higher values for low frequencies. We attribute this discrepancy to the difference of mass and stiffness between the modeled and benchmark plates, given that, in lack of the exact density and Young's modulus values of the latter, we have taken approximate values of these two properties for our simplified model.

ABAQUS offers a special tool for the creation of diffuse fields. This simulates the incidence of a user-specified number of uncorrelated incident waves with different incidence angles. However the result doesn't seem to match the benchmark solution. This could be because this tool is conceived for 3D diffuse field creation, and is not adapted for 2-dimensional applications. As a result, we have decided to simulate the diffuse field by our own means. For a diffuse field of N incident waves, we build a Matlab script that creates N ABAQUS input files, each with a different single oblique wave excitation, which we know to be accurately modeled thanks to the previously mentioned comparison in Figure 2.21. These scripts are all inputted in ABAQUS. The square-pressure results at the receiving side of the plate are averaged, and the mean power is determined. Finally, the TL is found using the equations above. The results are depicted in Figure 2.22.

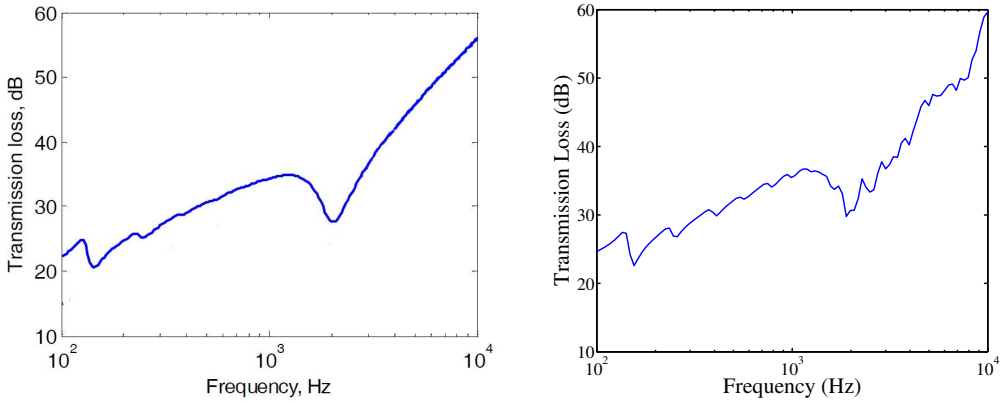

a)TL curve for diffuse field by I. Prasetiyo and D.J. Thompson

b)TL curve for diffuse field from simplified model.

Figure 2.22: Transmission Loss for a diffuse field excitation

We can observe in the figure that both curves have a very similar tendency. However, the results from the simplified model show some oscillations that do not appear in the image from the paper. To explain this we have to take into account the differences between the 2 models. The one in the paper generates a diffuse field using 9 incident angles about the z axis of Figure 2.19 and 18 in the y axis. Our simplified model is 2D, and thus we have 20 waves incident about the z axis, always in the x-y plane. This prevents the smoothing about the y plane that derives from a diffuse field, and some modes or pseudo-coincidences might appear.

All in all, the results from the comparison of the TL curves obtained with the simplified model and those found for the benchmark solution in the cited paper allow us to pre-validate the used tools.

2.3.2 Door Seal Transmission Model

Once the ABAQUS tools for acoustic modeling have been validated, they are ready to be applied to the seals.

For the door seal, the deformed mesh and stress state of the seal at the end of the static simulation are imported into a new model. Using this deformed geometry, the air cavities around the seal are modeled. These are:

- The inside cavities
- Exterior cavity
- Interior cavity

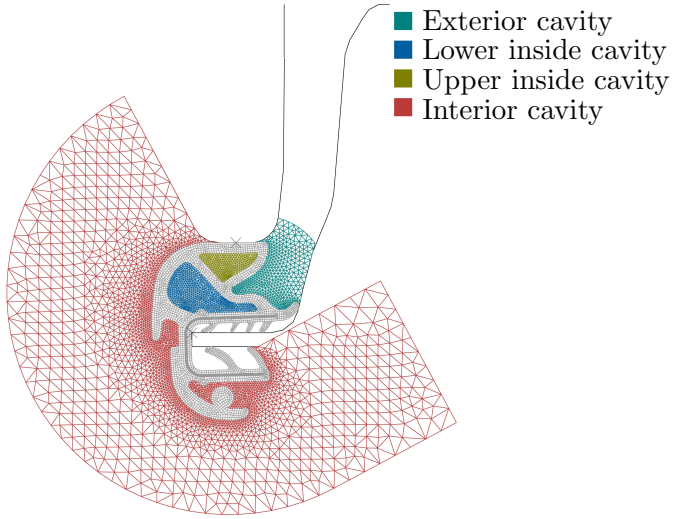

Figure 2.23: Door seal Transmission Loss model

The zones corresponding to each of these cavities are shown in Figure 2.23.
The exterior and interior cavities are both modeled with a semicircular geometry on their sides farther away from the seal, so that the infinite elements can be implemented. As in the simplified model, each of the zones mentioned in Section 2.3.1 and in Figure 2.20 can also be found in the Door Seal Transmission Model, and are illustrated in Figure 2.24.

Given that for the experimental validation the output is the pressure in the cavity, right next to the seal, instead of the pressure and velocity of the radiating surface of the seal itself, the radiated energy W_{rad} is calculated using equation 2.32, which transforms, through equation 2.1 into

$$W_{rad} = \frac{1}{2}\Re\left\{\int_{S_{out}} \frac{pp^*}{\rho_f c} dS\right\} \tag{2.57}$$

With p the pressure values in S_{out}, marked as a dashed black line in Figure 2.24.

The model's viscoelasticity has been characterized using the values in Table 2.2, through either tabular input or Prony series coefficients. The elasticity is determined by the static material behavior coefficients used for the model in the previous chapter (see Table 1.3).

As for the Simplified Transmission Model, the air is meshed with triangular elements, whereas the seal inherits the geometry of the previous static model and is hence built from quadrilateral elements (Figure 2.23).

As we have explained in the Introduction, TL curves are not really informative,

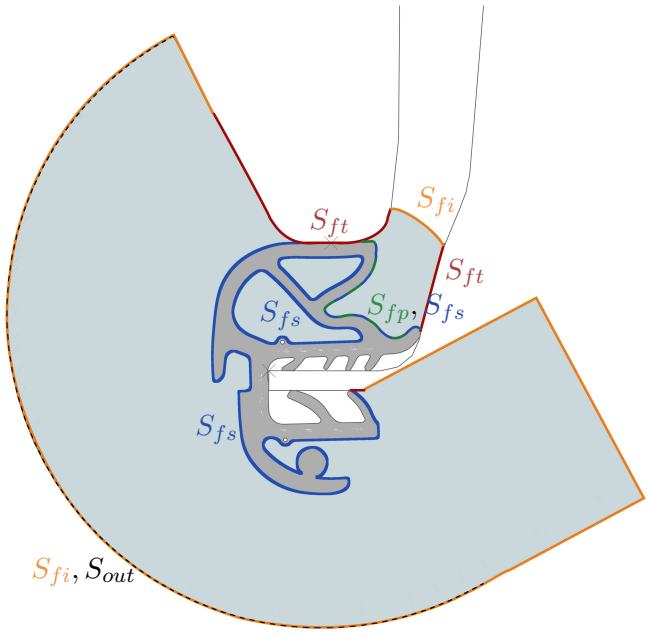

Figure 2.24: Boundary conditions on the door seal transmission model

since they only give information near the seal. A thorough analysis is thus not relevant and we will only briefly comment the TL curves in this section.

The resulting TL curve for an H1 pre-compressed seal excited by a diffuse field is depicted in Figure 2.25. To account for diffuse field convergence, we show the results for 20 and 40 incident waves. In general, we can see that there are a lot of seal modes or coincidences from mid to high frequencies. Also, for this combination of material parameters, we seem to observe a dip in the main trend of the curve around 1000-2000Hz.

2.3.3 Window Seal transmission model

The Window Seal Transmission Model is implemented in ABAQUS in the same way as the Door Seal model. The resulting mesh and stress state at the end of the Static Model described in Chapter 1 are imported into a new model, with the addition of the viscous parameters for TPE shown in Table 2.2. Figure 2.26 illustrates the inside, exterior, and interior semi-circular cavities modeled around this mesh for the acoustic excitation. The different zones, corresponding to the different boundary conditions mentioned in Section 2.3.1, are shown in Figure 2.27.

The resulting TL is shown in Figure 2.28. In this figure we observe fewer modes than in the door seal TL. We seem to observe a maximum sound transmission (mini-

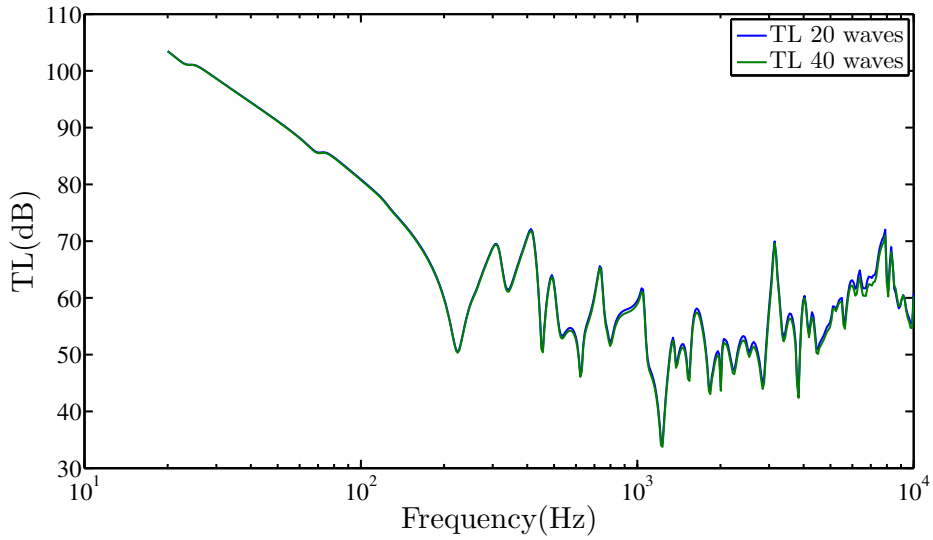

Figure 2.25: Door seal TL for 20-wave diffuse field

mum TL) around 1000Hz, more accentuated than in the other type of seal. Obviously this will depend on the material parameters used for the model, which, as explained in the Introduction have been greatly simplified.

Until now, only the mentioned window and door seals have been modeled. However, as already explained in the Introduction, the windows are another important path for sound transmission into the interior of the vehicle. Additionally, the window seals, which are placed around 3 of the 4 sides of the windows play an important role in the way the latter behave. Since plate-like structures such as windows have already been thoroughly studied, it is this boundary condition behavior of the window seals that is of interest to this research.

Window seal boundary conditions equivalent spring

The goal of our analysis is to obtain the dynamic stiffness of the seal when it is directly excited by an harmonic force perpendicular to the window F_{ext}(see Figure 2.29). This stiffness is frequency-dependent, and its effect on the window system can be reproduced by replacing the seal with a simpler element in ABAQUS, with the same dynamic stiffness. This replacement at the boundaries of the window model would substantially reduce its complexity and size, leading to a faster simulation.

Given that, to study the dynamic behavior of the window seal, the meshing of the air cavities is unimportant, there is no need to separate the Static Window Model from this vibrational study. In consequence, this analysis will be added to the Static Window Model described on the previous chapter, where the window is modeled as

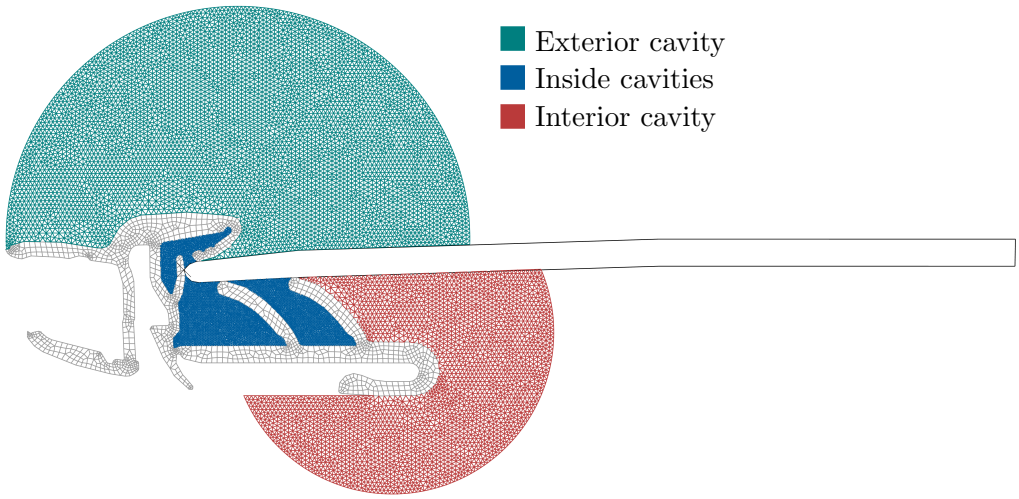

Figure 2.26: Window Seal Transmission Loss model

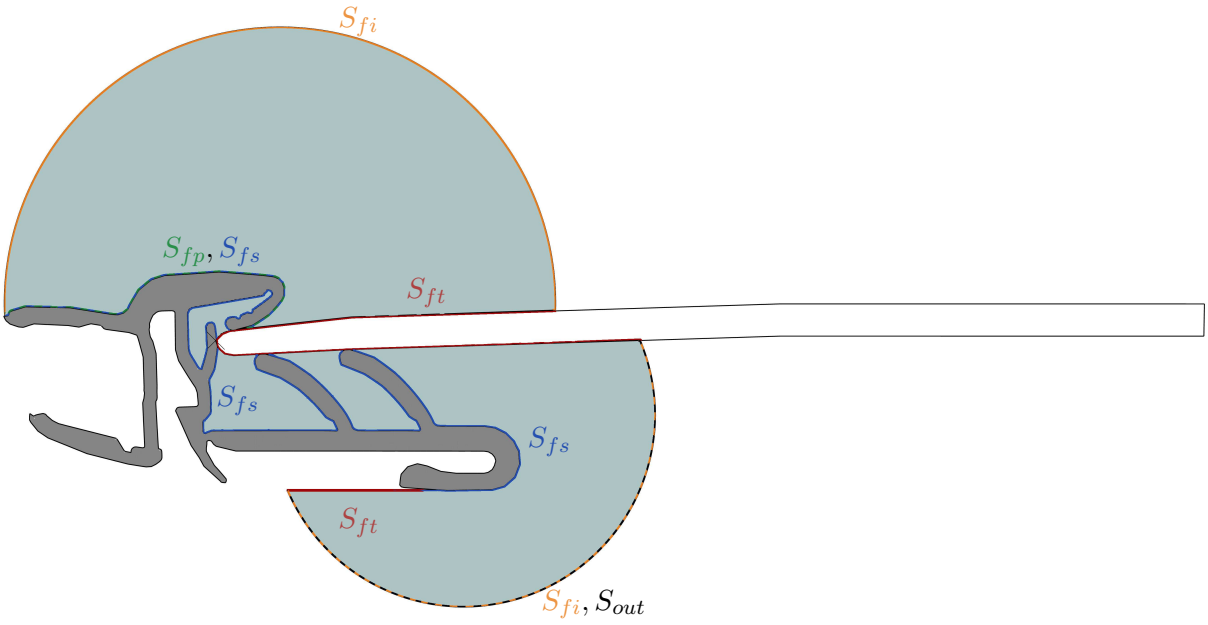

Figure 2.27: Boundary conditions on the Window Seal Transmission Model

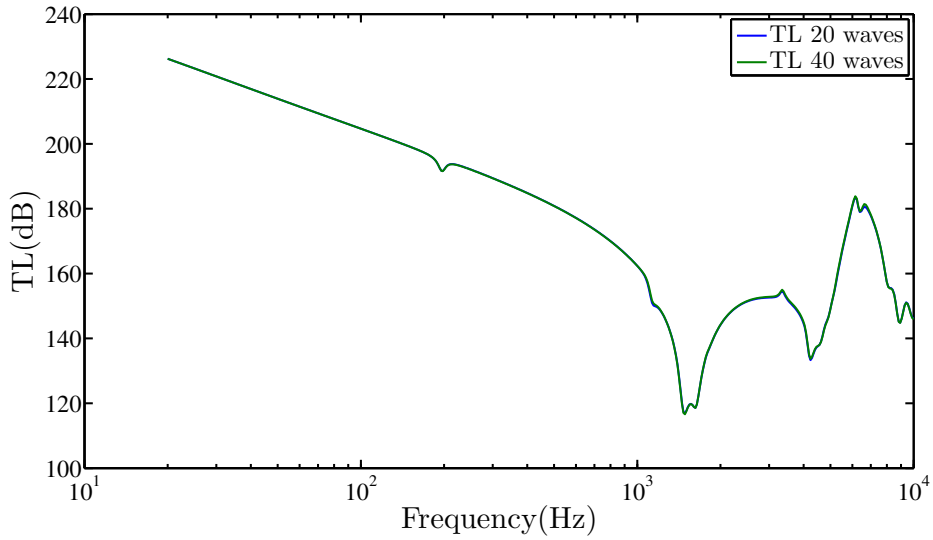

Figure 2.28: TL for the window seal

a rigid solid and has thus no deformation dof. Two fictitious phases are added to those already in the Static Model.

Boundary condition replacement: For the window insertion phase in Chapter 1, the vertical and rotational dof of the window are blocked, to mimic the subjection force that is applied to the window by the unknown surrounding elements, different from the seal (Figure 1.13). However, the harmonic excitation needs for the vertical dof to be released, to allow vertical displacement, whilst maintaining the effect of the forces applied by the mentioned surrounding elements. This issue is solved by replacing the vertical blocking of the window by an equivalent applied vertical load, that retains the window in place when no excitation is applied, but allows for vertical displacement (Y_{disp}) when a dynamic force is implemented. For the model to converge after this replacement, a static step, separate from the dynamic excitation, needs to be simulated.

Dynamic load and seal replacement: Once the vertical displacement of the window is liberated, a harmonic vertical force can be applied, in addition to the static force described in the previous paragraph. To account for the effect of the window's inertia, a mass M, equivalent to that of the section of the window being modeled, is applied to the rigid window. By regarding the relationship between its displacement and the force applied by the seal F_{seal} (different from the external force due to inertial effects), we can calculate the value of the frequency-dependent stiffness of the seal. Figure 2.30 shows the results for the inverse of this stiffness $1/K_{dyn} = Y_{disp}/F_{seal}$. We can see that these curves have several peaks, due to the modes of the seals. However, given the considerable mass of the window with respect to that of the seal, it is

possible that the effect of these peaks on the whole system is negligible. In this case, instead of having a frequency dependent stiffness (such as the one in Figure 2.30), the effect of the seal could yet be simplified into a spring-damper system tied to a mass (the window), with constant values of stiffness k and damping coefficient c.

Figure 2.31 shows the transfer function between the harmonic applied excitation and the displacement of the window $TF = F_{ext}/Y_{disp}$. We can see that the seal modes don't have an influence over the entire system, and hence, we might be able to use the equivalent constant spring-damper simplification.

The transfer function of such a system is

$$\frac{Y_{disp}}{F_{ext}} = \frac{1}{(k - M\omega^2)^2 + (c\omega)^2} \tag{2.58}$$

If we consider small damping, then the resonant frequency of the system in Figure 2.31 (ω_d) can be considered very similar to the natural frequency of the undamped system and the value of the spring's stiffness is

$$k = \omega_d^2 M \tag{2.59}$$

The damping coefficient c can be calculated by replacing ω by the known value of ω_d in equation 2.58 and equaling it to the also known maximum value of TF.

Given the linearity of the material model for window seals, the Payne effect cannot be evaluated, and the response will be the same for any excitation amplitude. A simple, linear spring-damper model can thus replace the seal at all frequencies in the window model. For this specific seal, the stiffness is $k = 9270$ N/m and the damping coefficient is $c = 0.2324$ Kg/s. The comparison between the TF of the window seal model and the new equivalent model with the spring-damper system is shown in Figure 2.32.

2.3.4 Window Transmission Model

The Window Transmission Model uses the same ABAQUS acoustic tools than the previous 2 models. As such, the same zones can be found (Figure 2.34), with the singularity that one of the boundary conditions has a spring-damper system attached, equivalent to the effect of the window seal on the left extreme of the window, and obtained through the process described in the previous section. Again, the acoustic mesh is modeled with triangular elements, whereas quadrilaterals are used for the window itself. The final mesh is shown in Figure 2.33. Given the size of the window, this model is much heavier than those of the seals.

The resulting TL is shown in Figure 2.35. Here we can clearly observe the coincidence effect described in Section 2.1.2, at around 6000Hz. In this case, we can

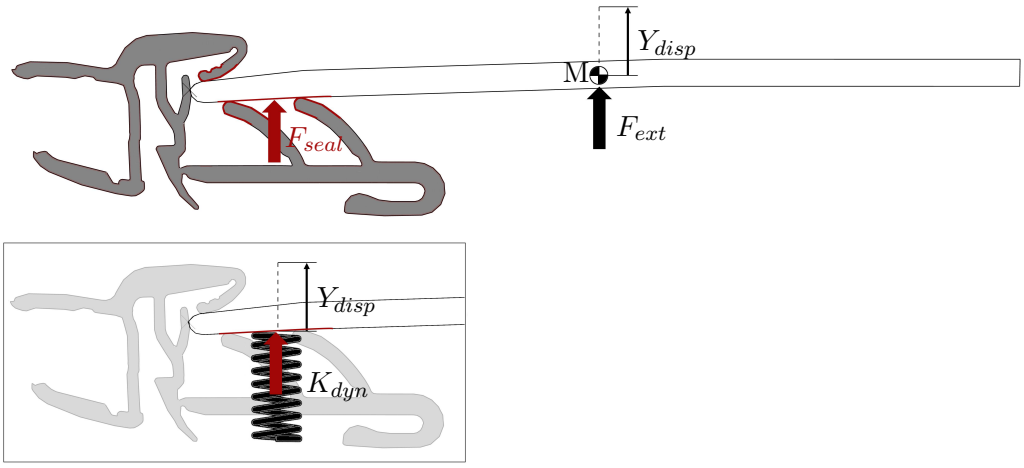

Figure 2.29: The seal's effect can be characterized by an equivalent dynamic stiffness

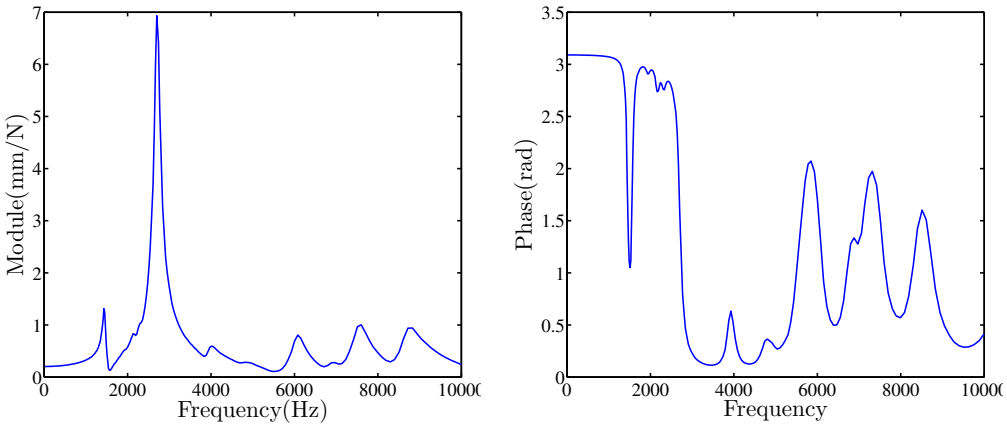

Figure 2.30: Values of $1/K_{dyn}$ for the equivalent seal

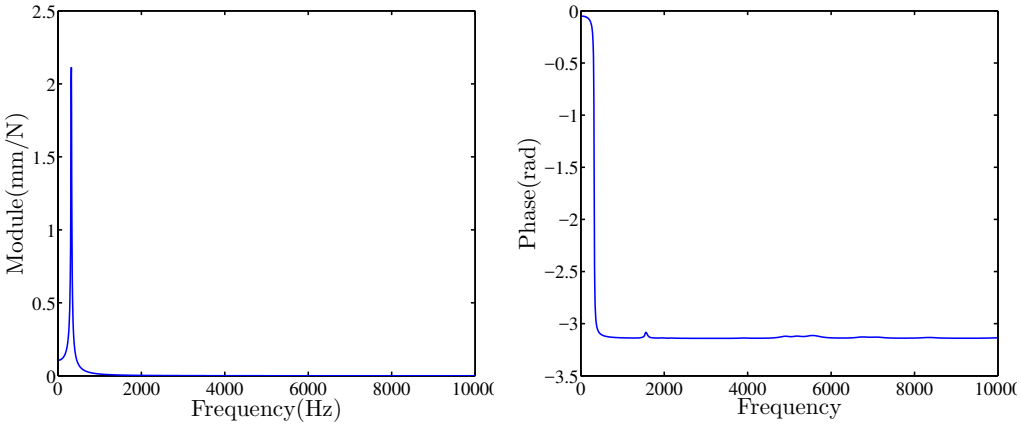

Figure 2.31: Values of TF for the window seal

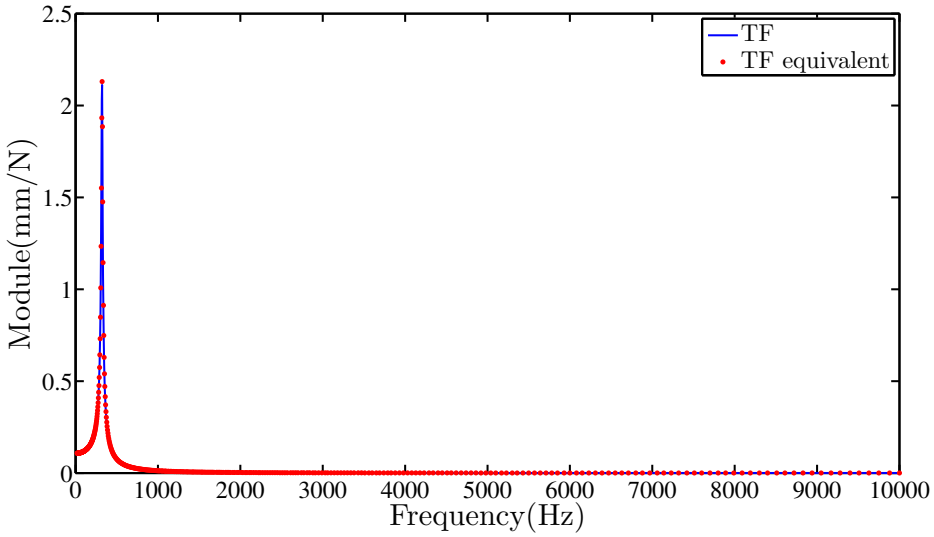

Figure 2.32: Values of TF for the window seal model and equivalent model

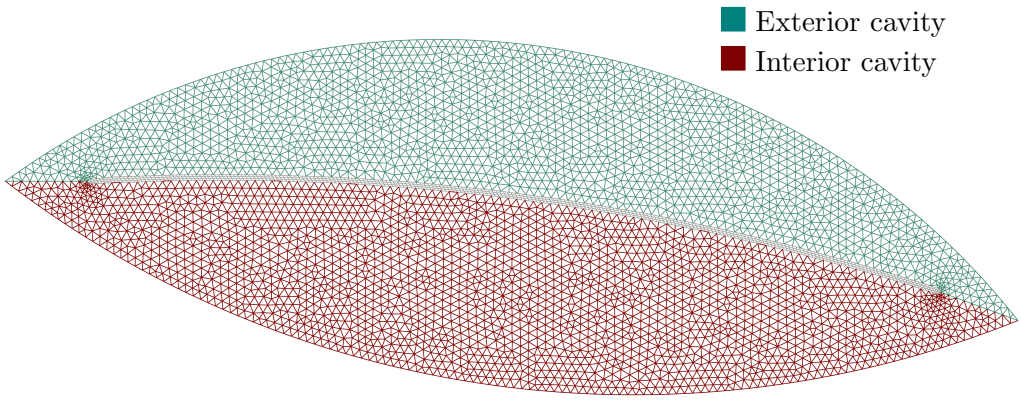

Figure 2.33: Window Transmission Loss model

see that 20 waves are barely sufficient to model the diffuse field, since at very high frequencies its TL curve differs from that of a 40-wave excitation. However, the difference is minimal, and to reduce time cost we will consider a 20-wave excitation acceptably accurate.

2.4 Experimental Validation

Even though the acoustic tools used in the transmission models seem to be accurate (given that the transmission loss curves of the simplified model match those of the paper cited above), an experimental validation is needed to ensure that the seals are correctly modeled under acoustic excitation. For simplicity, and as in the Static Model, only the door seal is tested, and we assume that whatever tools work for this seal will also work for the window and window seal models. The problem that needs to be experimentally tested involves a free-field (exterior) cavity, coupled to a section of the door seal in its compressed state, being excited by a diffuse field. In the physical environment, this corresponds to a section of the seal introduced inside a metallic structure, capable of simulating different seal compressions and allowing no sound leaking, placed between a reverberant room (diffuse field) and an anechoic (absorbent) chamber.

2.4.1 The test bench

The acoustic cabin

The means that are within our reach for this kind of test comprise the experimental system depicted in Figure 2.36, which we call the small cabin. It consists on an

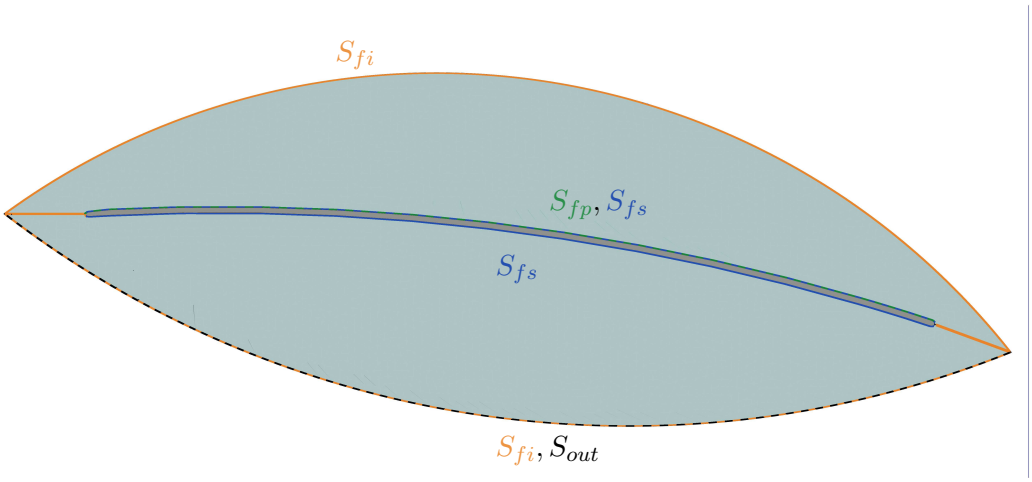

Figure 2.34: Boundary conditions on the window Transmission Model

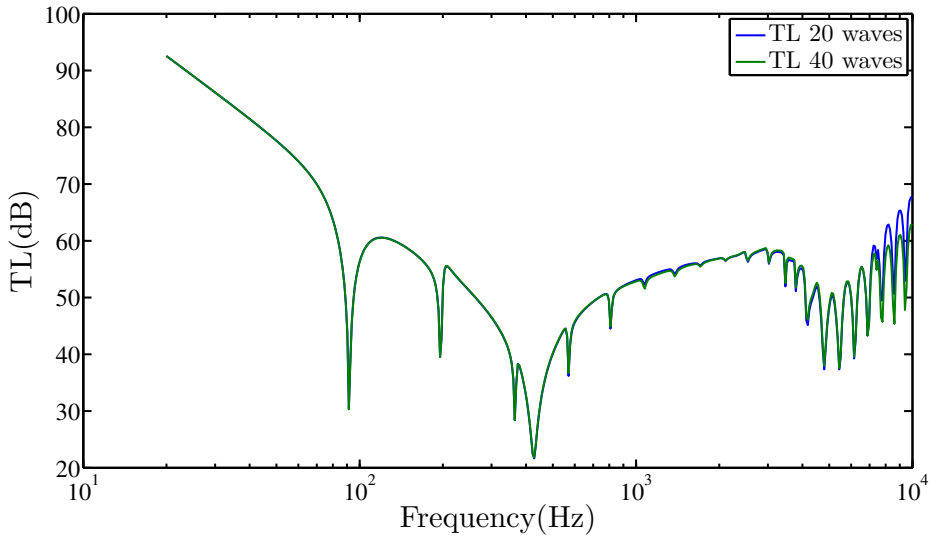

Figure 2.35: TL for the window, with replaced boundaries.

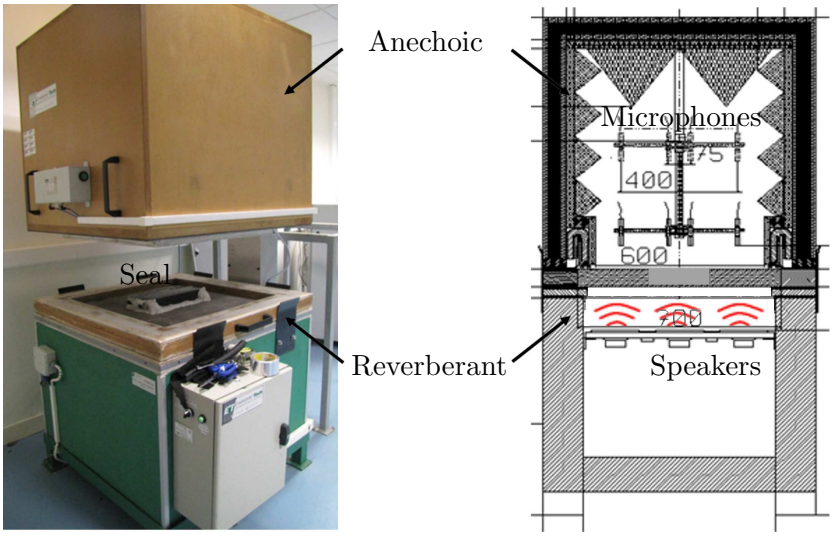

Figure 2.36: Acoustic cabin

assembly of two cavities, one supposedly reverberant, and one coated with an absorbent material, connected through a thin wall with a hole in its center (it is in fact a supported plate) on which an element whose transmission we want to test can be placed.

The emission is a white noise generated by a set of speakers, positioned as seen in picture 2.36. Low and high-pitched noises (50-2500 Hz and 3150-10000Hz respectively) are emitted separately. This emission is controlled by one single microphone, which ensures that the noise is in fact a white noise.

The semi-anechoic chamber has 4 microphones, placed at different distances from the walls, to measure the transmitted sound (Figure 2.37).

For every test, the experiments' software gives the sound pressure level throughout the whole frequency range of each receiving microphone, as well as of the control microphone in the emitting cavity. The pressures can then be obtained through

$$L_p = 20log\left(\frac{p}{p_{ref}}\right) \tag{2.60}$$

Where p_{ref} is $2e{-}5Pa$.

This test bench is actually conceived to see how the addition of an element, in the wall separating the cavities, affects the power ratio between them, in comparison with the case where there is no element at all (acoustic attenuation test). In consequence, the accuracy of the diffuse field or the absorbency of the cavities is not crucial, since what matters is that both cases are tested under the same circumstances, so that

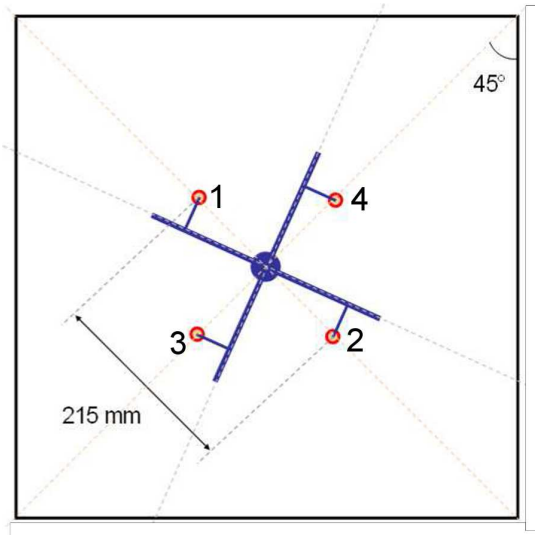

Microphone pair	Distance to the inter-cabin wall
1-2	75 mm
3-4	125 mm

Figure 2.37: Receiving microphone placement. View from the top of Figure 2.36

the comparison is appropriate. However, the experimental validation of the Seal Transmission Model needs these parameters to be precise. In consequence, we expect three sources of discrepancy between the experimental and numerical results:

- Poor absorbency for low frequencies: We can see in Figure 2.36, that the thickness of the absorbing layers in the "anechoic" chamber is of about 20 cm, for the top of the chamber, and 9cm at the side walls. The maximal wavelength of the sound waves corresponds to 50Hz, which yields 6,8m. From [Sed09], for low frequencies, a material is able to absorb waves with wavelength ten times bigger than its own thickness. This means that waves under 380Hz cannot be fully absorbed by the absorbing material, and thus the experimental results under this frequency will diverge from those of a fully absorbent cavity. However, since the interest of this study lies only on the frequency range from 400 to 10000Hz, this inefficiency of the low-frequency absorption should not have an impact on the accuracy of the experimental validation.

- Non-diffuse emission: The sound excitation comes from 9 speakers. The "reverberant" chamber is square, with no irregularities and the excitation is really close to the cavity-dividing wall, as we can see in Figure 2.36. In consequence, we cannot expect a real diffuse-field type of excitation, but rather one with some directivity and some cavity modes. The experimental results could hence differ from the model results throughout the whole frequency sweep. However, we expect some similarities through which we can semi-validate our numerical model.

- 3D-2D inaccuracy: The experimental procedure is done on a 300mm-long section of the seal. However, as it has been explained above, the Transmission

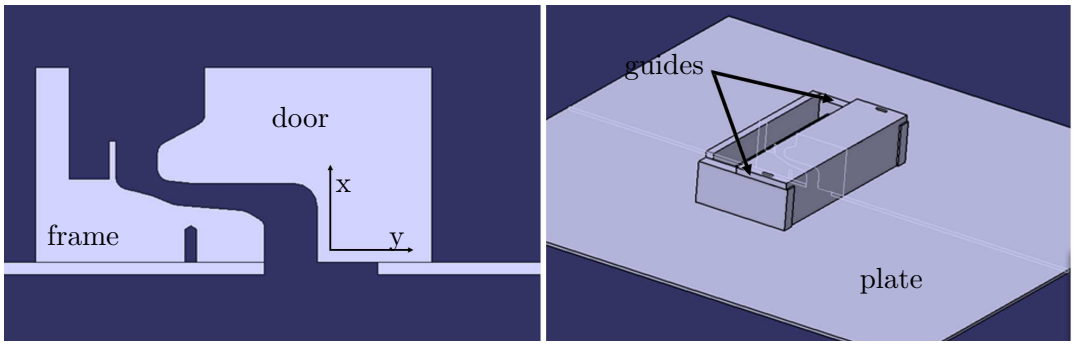

Figure 2.38: Experimental assembly for acoustic tests

Model is two-dimensional. It is hence obvious that the 3-dimensional behavior of the tests will not be represented in the numerical model.

The testing assembly

The architecture of the acoustic cabin described above, needs a structure to support the seal and position it in the middle of the dividing wall. This structure must also reproduce the geometry in contact with the seal, and be adjustable to every compression. The resulting conceived prototype is shown in Figure 2.38. It consists of 5 parts:

- A fix part representing the car frame where the seal is fixed.
- A mobile part acting as the door, which moves in the y direction to compress the seal to its 4 possible positions.
- Two rectangular pieces guiding the direction of the compression.
- A plate-like piece, that acts like the inter-cavities wall on which the other parts are fixed. This plates needs to have a hole in the middle with the length of the tested sections of the seal, and a width that allows the seal to be tested at its minimum compression.

All the parts are manufactured from pieces of aluminum.

More information on this prototype can be found in Appendix C.

Test Preparation

The entire assembly described above is placed between the two cavities, and a wood frame is placed on it to ensure the junction. The exposed surface of the plate is then covered with 2 kinds of sound reducing materials. The first layer is a sound absorbing wadding, 4cm thick, and with a density of $1.2kg/m^2$. Over this fabric, a

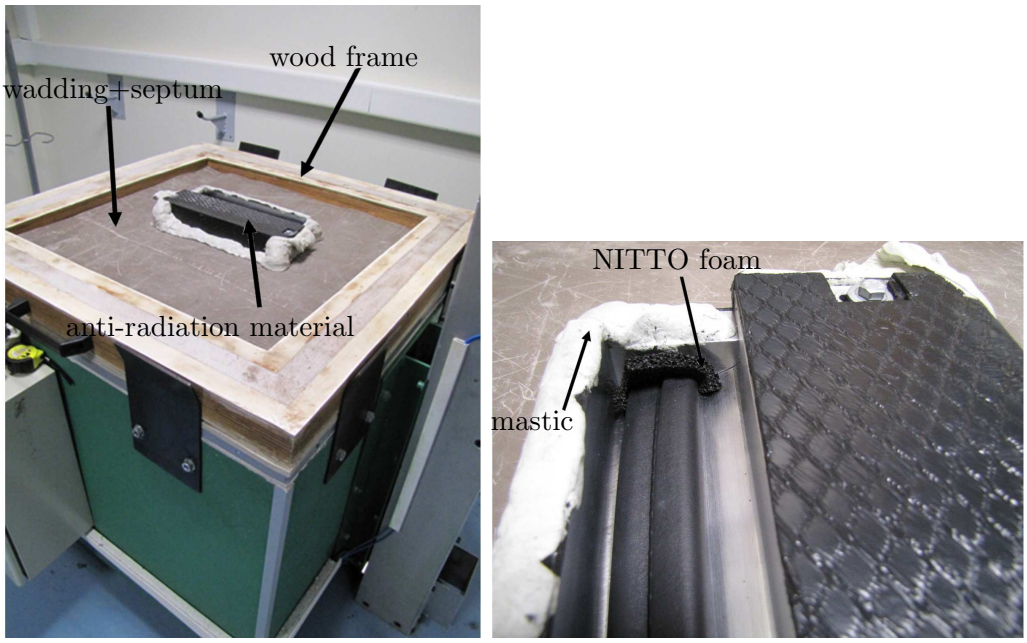

a) b)

Figure 2.39: a) Several elements are added in order avoid unwanted radiation b)Nitto and mastic are used to prevent leakage

set of septum layers, with a total weight of $20kg/m^3$, is used. This additional weight prevents the vibration of the aluminum plate, and thus, its radiation to the receiving chamber. The pieces that constitute the support of the seal must also be covered with a heavy material, to avoid its radiation's interference with the results. All these insulating elements are shown in Figure 2.39.a.

Another thing that must be prevented for good experimental results, is sound leakage through the junctions between the elements. Given the need of repeatability, the masking of these leaks must be non-destructive, hence we have chosen to use acoustic mastic. However, on the extremes of the seal, this technique cannot be used because it limits their movement thus changing the results. As a consequence, the seals are cut longer than necessary (305mm), and NITTO foam of 5mm thickness is placed between their extremes and the support (see Figure 2.39.b). Finally, the sound insulation efficiency is verified using a sound leak detector.

Procedure

Much as for the static experiments, different seal sections are tested for the validation of the acoustic model. Using the nomenclature in Chapter 1 and Figure 1.22, 2 sections of 3 different seal profiles have been tested in each one of the 4 possible

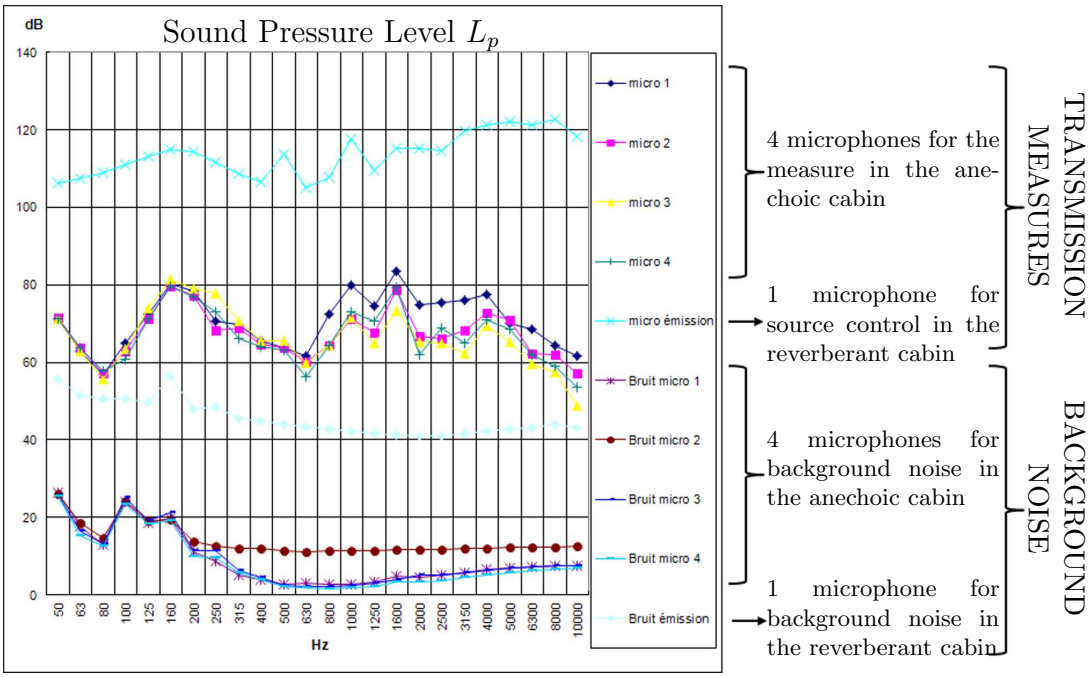

Figure 2.40: Example of the results in the outputted excel file for J3S1 H3

positions H1, H2, H3, H4 in Figure 1.9.

For each tested seal, the section is placed by pushing it against the frame as described in the Introduction. One piece of NITTO foam is placed on each side, as shown in Figure 2.39.b. Next, the movable part is positioned to minimal compression (H3), and the mastic is placed and verified with the leak detector. A background noise test is made first, to ensure that this type of noise is much smaller than the excitation and that it will not interfere with the results. This step is repeated once for every seal profile, but not for every compression.

Finally, a white noise, first of 50-2500Hz and then, in a second step, of 3150-10000Hz is applied, and the results processed by the system and outputted by third octave bands in an excel file. An example of these results can be seen in Figure 2.40.

The compression is modified to H1 and the steps are repeated, until maximum compression H4. Then the seal is changed and the whole process starts again.

2.4.2 Experimental results

From the results outputted on the excel file, we can already see some problems. As we can observe in Figure 2.40, the microphone in the emitting cabin doesn't capture a true white noise. The light blue curve shows that the sound level isn't constant

throughout the frequency sweep, but tends to rise at higher frequencies (over 15dB of difference). We can see a clear difference of mean sound level between the low-pitched frequency emission (up to 2.5KHz) and the high-pitched white noise (3.15 to 10KHz). Additionally, we can observe some peaks at different frequencies. This confirms the hypothesis that we formulated above, that the excitation cannot be diffuse, since the emission cavity modes are likely to have an influence on the overall sound level of the cabin. We can see in Figure 2.40 how these peaks of emitted sound are transmitted into the reception cabin, creating similar peaks at the same frequencies in the lectures of the 4 microphones in the anechoic cabin. We deduce that for frequencies under 2000Hz, the modes of the emission cavity are likely to importantly disturb the response measured in the anechoic cabin.

The results for J1S1 are not taken into account. This is due to the fact that this section of the seal was too long for the experimental set-up, and didn't fit correctly and bended when introduced in the experimental support, compromising the soundproofing. Figure 2.41 shows the comparison of the transmission loss curves between all the other seals, for H1 compression. As we can see, almost all the seals have essentially the same behavior for low frequencies, and the curves start to diverge after 500Hz. We don't observe a particular concordance for sections of the same seal profile.

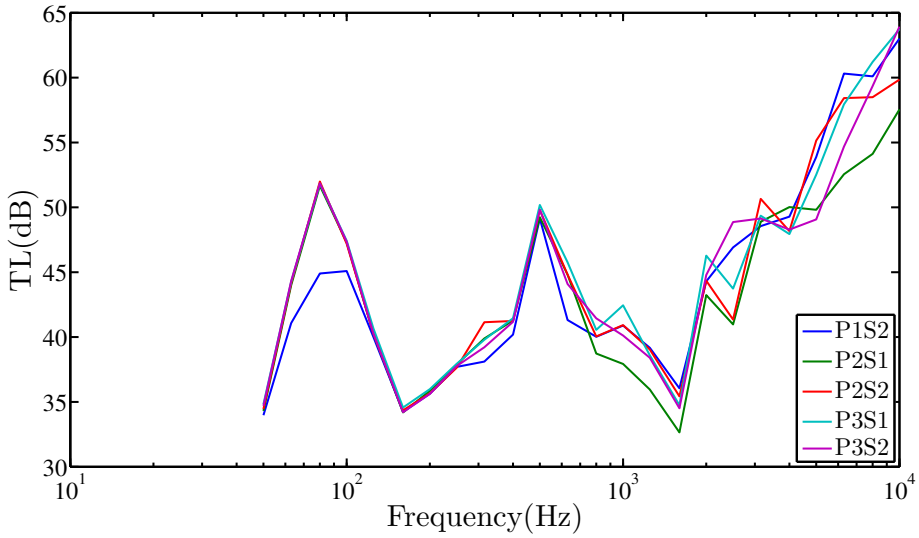

Figure 2.41: Experimental TL curves for H1 compression for each seal section

Experimental compression influence analysis

To account for the influence of compression on sound transmission loss, Figure 2.42 shows the TL curves for the mean values of all seal sections for different compressions

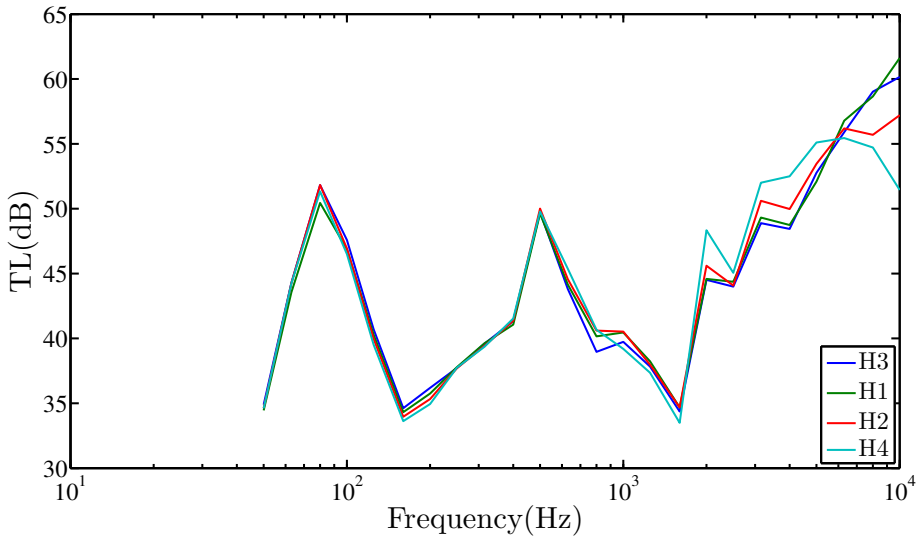

Figure 2.42: Experimental TL mean curves of all seal sections for each compression level

(H3 to H4).

In this figure we observe again the similar behavior for low frequencies. The transmission loss curves start to diverge over 2000Hz, for which the higher the compression, the higher the TL. For frequencies 5000 to 10000Hz however, this behavior is reversed and, for big compressions, the more compressed the seal is, the more sound it lets through.

Repeatability tests show the experimental error to be negligible.

2.4.3 Numerical Transmission Model for experimental validation

The numerical model has to match the geometry of the experimental setup described above. Additionally, we need to output the pressure levels in the numerical model at the approximate distance where we would find the 4 receiving microphones in the experimental cabin. In consequence, the Door Seal Transmission Model detailed in Section 2.3.2 is modified, the resulting geometry and output points are shown in Figure 2.43.

Several waves are applied to recreate the diffuse field. Since the real incident power in the emitting room is unknown, we have decided to change the amplitude of the numerical incident waves in each frequency, to fit the sound power captured by the microphone in the emission chamber. The total incident sound power level inputted in the numerical model is hence represented by the emission curve in Figure 2.40.

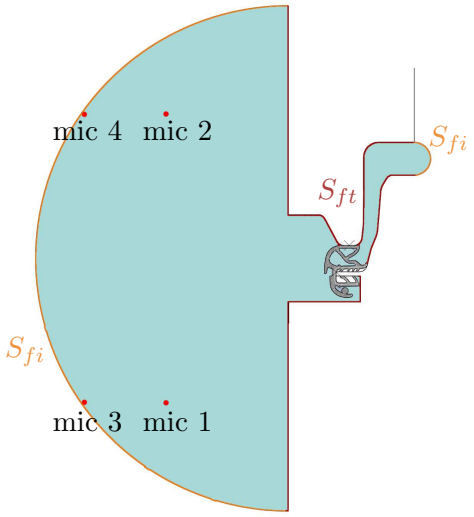

Figure 2.43: Numerical model for comparison with experimental results. Each red point corresponds to a microphone

We believe this approximates better to the resulting excitation of the seal than that of a real diffuse field, with constant sound power level for all frequencies. However, a quick study shows that the influence of this change on the numerical model is negligible.

We have also observed that the results of the numerical model present close to no difference between the TL for a single wave excitation and the TL of a diffuse field. This might be due to the fact that the results are presented in third-octave bands, which smooths all coincidences and modes of the single wave excitation.

2.4.4 Comparison of the experimental and numerical transmission loss curves

Figure 2.44 shows the comparison between TL, for the converged numerical model and the experimental results on J2S2. We will only compare case H1 for all seal sections with the numerical model results. All results will be expressed in third octave bands unless specified otherwise. As expected, for low frequencies we seem to find much more noise in the experimental reception chamber (low transmission loss) than in the numerical case.

For the rest of the frequencies, the numerical curves don't seem to correspond to those of the experimental procedure. The former fluctuates importantly, whereas the latter presents only small oscillations. The mean value of the curves is fairly similar, with up to 6 dB of difference depending on the frequency. This can be observed in Figure 2.45, where the same curves are plotted for octave bands instead of third-

octave.

Again in Figure 2.44, we can observe that for frequencies over 2000Hz the fluctuation of the numerical TL curves seems to almost correspond to that of the experimental results, not in value, but in the placement of the peaks and dips (especially for the dip at 2500Hz). However, for mid-frequencies, there is close to no correspondence of the peaks and dips. This could be due to the fact that, it is in this frequency range (400-2000Hz) that we find the most irregularities in the output of the experimental emission curves of Figure 2.40, which, as mentioned above, we believe to be caused by the non-diffuse emission's cavity modes.

In general, the numerical curve is higher than the experimental. Since the sound power level in the incident cavity is the same for the experimental tests and numerical model, this means that the receiving microphones sense more sound in the anechoic cabin than the equivalent value accounted for in the numerical model. This agrees with the hypothesis that the 2D model cannot fairly represent the 3-D behavior of the seal section. The microphones could be registering the effect of three-dimensional flexural modes, or simply the radiation contributed by every transverse section of the 3-D seal, whereas the numerical model can only calculate the radiation of one of these transverse sections. Additionally, we find that the numerical curve presents higher oscillations than the experimental curve, even for the zone where the peaks and dips are coincident in frequency. Since FE software ABAQUS isn't a specialist in IE, this could be caused by some numerical fictitious resonances on the infinite element boundary, caused by the truncation of the infinite domain, and the subsequent numerical approximations needed to simulate an unbounded space through a finite model. We also consider the possibility of some error in the material coefficients rudimentarily calculated in Section 2.2.4.

All in all, the correlation between experimental and numerical TL curves is not correct. We believe that this is due mainly to the bad experimental conditions, and that the experiments should be repeated in a truly reverberant/anechoic structure. For optimal results, we would also advise the repetition of the viscoelasticity calibration test, and the creation of a 3D model capable of fully representing the acoustic phenomena in experimental cabin.

However, although we cannot fully validate the numerical model, some similarities with the experimental results, as well as the pre-validation procedure explained in Section 2.3.1, drive us to believe that it is fairly accurate, and hence to continue with the described strategy.

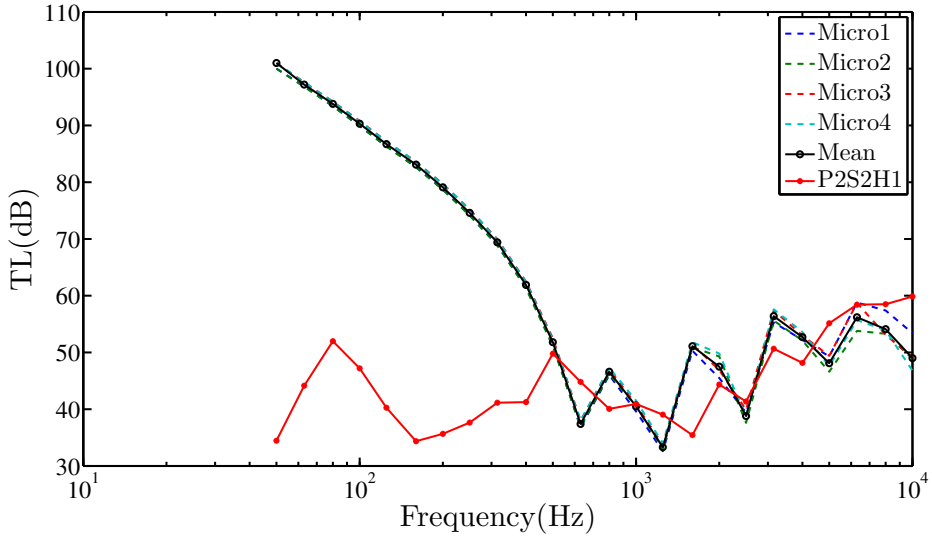

Figure 2.44: Experimental TL curve for J2S2H1 vs. numerical curves for the 4 "microphones" and its mean value

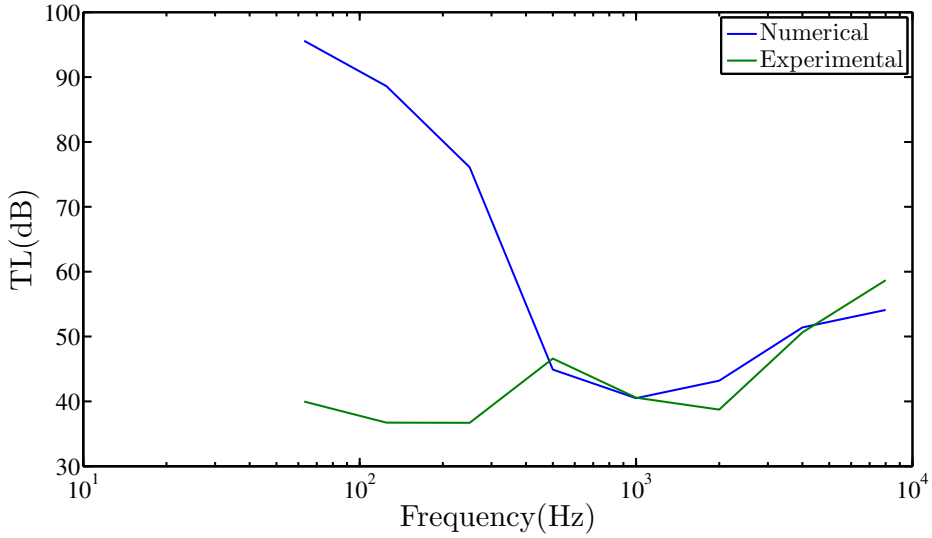

Figure 2.45: Experimental TL curve vs. numerical microphones mean TL, per octave band

2.5 Conclusions

In this chapter we have described the process to the obtainment and validation of the sound transmission models for door seals, window seals, and windows. Before the construction of such models, the dynamical behavior of all the materials in window, window seal and door seal models must be taken into account and coupled with the elastic properties described in the previous chapter. This dynamical behavior is expressed as structural damping around linear elasticity for the window and window seal models. For the door seals however, viscoelastic properties need to be introduced. Nevertheless, the information on these properties is incomplete for some of the seal's materials. To solve this, a set of experimental tests allowing the calibration of the Prony series viscoelastic coefficients through comparison with a numerical model have been carried out, and are explained in detail in this chapter.

The goal of the transmission models is to export the deformed and stressed elements at the end of the static models described in the previous chapter, excite them with an acoustic source and output the TL curves that relate the input and output power. All this is achieved using the acoustic tools available in the FE software used by PSA Group (ABAQUS), which allow us to impose different excitations and types of boundary conditions on each element (door seals, window seals and windows). Given that these tools are fairly uncommon, a Simplified Transmission Model, for which a benchmark solution can be found in the bibliography, has been built initially. The results obtained through this model can be ratified by comparison to the benchmark solution, allowing the validation of the acoustic tools used in the modeling. Once these tools have been validated, the same procedure is applied to both seals as well as the window.

Additionally, the boundary conditions on the window, generated by the window seals, are studied. The stiffness of the contact is characterized in a way that the window seal can be completely replaced by a dynamic, frequency-dependent spring in the window model. In doing so, all the dof of the seal do no longer need to be accounted for in this model, substantially reducing its size.

As in Chapter 1, only the results of the Door Seal Transmission Model are compared to some experimental tests, and we assume that if the results are validated for this model, the validation applies for the rest of the transmission models. For the tests, an experimental set-up has been conceived and tested inside an acoustic cabin. However, the inaccuracy of the experimental test bench at our reach, prevents us from attaining a good correlation between the numerical and the experimental results. Nevertheless, some similarities are found, which have led us to believe our door seal model not far from correct, and, in lack of other experimental means to fully validate it, to the decision to carry on with the chosen modeling strategy.

2.6 Expansions

As explained in the previous section, the acoustic experimental tests have not allowed us to fully validate the Door Seal Transmission Model. In consequence, a new set of experiments in an adequate test bench, is the first action that should be taken as an expansion of this study. In a similar way, the procedure to obtain the viscoelastic coefficients for this model is very rudimentary, and a new characterization with more suitable experimental tools is advisable.

Additionally to the improvement of the previously described work, we have several propositions to enlarge it that we think could lead to interesting results in future studies.

From a material point of view, we have already described in the previous chapter the need for a good characterization of the window seal materials, which have been greatly simplified in this work, as described in the Introduction. The need for a more complex and precise material characterization still applies in this chapter, and is extended to its dynamic behavior in addition to its elastic demeanor. In the case of the door seal, some of the materials had already been characterized by the provider, but the compressible EPDM we have characterized ourselves through some experimental tests. However, these are very rudimentary, and allow only the calibration of one set of Prony Series parameters. In consequence, it would be advisable to redo these tests in the already existing test-benches specially conceived for this use.

Regarding optimization, no parameter influence has been presented in this chapter, with the exception of the experimental seal compression. The impact of the compression in the numerical Transmission Model, as well as that of the door-seal contact are both examples of possible research to carry out before the optimization.

Finally, the Payne effect mentioned in the Introduction, which is the effect of the amplitude of the excitation on the dynamic response of the element, has not been taken into account for the seals. Its inclusion is another aspect of the study that should be taken into consideration on a posterior extension of the work described here.

2.7 Bibliography

[AM06] Jean-Christophe Autrique and Frédéric Magoulès. Studies of an infinite element method for acoustical radiation. *Applied Mathematical Modelling*, 30(7):641–655, July 2006.

[Bar13] E.J. Barbero. *Finite Element Analysis of Composite Materials Using ANSYS®, Second Edition*. CRC Press, December 2013.

[Bow09] A.-F. Bower. *Applied Mechanics of Solids*. CRC Press, October 2009.

[Das14] Dassault Systems. Abaqus 6.14 Theory Guide Documentation, 2014.

[DB08] E. Dikmen and I. Basdogan. Material characteristics of a vehicle door seal and its effect on vehicle vibrations. *Vehicle System Dynamics*, 46(11):975–990, November 2008.

[Fah00] F. J. Fahy. *Foundations of Engineering Acoustics*. Academic Press, September 2000.

[Gac07] H. Gacem. *Comportement visco-hyperélastique des élastomères: Viscoélasticté non linéaire, Application aux Multicouches [french]*. PhD thesis, Université Pierre & Marie Curie - Paris VI, 2007.

[Ger00] K. Gerdes. A review of infinite element methods for exterior helmholtz problems. *Journal of Computational Acoustics*, 08(01):43–62, March 2000.

[MO92] H. J.-P. Morand and R. Ohayon. *Interactions fluides-structures*. Masson, 1992.

[Mös09] M. Möser. *Engineering Acoustics: An Introduction to Noise Control*. Springer Science & Business Media, September 2009.

[NK03] M. P. Norton and D. G. Karczub. *Fundamentals of Noise and Vibration Analysis for Engineers*. Cambridge University Press, October 2003.

[Nun10] P.-M. Nunez Trujillo. Electroacústica. `http://tsc.unex.es/~pnuntru/2009..10/EA/indexEA.html`, 2009/2010.

[PT12] I. Prasetiyo and D. J. Thompson. Study of the effect of finite extent on sound transmission loss of single panel using a waveguide model. In *Proceedings of the Acoustics 2012*, Nantes, France, April 2012.

[Saa03] P. Saad. *Modélisation et identification du comportement non linéaire des cales en caoutchouc [french]*. PhD thesis, Ecole Centrale de Lyon, 2003.

[Sch05] Scott D. Schrader. Modeling Thermoplastic Vulcanizate Seals with ABAQUS. In *ABAQUS Users' Conference*, 2005.

[Sed09] H. S. Seddeq. Factors influencing acoustic performance of sound absorptive materials. *Australian Journal of Basic and Applied Sciences*, 3(4):4610–4617, 2009.

Chapter 3

Acoustic Propagation Model

This chapter describes the methodology used for the implementation of an energy model capable of predicting the propagation of the sound transmitted through the seals into the vehicle cavity. This model is to be coupled to each of the three TL models described in Chapter 2.

Up until now, we have described the procedure to locally analyze the transmission of sound, only through the seals or windows. However, it has been mentioned that it is its propagation into the vehicle cabin that is of most interest in a search for seal optimization. We have explained in the introduction how, in the range of frequencies of this study (400Hz-10000Hz), there is a relevant amount of modal overlap, and thus an analysis through the FE method of the entire volume of the vehicle cavity, with the required very fine discretization, would imply costly calculation times. An energy model is better suited instead.

The most known energy model for the prediction of the sound pressure level of a cavity is the Statistical Energy Analysis (SEA). However, in this method, each subsystem is represented by a single value, an averaged energy which provides only global information. Since the interest of this study is to reduce passenger discomfort, a more local approach is intended. This problem is solved through the Méthode Énergétique Simpliefiée (MES), a simplified energy method which allows a fast, local calculation of the energy values in a cavity, with only a coarse boundary mesh. The application of this method to our specific case, with its consequent simplifications, is described here.

This method has some limitations, especially for the treatment of very directive sources and near acoustic fields, as is the case of the radiating seals. An improvement is thus proposed and applied in this chapter, its results validated through comparison with a heavy FE simulation of the entire cavity.

The resulting methodology is validated through comparison of the improved MES on a door seal, with an equivalent FE model including the entire interior cavity.

3.1 Simplified Energy Method (MES)

We have already stated that the MES derives from the better known Statistical Energy Analysis (SEA) method, which divides the problem into subsystems and calculates the flow of energy in-between them ([Lyo03]). However, in the SEA the information is given globally for an entire subsystem. In order to have local data, the system must be divided into small subsystems, all coupled in-between them, which adds complexity to the model. The need of a lighter, local approach for vibroacoustic design, led to new energy methods providing energy spatial distribution around a vibrating element. Among these new methods the power flow method was introduced by Nefske and Sung [NS89] and improved in [WB92],[BB95a] and [BB95b]. This new approach also led to the formulation of the General energy method (MEG), found in references [LIJ96],[ILJ97]. This method characterizes the propagation and modal behaviors of the system through 4 variables: total energy density, active energy flow, Lagrangian energy density and reactive energy flow, where the last two are known to describe mainly wave interferences or singularities. Hence, if we neglect wave correlation for mid and high frequencies we can eliminate these 2 variables. This leads to a phase-averaged, local energy approach formulation, which is the base of the MES. This formulation has been applied to several structures such as beams, plates and membranes (references [BB95a]-[LIJ96], [WVW04]and [Mor98]), however in this dissertation our main concern is its application to acoustic radiation (references [WVW04], [Cot01] and [CLJ02]).

There are two main formulations of the MES, depending on the method chosen for the resolution of the equations. The differential MES uses plane waves to solve the problem, whereas the MES in integral form, takes into account cylindrical (2D) or spherical waves (3D).

3.1.1 Theory and assumptions

Let us consider a linear isotropic system, in a steady-state regime at pulsation ω. If we focus in an elementary volume such as the one depicted in Figure 3.1, the energy balance in this volume is represented by equation

$$\Pi_{inj} = -\boldsymbol{\nabla} \cdot \mathbf{I} - \pi_{diss} \tag{3.1}$$

with Π_{inj} the energy injected into the volume, and $\mathbf{I}$ the energy flow per unit of surface. π_{diss} is the dissipated energy in the volume and, as in SEA, it is considered proportional to the total energy in the volume W(see equation 3.2).

This equation is exact if we consider the real and imaginary parts of the injected power, as does the MEG in [ILJ97]. The MES attempts, by assuming several hypothesis, to solve this problem considering only the active part of this power. These hypotheses are formulated as follows:

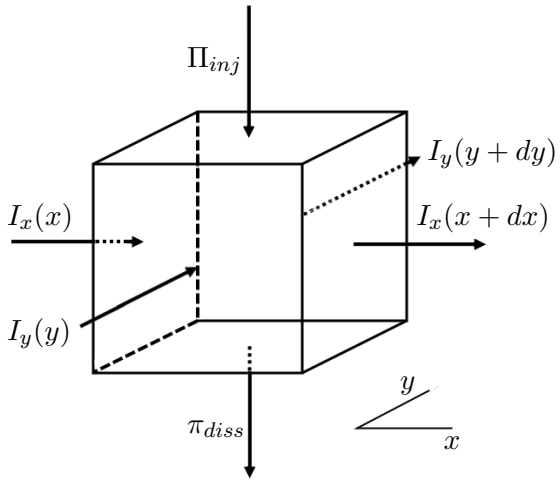

Figure 3.1: Energy balance in an elementary volume

- Only the real part of the energy exchanges is taken into account.
- The dissipated energy in an elementary volume M is considered proportional to the energy density $W(M)$, hence

$$\pi_{diss} = \eta\omega W \tag{3.2}$$

  With η the damping coefficient. Note that this is only true for the far field, or when reverberation is sufficient so that the far field is predominant over the near field, and if damping is not high.

- Due to the fact that only the active part of the power is considered, evanescent waves are not taken into account. Only propagation waves are thus treated, which implies that, near the singularities (such as directive sources), where the participation of evanescent waves is relevant, MES cannot predict correct energy values.
- Waves are assumed to be uncorrelated. As a consequence, the energy of each wave is simply summed, instead of computing the energy of the total resulting wave. If u_1, u_2 are the amplitudes of two waves, their associated energy is:

$$|u_1 + u_2| = \underbrace{|u_1|^2 + |u_2|^2}_{\text{terms taken into account}} + \underbrace{u_1^* u_2 + u_1 u_2^*}_{\text{terms with an average value of 0}} \tag{3.3}$$

  This hypothesis is consistent with the fact that, for mainly reverberant fields, the last terms in equation 3.3 are averaged out. Note that not considering these terms is equivalent to neglecting the phase of the waves in the cavity. In consequence, the modal information on stationary waves resulting from the constructive interference of two waves is not taken into account.

In summary, the MES is a mid-high frequency energy method, with a frequency averaged energy output, valid only for far fields and which cannot represent directive sources. From equation 3.1 and 3.2 the main equation from the MES becomes

$$\frac{dW}{dt} = -\boldsymbol{\nabla} \cdot \mathbf{I} - \eta\omega W \tag{3.4}$$

As we have explained, the MES has several variants. For this study we have chosen the integral MES, which is better adapted to acoustical problems and in 2D solves equation 3.4 using cylindrical waves. For further information on MES and its different variants refer to [Har05] and [BIJ10].

For the far field, cylindrical waves can be simplified to plane waves ([Sch04]), and so W and $\mathbf{I}$ are related through:

$$\mathbf{I} = cW \cdot \mathbf{n} \tag{3.5}$$

$\mathbf{n}$ being the unit normal vector at the boundary of the elementary volume and c the sound speed. This expression is only valid for non-damped wave fields.

With these types of waves, given a unitary input of energy at $r = 0$, where r is the distance between the source and the measured point, expressions (3.1), (3.2), and (3.5) yield

$$\frac{1}{r}\frac{\partial}{\partial r}(rW) + \frac{\eta\omega}{cW} = \frac{\delta(0)}{c} \tag{3.6}$$

for which the solution in terms of W is the Green function

$$G = \frac{1}{\gamma_0 c}\frac{e^{-\eta\omega}}{r} \tag{3.7}$$

Given that in this study the transmission of sound is done through elements on the exterior surface of the cavity, we will consider these elements surface sources, injecting an amount of energy into the vehicle. The total energy density at a specific point M is thus equal to the participation of all sources in the vehicle cavity's surface. Through expression 3.7, the participation of a source in P to a point in M is

$$W(M) = \int_{\partial\Omega} \Phi^{inj}(P) d_\Phi(P, M) G(P, M) dP \tag{3.8}$$

Where Φ^{inj} is the power injected by source P and d_Φ is the directivity. The meaning and expression of the latter are detailed in Section 3.1.2.

In order to take into account reflections, the total energy in a point is represented as a superposition of the direct field W_{dir}, and the reverberant field W_{rev} (Figure 3.2).

$$W = W_{dir} + W_{rev} \tag{3.9}$$

The direct field comes from the participation of the actual sources (seals and window), which are called primary sources. The reverberant field can be considered as the result of secondary (fictitious) sources at the boundaries, resulting from reflections (Figure 3.3). With this division, the injected power in equation 3.8 can be represented by

$$\Phi^{inj} = \Phi^{dir} + \sigma \tag{3.10}$$

With Φ^{dir} the power injected from primary sources and σ the reflected power, from the secondary sources. From equation 3.8, the direct and reverberated field energy densities are expressed as

$$W_{dir}(M) = \int_{\partial\Omega} \Phi^{dir}(P) d_\Phi(P, M) G(P, M) dP \tag{3.11}$$

$$W_{rev}(M) = \int_{\partial\Omega} \sigma(P) d_\Phi(P, M) G(P, M) dP \tag{3.12}$$

Where $\sigma(P)$ is the power reflected in surface point P.

We know that when a wave impinges on a surface, part of its energy is absorbed by the material and the rest is reflected back into the media where the wave travels. We also know that the absorbed energy is proportional to the impinging energy, through an absorption coefficient α characteristic of the surface's material. Thus, the reflected power σ is related to the impinging power Φ_{imp} through

$$\sigma = (1 - \alpha)\Phi_{imp} \tag{3.13}$$

In the MES, the impinging power on a point P of the surface is the sum of the power emerging from the real sources, and the power coming from the reflections on all the other points P' of the surface.

$$\begin{aligned}\Phi_{imp}(P) = &\underbrace{\int_{\partial\Omega} \Phi^{dir}(P') d_\Phi(P', P) G(P', P) cos\theta dP'}_{\text{power from primary sources in P'}} + \\ &\underbrace{\int_{\partial\Omega} \sigma(P') d_\Phi(P', P) G(P', P) cos\theta dP'}_{\text{power coming from the reflections in P'}}\end{aligned} \tag{3.14}$$

With θ the impinging angle. From equations 3.13 and 3.14, the power injected by a secondary (fictitious) source in point P is

$$\begin{aligned}\sigma(P) = (1 - \alpha(P))\Big[&\int_{\partial\Omega} \Phi^{dir}(P') d_\Phi(P', P) G(P', P) cos\theta dP' + \\ &\int_{\partial\Omega} \sigma(P') d_\Phi(P', P) G(P', P) cos\theta dP'\Big]\end{aligned} \tag{3.15}$$

With $\eta << 1$ in the fluid, we discretize the boundary with N_e elements. Given an element i of the mesh, if we consider Φ_i^{dir} and σ_1 constant throughout the element, equations 3.11 and 3.12 become

$$W_{dir}(M) = \sum_{i=1}^{N_e} \frac{\Phi_i^{dir}}{c_0} \int_{S_i} \frac{d_i(\theta)}{r_i} dP \tag{3.16}$$

$$W_{rev}(M) = \sum_{i=1}^{N_e} \frac{\sigma_i}{c_0} \int_{S_i} \frac{d_i(\theta)}{r_i} dP \tag{3.17}$$

With $r = ||\overrightarrow{PM}||$, θ the angle between the normal vector $\mathbf{n_i}$ and vector $\overrightarrow{PM}$, and $d_i(\theta)$ the directivity of element i. Observe that the solid angle in equation 3.7 has been replaced by a directivity. If we consider α_i the absorption coefficient of element surface S_i, then, integrating equation 3.15 over this surface

$$\begin{aligned} \sigma_i S_i = (1-\alpha_i) \Bigg[& \sum_{\substack{j=1 \\ j\neq i}}^{N_e} \Phi_j^{dir} \int_{S_i} \int_{S_j} \frac{cos\theta_i d_j(\theta)}{r_{ij}} dP_i dP_j + \\ & \sum_{\substack{j=1 \\ j\neq i}}^{N_e} \sigma_j \int_{S_i} \int_{S_j} \frac{cos\theta_i d_j(\theta)}{r_{ij}} dP_i dP_j \Bigg] \end{aligned} \tag{3.18}$$

From a matrix point of view, equation 3.18 can be rewritten, for all N_e elements as

$$\mathbf{M}\boldsymbol{\sigma} = \mathbf{B} \tag{3.19}$$

With

$$\begin{aligned} \mathbf{M} &= \mathbf{I} - (\mathbf{I} - \boldsymbol{\alpha})\mathbf{T} \\ \mathbf{B} &= (\mathbf{I} - \boldsymbol{\alpha})\mathbf{T}\boldsymbol{\Phi}^{\boldsymbol{dir}} \end{aligned} \tag{3.20}$$

Where $\boldsymbol{\alpha} = \delta_{ij}\alpha_i$ is the matrix of absorption coefficients. The double integrals in equation 3.18 can be simplified by assuming that, given a specific secondary source element S_i, the terms inside these integrals do not have a relevant variation throughout the element. In consequence these terms can be evaluated for a point at the center of this element. Hence, equation 3.18 is simplified and matrix $\mathbf{T}$ of equation 3.20 can be expressed through

$$\mathbf{T_{ij}} = \int_{S_j} \frac{cos\theta_i d_j(\theta)}{r_{ij}} dP_j \tag{3.21}$$

It is the construction of this matrix $\mathbf{T}$ that will constitute the main cost of the simulation. Equation 3.19 can be rewritten using the expressions in 3.20 to give

$$\boldsymbol{\sigma} = \mathbf{M^{-1}B} = \mathbf{M^{-1}}(\mathbf{I} - \boldsymbol{\alpha})\mathbf{T}\boldsymbol{\Phi}^{\boldsymbol{dir}} \tag{3.22}$$

The direct and reverberated fields in equations 3.16 and 3.17 can be expressed through

$$\mathbf{W} = \mathbf{Y^W \Phi^{dir}} + \mathbf{Y^W \sigma} \tag{3.23}$$

Where $\mathbf{Y^W}$ is

$$\mathbf{Y^W_{ij}} = \frac{1}{c_0} \int_{S_i} \frac{d_i(\theta)}{r_i} dP \tag{3.24}$$

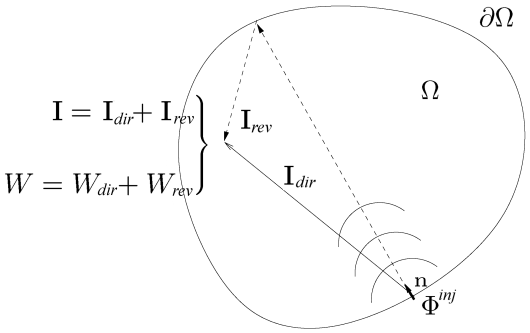

Figure 3.2: The total intensity and power in one point are the sums of their direct and reverberant field components

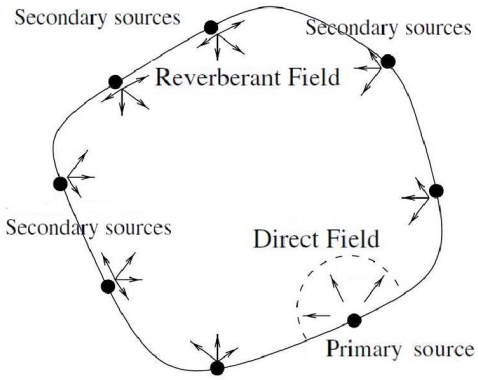

Figure 3.3: The reverberant field is assimilated to the direct field of secondary sources

3.1.2 Directivity

The precision of this method depends on the accuracy of the choice for directivity d_θ. The conventional d_Φ used for the MES is based on Lambert's emission law, which states that a source emits energy in every direction (diffusive character), and that it does so in a non-uniform way, proportional to the angle of emission θ. Since the sum of the directivity for all possible emission angles must be equal to 1, in 2-D we have:

$$d_{n=2}(\theta) = \frac{cos(\theta)}{2} \tag{3.25}$$

$$\int_{\frac{-\pi}{2}}^{\frac{\pi}{2}} d_{n=2}(\theta) = 1 \tag{3.26}$$

This directivity is used for the emission of the primary sources as well as for the re-emission of reflected sound rays (secondary sources). However, although we can assume reflections are re-emitted in a diffuse way because of the roughness of the surface (Figure 3.4), the primary sources can have completely non-diffuse directivity (ex: dipoles, complex sources, etc.). In this study, the sources (seals and window)

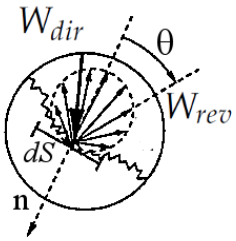

Figure 3.4: Diffuse reflection (Lambert's emission law)

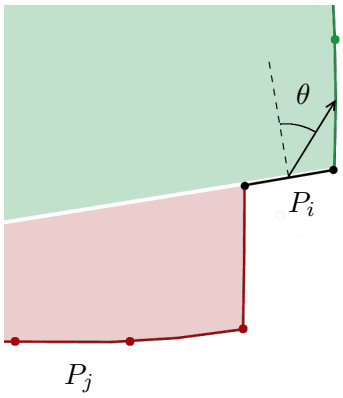

Figure 3.5: Self-obstruction

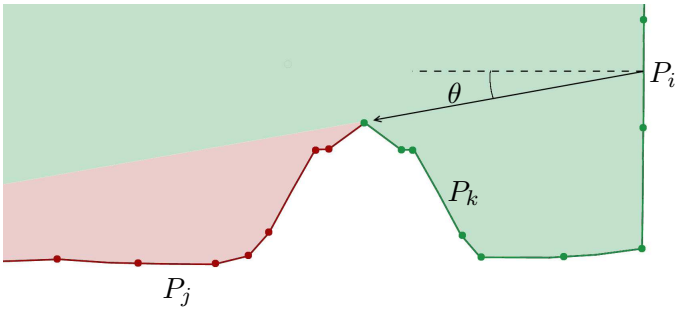

Figure 3.6: Obstruction to another element

have complex geometries, which in general implies very directive sound rays. Hence, an approach using a directivity other than Lambert's is necessary.

3.1.3 Visibility

One parameter that is found sometimes in the MES, and that we have not included in the equations in Section 3.1.1, is visibility. Matrix $\mathbf{T}$ describes the transmission of energy between element i and element j. However, it only takes into account the spatial location of each one of these elements, without accounting for the physical objects between the two that can obstruct this transmission. The same happens for matrix $\mathbf{Y^W}$ between P_i and the measure point M. There are 2 types of obstructionism:

- An element i is prevented from transmitting onto another element j by its own surface (Figure 3.5). A plane surface element can only radiate into an angle of 180°, with $\theta = [-90^o, 90^o]$. It cannot radiate backward through its own surface.
- An element i is prevented from transmitting onto another element j by a third element k. Figure 3.6 depicts this type of interference.

This obstruction is introduced in the equations by adding a visibility coefficient v_{ij}, with value equal to 1 when i and j can freely transmit energy one to another,

and 0 when the path between the two is hampered. This coefficient would multiply to equation 3.7 so that G in equations 3.16 to 3.18 becomes

$$G = v_{ij}\frac{1}{c}\frac{1}{r_{ij}} \tag{3.27}$$

3.2 Implementation of the improved MES and coupling with the Transmission Model

As we have explained earlier in this dissertation, the goal is to be able to calculate the sound level at any point of the interior vehicle cavity, with a fast model that allows its implementation into an optimization procedure. This is attempted by coupling the MES to the Transmission Models built in the previous chapters. However, we have seen that the basic MES only takes into account diffuse sources of noise. This is adequate for the secondary sources described in the previous section, because they are consequence of reflections into the cavity surface, which have a diffuse character. However, we can see in Figure 3.7 that the pressure distribution around the door seal is clearly directive.

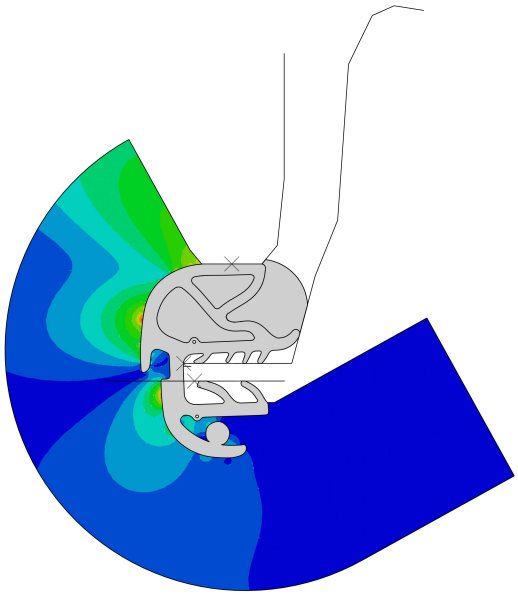

Figure 3.7: Pressure distribution caused by the excited seal at 7144Hz

Additionally, from the equations described in the previous section we can see that, in order to couple the Transmission Model with the MES, the power input of every element in the S_{out} of Figures 2.24, 2.27 and 2.34 must be inputted, adding dof to the MES model. Since the acoustic mesh is quite fine, and especially in the case of

big elements such as the window, these additional dof lead to bigger, slower models, which goes against the main goal of a light, fast model apt for optimization.

3.2.1 Directivity improvement: equivalent source

The solution for directivity that we propose solves all the previously mentioned problems. The goal is to reduce the information of all the elements in the S_{out} output surface of the Transmission Models, to a single point equivalent source with a directivity. This point source is situated inside a single element of fixed dimensions. That is, the entire seal or window is replaced by one single element, with one directivity function dependent on φ, as seen in Figure 3.9. The approximation of the directivity is achieved through the method used in [SBS15].

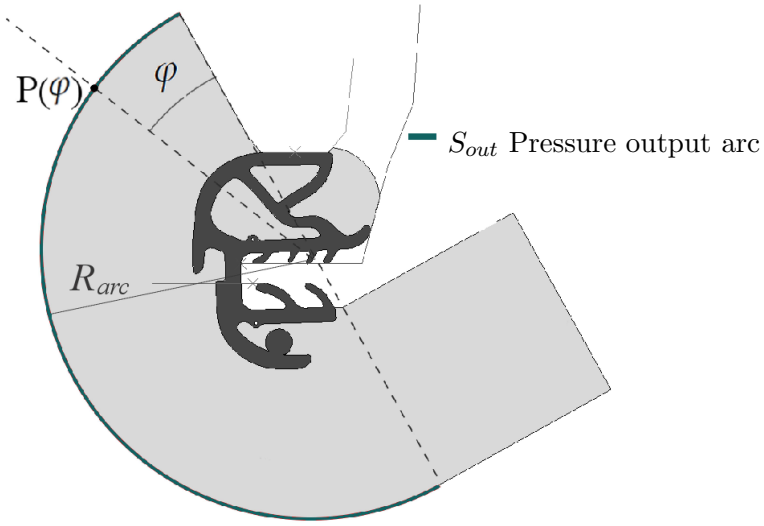

Figure 3.8: Pressure P(φ) is measured for all points in a half-circle of the Transmission Model boundary

The first step is to find the intensity $I(\varphi, b)$ for every point of the FE arc:

$$I(\varphi, b) = \frac{||P(\varphi, b)||^2}{\rho c} \tag{3.28}$$

Where b is the 1/3-Octave band for which directivity is calculated, P is the pressure and φ is the angle from the point where P is measured, through the center of the arc, to the superior extreme of the arc (see Figure 3.8).

Next, the direction for which the value of I is maximal is selected for every 1/3-Octave band

$$I_{max}(b) = I(\varphi_0, b) \tag{3.29}$$

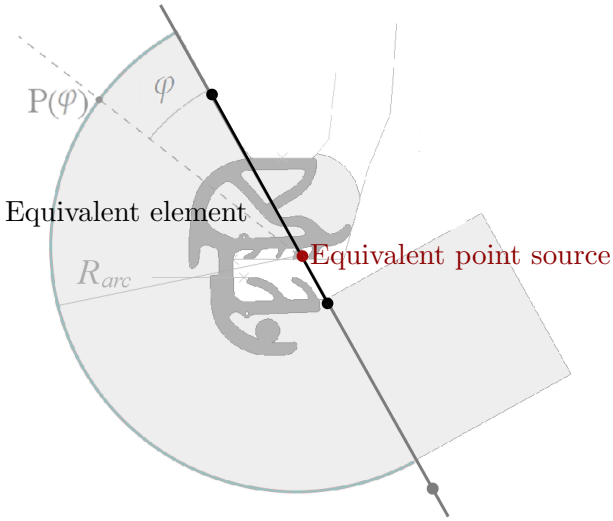

Figure 3.9: The seal is replaced by a single equivalent element with a point source with a specified directivity

Finally, the directivity function is found by normalizing the values of I over I_{max}

$$h(\varphi, b) = \frac{I(\varphi, b)}{I_{max}(b)} \tag{3.30}$$

This approach needs all pressure points to be at the same distance from the equivalent source, hence the pressure output arc must be a half-circle. In the situation where this is not the case, as in the window model in Figure 2.34, this approach must be modified. In such case, the equivalent source is placed at the median between the extremes of the arc. If we take d the distance between an extreme and the equivalent source, and $R_{arc}(\varphi)$ the distance between the latter and all other points in the arc, the Transmission Model pressure values can be used for the calculation of a new set of values, all at a distance d of the equivalent source, as depicted in Figure 3.10. The resulting intensity values are all at the same distance of the source and a directivity function h can thus be obtained. This is achieved by assuming the MES hypothesis which states that the sound pressure level decreases with distance from the source with a proportional value of $1/r$, thus the intensity decreases with $1/r^2$. Equation 3.31 becomes

$$h(\varphi, b) = \frac{R_{arc}(\varphi)^2}{d^2} \frac{I(\varphi, b)}{I_{max}(b)} \tag{3.31}$$

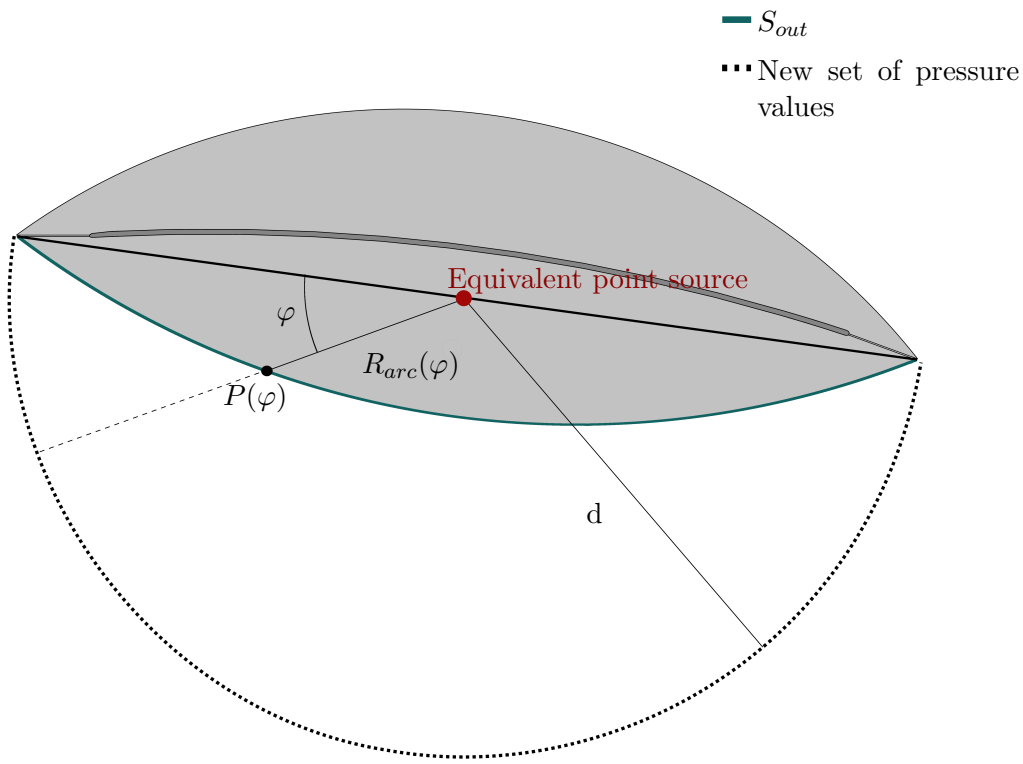

Figure 3.10: The window is replaced by a single equivalent element with a point source with a specified directivity

The number of FE pressure values in S_{out} is determined by the convergence of the FE Transmission Model. Therefore, the approach suggested in the original paper [SBS15], where the directivity is calculated from a polynomial fitting and the number of pressure values is minimized depending on the precision of the fit, has no interest in this study. Additionally, a fitting using all the directivity values in the arc causes high oscillations due to the Runge phenomenon. To solve this, we would need to choose only some points of the arc which would call for an optimization procedure, all resulting in a much more complicated and slower process. Instead, we have chosen a simple interpolation of values. This is, for this study, for any given angle the directivity, d_Φ is interpolated from the values of function h.

The schema in figure 3.11 summarizes the described procedure for the evaluation of the hybrid model.

The accuracy of the directivity function h is of course dependent on the accuracy of the Transmission Model. The bigger the meshed surface of the interior cavity,

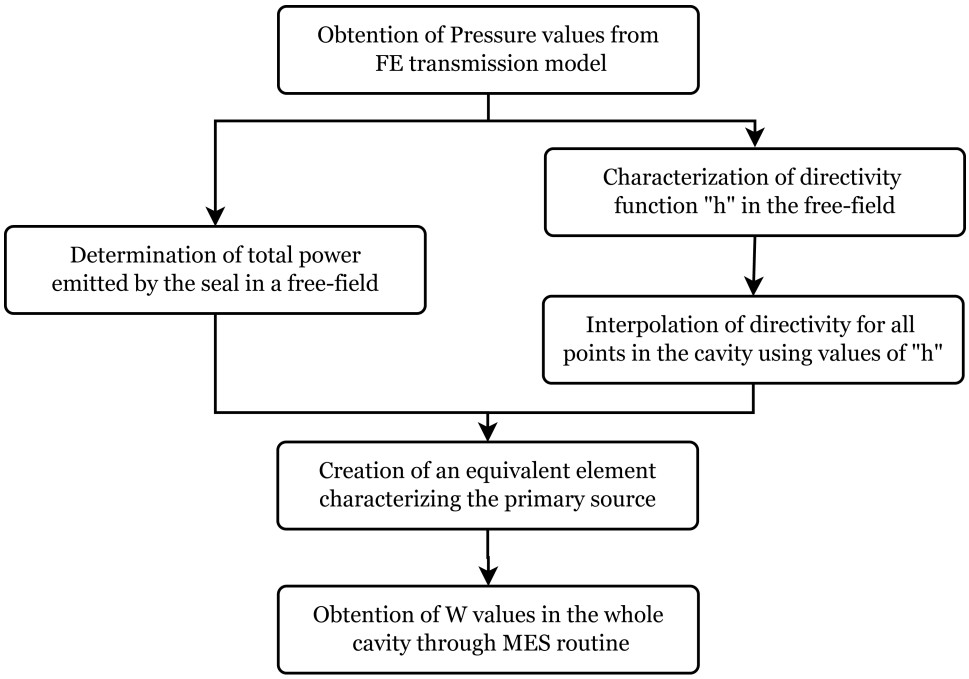

Figure 3.11: Schematics of the equivalent source method

the better. As a consequence, the radius of the interior cavity of the Transmission Models described in Chapter 2 might need to be modified to obtain the best accuracy in directivity.

3.2.2 Visibility solution

The visibility issues described in Section 3.1.3 can be avoided using a convex, 1-meter squared cavity. We have nevertheless formulated a solution for each one of the cases exposed in said section, which can be found in Appendix D. However, the second one of these solutions is difficult to implement computationally without providing much scientific interest to this dissertation. Additionally, if wrongly programmed, it can lead to a significant decrease of the model's simulation speed. We have thus decided to leave this programming work to a specialist and have chosen to test the MES in a simple, square (thus convex) vehicle cavity instead.

Figure 3.12 depicts the resulting square MES model.

3.2.3 Equivalent FE model

To validate this approach, we have compared the results of the door seal MES in Figure 3.8 with the equivalent, heavy, FE model depicted in Figure 3.12. Note that the used door seal Transmission Model doesn't correspond exactly to the one de-

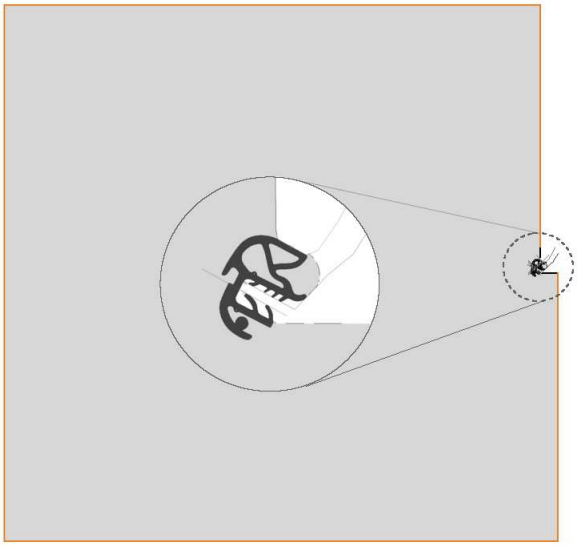

Figure 3.12: Whole cavity equivalent FE model. Infinite elements in orange

scribed in Chapter 2. The exact same methodology is used for its construction but the material parameters are different. Since the goal of this section is a comparative validation using the same seal parameters in a FE equivalent model, the accuracy of the Transmission Model used is irrelevant, as long as the models compared are built in the same way.

Given that the MES model for sound propagation in the cavity (from here on "the Propagation Model") already gives a good prediction on the reflection inside the square cavity, it is the direct field alone that is of interest. In consequence, only the direct fields of MES and equivalent FE models will be compared. This means that the exterior walls of the FE equivalent model are modeled as infinite, using the same infinite elements procedure described in chapter 2. Using the color code of Section 2.3.1, Figure 3.12 depicts these elements in the equivalent FE model.

3.3 Validation of the improved MES and comparison to an equivalent FE model

As stated previously, both the MES and the FE models are considered infinite cavities, and so infinite elements have been applied on several edges (marked in orange in Figures 2.24 and 3.12). However these elements don't work when they are really close to the excitation. We can observe in Figure 3.14.b that the power rays are curved near the right upper wall for some frequency bands. These same rays transform into a rectilinear trajectory when the cavity is expanded to the right so that the infinite

elements are not as near to the source. In consequence both the equivalent FE model and the Transmission Model might give distorted results near the right wall of the cavity.

As stated earlier in this dissertation, the radius of the arc where the directivity is calculated R_{arc} can have an impact on the accuracy of its prediction, especially if the source is complex. Because we know results to be inaccurate for extreme values of φ, convergence criteria for directivity will be evaluated on the inner values of the angles. Figure 3.13.a shows the different curves obtained for the calculation of directivity at different distances from the source. We can see that it converges for radius bigger than a certain one. In $R_{arc} = 40mm$ the main peak is shifted to the left, whereas for bigger values of R_{arc} the main peaks show the same tendency, but more to the right. Because the case shown combines the Propagation Model with a FE Transmission Model, the cost of the the calculation will be highly dependent on the chosen value of R_{arc}, and thus, a choice between accuracy and cost has to be made for each FE Transmission Model.

This is not the case however, for other methods where the improved MES can be applied. Indeed, the improved MES described in this chapter only needs a set of pressure values in R_{arc} as input, disregarding how these values were obtained. As a consequence, it can be used coupled with any method of obtainment of these values, whereas it is through a different Transmission Model using other numerical techniques such as BEM, or simply with the pressure values obtained from some microphones in an experimental excitation of the seal. For these cases, the pressure results can often be calculated at any radius, without a relevant increase of cost. In such situations, a radius as big as needed should be used.

In Figure 3.14 we show the comparison between the MES with converged directivity and the equivalent FE model, for the direct field in a band between 3564 and 4490Hz. Given the good correlation between the two, we can assume that the method will give good results with MES directivity extracted in a sufficiently large R_{arc}. If however we cannot attain the converged radius for model size reasons, like in our specific FE case, we consider that a small, non-converged radius (in this case of 40mm) is also sufficient for our needs (Figures 3.13.b and 3.15). This is a very good assumption in the case studied here, since the accuracy problems are mainly found near the walls around the tested element, and not in the middle of the cavity where the passengers, and hence our values of interest, are placed.

In any case, the characterization of the equivalent source and its directivity need to be done only once for each type of excitation and each set of seal parameters, hence any optimization of cavity dimensions, absorption coefficients, etc. can be achieved rapidly after the first costly directivity determination.

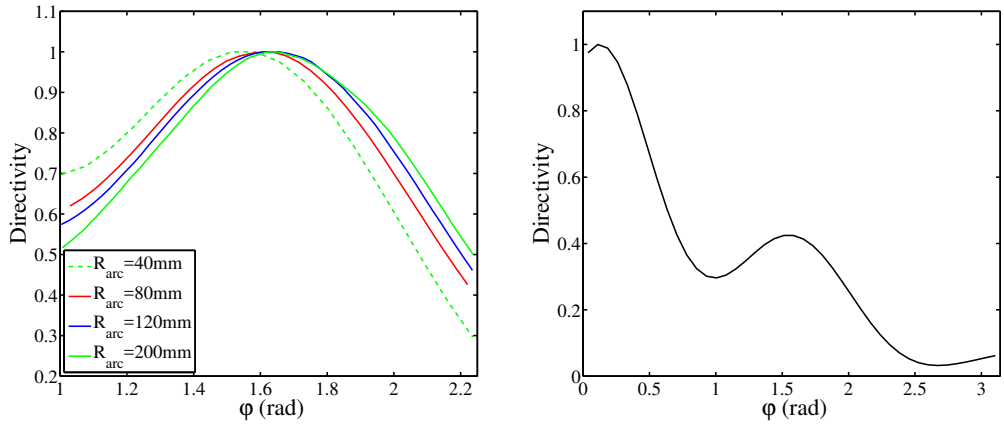

a) b)

Figure 3.13: Directivity values for frequency band between 3564 and 4490Hz. a)Directivity comparison for different values of R_{arc}. b)Directivity for $R_{arc} = 40$ for $\varphi = [0, \pi]$

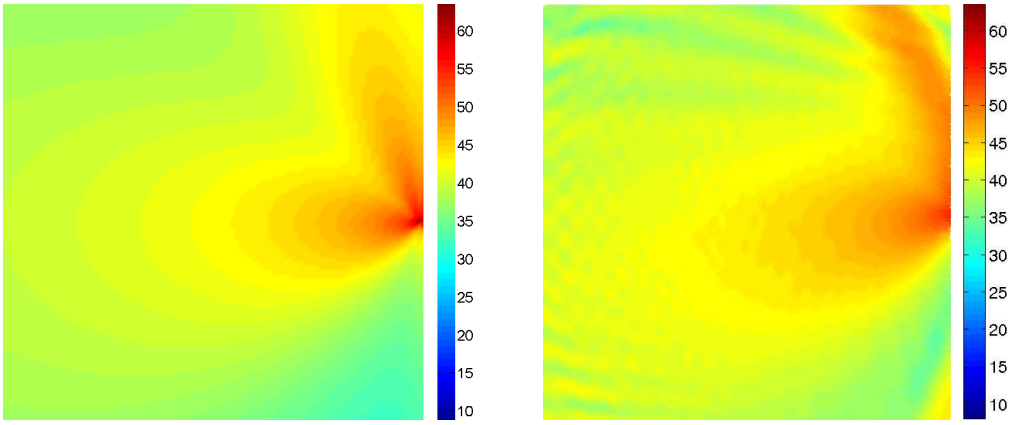

a) MES with converged R_{arc} b) Equivalent FE model.

Figure 3.14: Comparison of MES with converged $R_{arc} = 1200mm$ against FE equivalent model for frequency band 3564-4490Hz. Values are in dB of W

Model	Obtainment of necessary pressure points	Directivity determination	Determination of W for whole cavity	**Total time**
Complex FE	10851 s (3h)	–	1925 s	**12776 s (3.5h)**
FE+MES	357 s	15.2 s	16.2 s	**388.36 s**

Table 3.1: Time comparison for both approaches. All calculations have been achieved through a system of 32 CPU and 264Go of RAM

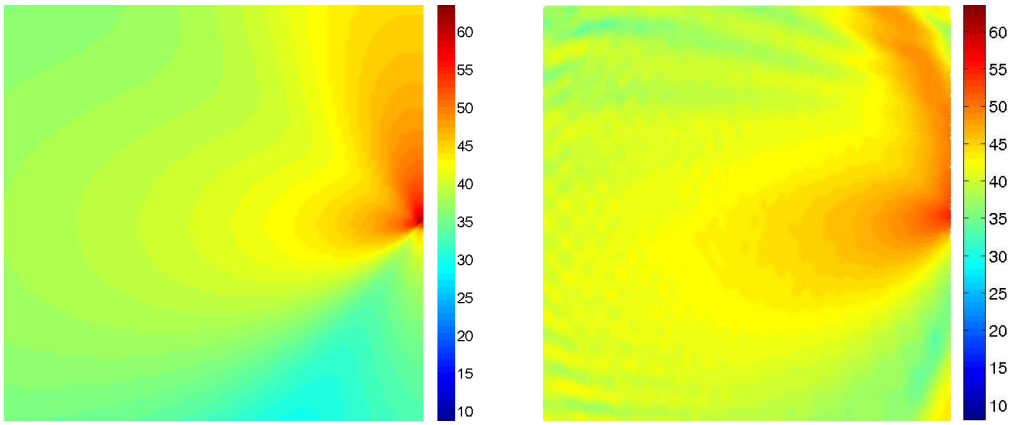

a)MES with small R_{arc} b)Equivalent FE model.

Figure 3.15: Comparison of MES with small $R_{arc} = 40mm$ against FE equivalent model for frequency band 3564-4490Hz. Values are in dB of W

Table 3.1 compares the calculation times for both approaches to simulate the energy distribution of the whole cavity. We can appreciate that the time is already greatly reduced if the hybrid model proposed here is chosen over a FE modeling. Moreover, if we only need information on one single point, the total time for the FE+MES method is reduced to 372.16s. The times for the transformation pressure results into W are of course dependent on the used programming techniques and software (MATLAB in our case), and could be improved. However, we can already see that it is the obtainment of necessary pressure points (obtained through ABAQUS) that will represent the larges proportion of the simulation time. Since the mesh in the FE entire cavity model is much larger than that of the FE Transmission model, the simulation of the former will always be much heavier.

Additionally we have validated the pertinence of choosing a more accurate directivity than the lambertian. This is depicted in Figure 3.16, where the MES results show how this type of directivity fails to accurately represent the real directivity shown in 3.16.b.

3.4 MES application to the studied elements and excitation influence

Once the methodology of the improved MES has been validated, the resulting Total Model can be applied to the different elements studied in this dissertation. For all these elements, two different excitations have been applied (single wave and diffuse field), and the resulting sound pressure levels (L_p) compared. For each case, the equivalent source is placed at the center of the right wall of a square cavity, and the

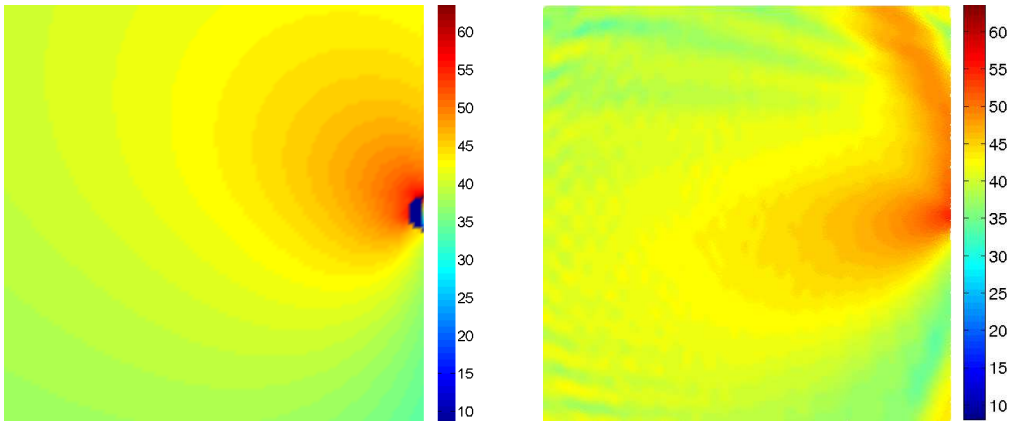

a)MES with converged R_{arc} b)Equivalent FE model.

Figure 3.16: Comparison of MES with small $R_{arc} = 40mm$ and lambertian directivity against FE equivalent model for frequency band 3564-4490Hz. Values are in dB of W

pressure level is calculated in a point 20 cm away, more or less the distance between the seals and the passenger's ear in a car. The amplitude of the excitation is always of 10Pa, which is the equivalent of a busy road. This value is only chosen as a reference, since this work is centered only around noise of aerodynamic nature.

3.4.1 Door seal MES

The pressure level results for the door seal are plotted in Figure 3.17. We can see that the curves are fairly robust to different excitations. We observe that the frequencies going from 800 to 6000Hz are the most noisy, and a frequency around 2000Hz for which a peak of noise appears, which should be carefully studied in the noise-reducing conception of the seal. Figure 3.18 shows the whole cavity MES for the frequency third-octave band ranging from 7079 to 8913 Hz with a diffuse field excitation.

3.4.2 Window seal MES

The same curves have been plotted for the window seals (Figures 3.19 and 3.20). Again, we observe close to no differences between the values of the curves for the different excitations. In this case, the most delicate frequencies go from 1500 to 3000Hz, with a delicate point around 2000Hz where the pressure level rises importantly. However, we see that the noise levels are very low. This is explained by the way the Transmission Model in Section 2.3.3 is built. Seen that the window is considered fix, so that its participation is not accounted for in the model, and that the part of the seal inserted in the frame is also fixed, there is only a small portion of the seal allowed for movement, which could be the cause of the low transmission onto the other side. This means that the most important contribution of this seal on sound

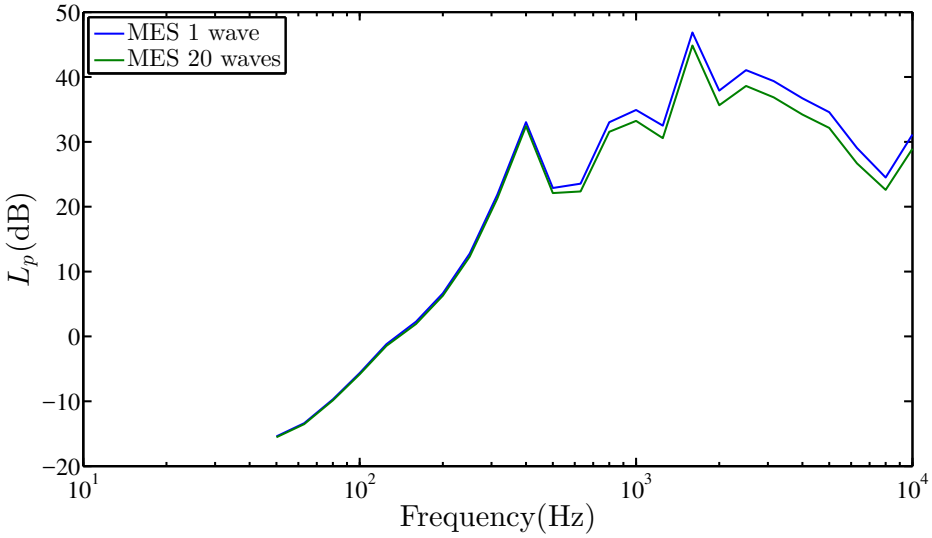

Figure 3.17: L_p for a point 20 cm away from the door seal, obtained through the improved MES

transmission is through its part in the boundary conditions of the window. Again, Figure 3.20 shows the SPL distribution in the case of a diffuse field for the window seal. As it has been repeated throughout this dissertation, all these results are based on the approximation of the material properties of the window seals made in Chapter 1, so any conclusions derived from this study assume this approximation is correct. Hence, it is possible that the fact that the noise transmitted through window seals is so low is due to an incorrect material characterization.

3.4.3 Window MES

In the case of windows, we can see in Figure 3.21 that the type of excitation is more relevant than in the previous two cases, especially for high frequencies. In the aerodynamic range (400-1000Hz) we can observe a first important L_p peak around 700Hz, and another, lower but highly influenced by the type of excitation, around 7000Hz. The SPL distributions with a diffuse excitation is shown in Figure 3.22.

Because the goal of this dissertation is not to model the transmission of the window but to observe the influence of the stiffness and damping of the window-seals, a small influence study of these parameters can be found in Figures 3.23 and 3.24. Here we can see the MES results for L_p when the window is excited with one single wave. Stiffness and damping (respectively k and c) have been modified to approximately ten times and a tenth of the values obtained in Section 2.3.3. Observing said figures we can see that both stiffness and damping can play an important role in the noise transmitted into the interior of the vehicle cavity. However, the former seems to affect

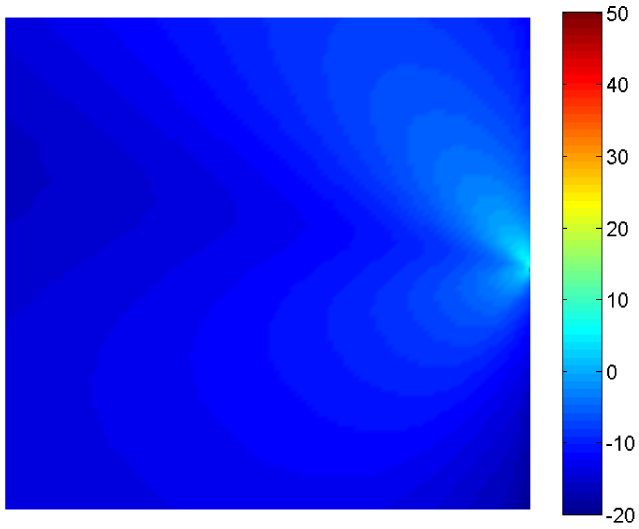

Figure 3.18: Whole cavity L_p distribution for door seal radiation, plotted using improved MES. Values are in dB of W

mainly low to mid frequencies, whereas the latter appears to be more influential for high pitched noises. We can see that a less stiff seal could reduce the transmitted noise at its maximal peak, whilst a less damped seal material would introduce several peaks of L_p.

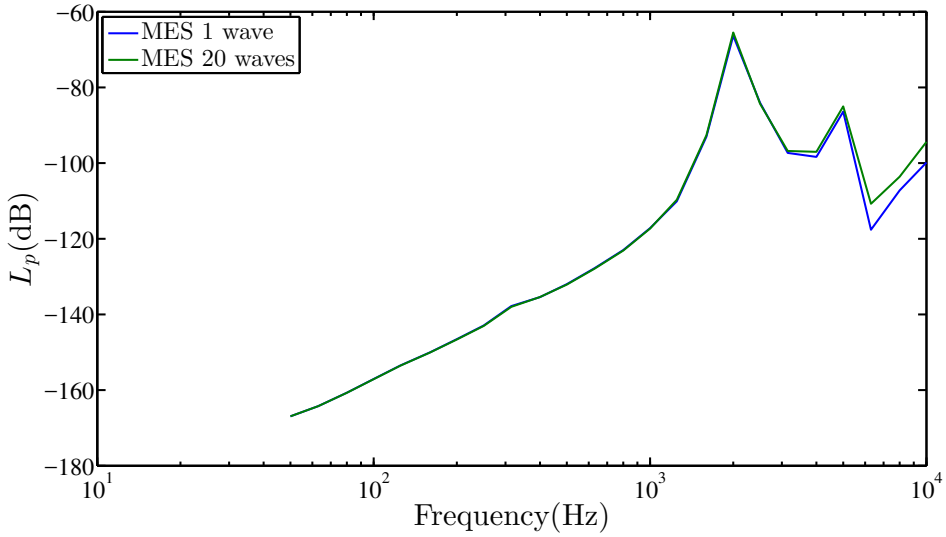

Figure 3.19: L_p for a point 20 cm away from the window seal, obtained through the improved MES

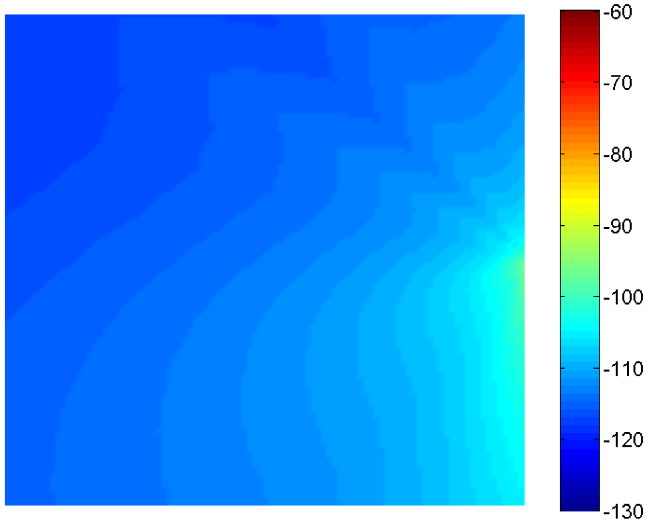

Figure 3.20: Whole cavity L_p distribution for window seal radiation, plotted using improved MES. Values are in dB of W

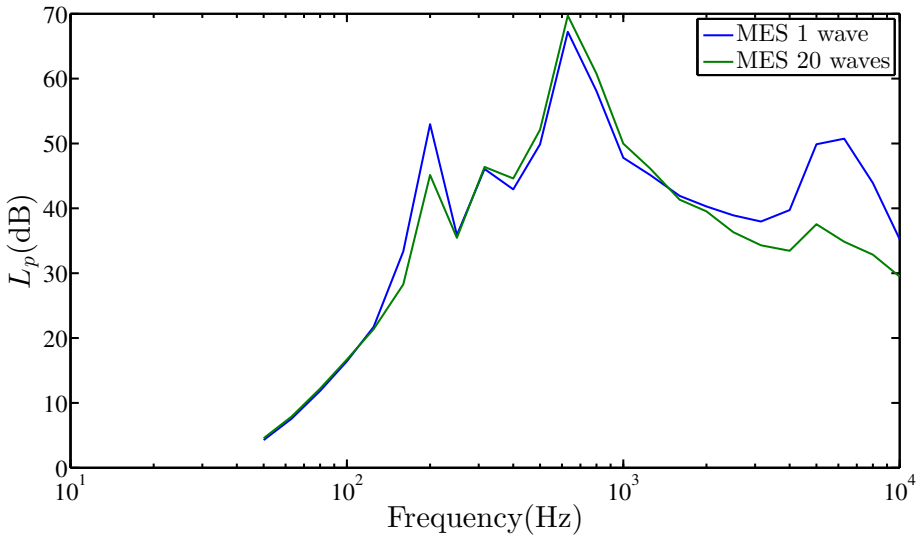

Figure 3.21: L_p for a point 20 cm away from the window, obtained through the improved MES

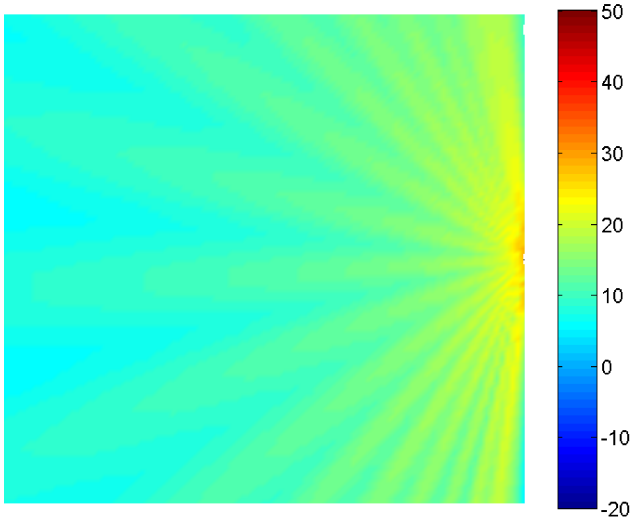

Figure 3.22: Whole cavity L_p distribution for window radiation, plotted using improved MES. Values are in dB of W

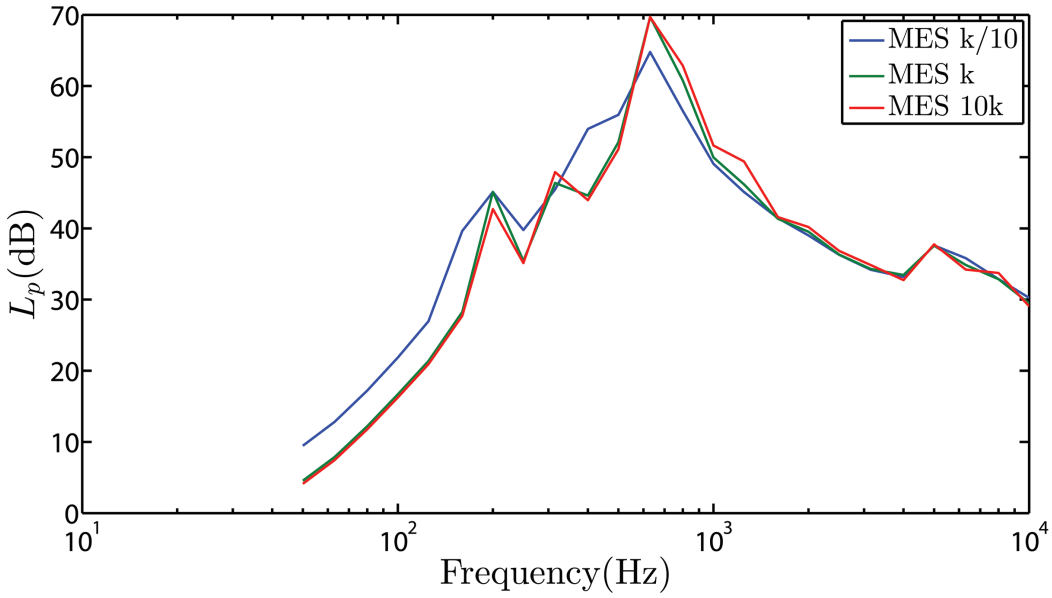

Figure 3.23: L_p curves for a single wave, with different equivalent stiffness parameters for the window model

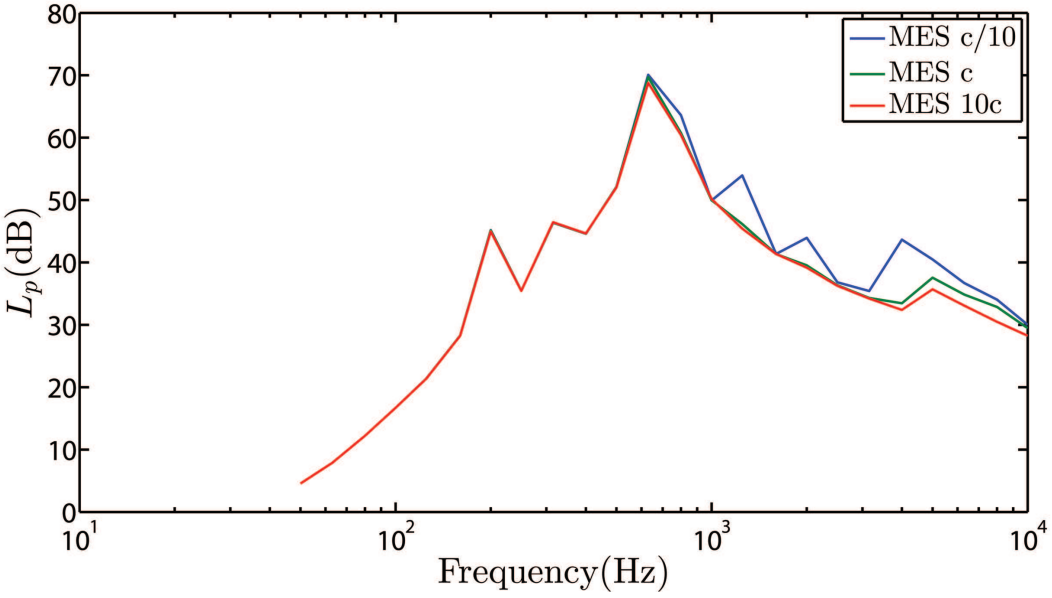

Figure 3.24: L_p curves for a single wave, with different equivalent damping parameters for the window model

3.5 Conclusions

In this chapter we have introduced a propagation model, capable of predicting the sound power level at any point inside a cavity in which the elements described in chapter 2 radiate. This is achieved through the use of the MES (Méthode Énergétique Simplifiée), a frequency-averaged energy modeling method, based on the well-known Statistical Energy Analysis. This method has the characteristic of being able to predict the SPL locally at any point of the cavity, with the need only of a coarse surface mesh of its walls, which leads to simulation times of the order of one thirtieth smaller than if the same case were simulated using FE in the entire cavity.

This Propagation Model can be coupled to the Transmission Models detailed in chapter 2, allowing the completion of the modeling of the entire sound transmission path, from the exterior of the car to passenger's ear. This way the big vehicle cavity can be modeled with a fast method, whereas the small, complex geometry of the radiating elements can be simulated with the more convenient FE mesh.

However, the MES in the bibliography has some limitations, especially when it comes to near fields and directive sources. Given that both types of seals are very directive, the MES would not be accurate for this study. In consequence, an improvement of the way the directivity is taken into account in the MES is proposed, and the results are validated through comparison with a much slower FE model of the entire cavity+door-seal geometry. Additionally, the MES Propagation Model can be built from any set of pressure values, regardless of how these values were obtained. That is, the SPL in the entire cavity can be plotted using only a few experimentally-obtained pressure values as input, or by coupling the Propagation Model with a different Transmission Model, using, for example, BEM.

To conclude, the improved MES, coupled with the Transmission Model, is applied to the three elements in study (door seals, window seals and windows), and the results commented. Additionally, the method, together with the simplified Window Transmission Model detailed in chapter 2, has allowed a fast influence study of the impact of the window seal's dynamic properties on the resulting noise transmitted through the windows.

3.6 Expansions

The MES detailed in this chapter has been applied to a square, simple cavity. The first expansion that we foresee doing for the improved MES is hence its application to a more complex cavity, with geometry similar to the one we could find in the interior of the vehicle. However, in such a cavity, we would probably find several visibility issues, such as the ones described in Section 3.1.3, due to the complex geometry and to the addition of interfering elements, mainly the car's seats. The programming

of the procedure described in Appendix D, for the implementation of the visibility coefficient in equation 3.27 would thus be necessary. Given that this model has been conceived for an optimization purpose, the programming should be carefully developed to add minimal time cost to the simulation.

The comparison with the FE equivalent model leads us to believe that the MES is accurate enough for our specific door seal. Nevertheless, for other complex sources, the directivity might not be radial, and its decay with the distance from the source might not be of $1/r$ as approximated with the Green function, but can be dependent on the angle. This can be observed in Figure 3.13.a, where the directivity diverges slightly at different distances from the source. This divergence could be amplified for other radiating elements. As a future perspective this dependence could be introduced in the directivity determination by interpolating the curves of that appear in the referenced figure.

Finally, the methodology described in this chapter has been validated through comparison with a FE equivalent model. However, a comparison with some experimental tests is necessary to endorse these results.

3.7 Bibliography

[BB95a] O. M. Bouthier and R. J. Bernhard. Simple models of energy flow in vibrating membranes. *Journal of Sound and Vibration*, 182(1):129–147, April 1995.

[BB95b] O. M. Bouthier and R. J. Bernhard. Simple models of the energetics of transversely vibrating plates. *Journal of Sound and Vibration*, 182(1):149–164, April 1995.

[BIJ03] A. Bocquillet, M. N. Ichchou, and L. Jézéquel, L. Energetics of axisymmetric fluid-filled pipes up to high frequencies. *Journal of Fluids and Structures*, 17(4):491–510, March 2003.

[BIJ10] S. Besset, M.N Ichchou, and Louis Jézéquel. A coupled BEM and energy flow method for mid-high frequency internal acoustic. *Journal of Computational Acoustics*, 18(1):69–85, 2010.

[CLJ02] V. Cotoni, A. Le Bot, and L. Jézéquel. High-frequency radiation of l-shaped plates by a local energy flow approach. *Journal of Sound and Vibration*, 250(3):431–444, February 2002.

[Cot01] V. Cotoni. *Modélisation de phénomenes vibroacoustiques en moyennes et hautes fréquences par méthode énergétique locale.* PhD thesis, Ecole Centrale de Lyon, 2001.

[Har05] P. Hardy. *Méthodes énergétiques simplifiées en moyennes et hautes fréquences: Théorie et applications industrielles*. PhD thesis, Ecole Centrale de Lyon, 2005.

[HIJ05] L. Houillon, M. N. Ichchou, and L. Jézéquel. Wave motion in thin-walled structures. *Journal of Sound and Vibration*, 281(3–5):483–507, March 2005.

[ILJ97] M. N. Ichchou, A. Le Bot, and L. Jézéquel. Energy models of one-dimensional, multi-propagative systems. *Journal of Sound and Vibration*, 201(5):535–554, April 1997.

[Lan95] R. S. Langley. On the vibrational conductivity approach to high frequency dynamics for two-dimensional structural components. *Journal of Sound and Vibration*, 182(4):637–657, May 1995.

[Le 95] A. Le Bot. *Équations énergétiques en mécanique vibratoire: applications au domaine des moyennes et hautes fréquences*. PhD thesis, École Centrale de Lyon, 1995.

[LIJ96] Y. Lase, M. N. Ichchou, and L. Jézéquel. Energy flow analysis of bars and beams: theoretical formulations. *Journal of Sound and Vibration*, 192(1):281–305, April 1996.

[Lyo03] R.H. Lyon. *Statistical Energy Analysis of Dynamical Systems: Theory and Applications*. MIT Press, February 2003.

[Mor98] P. Moron. *Mise en oeuvre de méthodes énergétiques dans l'étude du comportement vibratoire de structures complexes dans le domaine des moyennes et des hautes fréquences*. PhD thesis, Ecole Centrale de Lyon, 1998.

[NS89] D. J. Nefske and S. H. Sung. Power Flow Finite Element Analysis of Dynamic Systems: Basic Theory and Application to Beams. *Journal of Vibration, Acoustics, Stress, and Reliability in Design*, 111(1):94–100, January 1989.

[SBS15] K. Soobbarayen, S. Besset, and J-. J. Sinou. A simplified approach for the calculation of acoustic emission in the case of friction-induced noise and vibration. *Mechanical Systems and Signal Processing*, 50–51:732–756, January 2015.

[Sch04] T. Schmitt. *Modélisation des transferts acoustiques en moyennes et hautes fréquences par méthode énergétique: Application à l'encapsulage des compartiments moteurs*. PhD thesis, Ecole Centrale de Lyon, 2004.

[WB92] J. C. Wohlever and R. J. Bernhard. Mechanical energy flow models of rods and beams. *Journal of Sound and Vibration*, 153(1):1–19, February 1992.

[WVW04] A. Wang, N. Vlahopoulos, and K. Wu. Development of an energy boundary element formulation for computing high-frequency sound radiation from incoherent intensity boundary conditions. *Journal of Sound and Vibration*, 278(1–2):413–436, November 2004.

General Conclusions and Expansions

Conclusions

The goal of this study was the creation of a car door and window seal model, accurate but fast enough for its implementation into a sound reduction optimization procedure, specifically conceived to be simulated under aerodynamic excitations (400-10000Hz). For this, a hybrid model has been built, capable of taking into account the complex geometry of the studied elements and their material non-linearities, all while being sufficiently fast for an optimization in the required mid-high frequency range. The first part of this hybrid model comprises the modeling of the seals themselves, to predict their sound transmission capacity. We have called this the Transmission Model. This part evaluates also the window seal behavior when acting as a boundary condition of the windows, another crucial element in exterior sound reduction in vehicles. The second part propagates the transmitted sound from the previous model into the cavity, allowing determining the sound level at any point, for example, at the passenger's ear. This is the Propagation Model, and it allows taking into account the other surrounding elements inside the cavity, for a more accurate evaluation of passenger acoustic comfort. Additionally, some influence studies have been made to evaluate possible parameters prone to be taken into account in the subsequent optimization.

The first and second chapters describe the methodology to the construction of the Transmission Model. Given the static step through which the seals have to go before the aerodynamic excitation (insertion into the frame and door closure), this model has to be divided into two sections. In the first, which corresponds to the first chapter, the static behavior of the seals is modeled. In the second chapter the dynamic material properties are introduced, and the elements are subject to an acoustical excitation. This part of the work is modeled through finite element software ABAQUS, upon request of the implicated company PSA Groupe.

The Static Model needs the characterization of the non-linear rubbers used in the fabrication of the door seals. The Neo-Hookean law is chosen among all available hyperelastic models in ABAQUS, through the software's material-evaluating tool. This choice, as well as the resulting static model of the door seal, are validated through some experimental tests. In these, both the deformation and stress field are ratified, however, an unpredictable seal rotation unaccounted for in the numerical model is exposed, and it is decided that it should be considered as a source of uncertainty. The same scheme is applied to the window seals. To end the chapter, the static influence of door geometry, friction, and level of pre-compression are evaluated, all three found

to have a certain impact on the resulting stress distribution.

Chapter 2 introduces the Dynamic Transmission Model. For this, the pre-deformed and pre-stressed window and door seals, resulting from the previous chapter, are linearized around the pre-deformed state, thus their dynamic material properties must be implemented. Due to the lack of some viscoelastic parameters of the door seal, an experiment has been designed to define these values. The resulting seals are then excited with different acoustic excitations, and their Transmission Loss curves commented. In this chapter, the windows are introduced as a modeled element in a third Transmission Model. Given their coupling with the boundary condition behavior of the window seals, the latter must be introduced someway in this model. To simplify what would be a very costly window+window-seal model, the window seals are replaced by an equivalent spring-damper element, allowing the evaluation of the ensemble's TL through a much lighter simulation. Finally, we have attempted to validate the modeling methodology through comparison with an experimental acoustic test on the door seal. However, the results, although allowing certain deductions, are inconclusive due to lack of the appropriate experimental means.

The third and final chapter describes the Propagation Model to be coupled with the results of the three Transmission Models in the previous chapter. This is accomplished using the existing MES (Méthode Énergétique Simplifiée) method in its integral form. The MES is a frequency-averaged energy method, allowing calculating the Sound Power Level at any point of a cavity, in a fast manner and with only a coarse surface mesh of its exterior boundary. The limitations of this method yield it inaccurate for complex, directive sources such as the ones studied in this dissertation. In consequence, an improvement, allowing a better implementation of the correct directivity of the seals, is proposed here. The resulting improved MES is tested against an equivalent FE element method, and the comparison shows an important reduction of time using the energy method, while maintaining a correct accuracy. Finally, the MES is coupled to the three Transmission Models, and subjected to different excitations and, in the case of the window model, different seal-replacing boundary conditions. The results indicate a small sensibility of both seals to the type of excitation and prove the important role of window seals on the windows' noise-transmitting capacity.

All in all we have provided a simple model, capable of predicting the entire sound path between the exterior of a vehicle and the passenger's ear. Additionally, some studies have identified several parameters that could be influential on the final output of this path, to be considered in a future optimization. However, the seals' main function is not that of an acoustical barrier but has more of a water-proof purpose. The fact that this purpose could also be affected by the identified influential parameters leads to several impediments in their modification, which would bound the optimization and need to be taken into account.

Expansions

The hybrid model obtained from the study described in this dissertation is conceived to be used for the attainment of the optimal noise-reducing door and window seals, when subject to aerodynamic excitations. However, neither the optimization nor the simulation of the model under this specific excitation have been implemented. Hence, we consider these two factors to be the main work to be carried out in the future. On this matter, a choice on the parameters having an important impact on the sound transmitted through each element should be made. Some of these parameters, such as window seal stiffness and damping have already been found influential, and should hence be included to be modified for the determination of the optimal window seal. Other parameters, such as the level of pre-compression of the door seal, have only been found to be significant in the final stress distribution of the Static Model, but are considered very likely to be of major importance in the Dynamic Transmission Model as well. An influence study should hence be carried out over these parameters for the latter, before the optimization procedure. One of these parameters is the geometry of the seal. However, a complete geometry optimization is hard to implement and would need a separate thorough study. In consequence, we recommend that the geometry is taken into account in the influence studies and the optimization by small modifications, such as the thickness of the material or number of inside cavities, in a similar way to what has been done for its influence on the Static Model in Chapter 1.

Before this optimization, however, we find that there are several aspects that should be either more thoroughly validated, or improved in the model described here. Some of them have been explained in the Expansions sections at the end of each chapter. These comprise the re-evaluation of the material properties that where not supplied by the providers, for their characterization in a more standardized and accurate test. A study of the influence of these material uncertainties, or any other parameters for which the real values could differ from those explained throughout this dissertation, could also be of interest. We would also like to include the experimental validation of both the MES and the Transmission Model, for which the accuracy of the tests described in this dissertation has been found to be insufficient. However, we would like to highlight two future possible expansions for the model that we consider to be the most interesting.

The first one regards the actual improved MES model, which has only been applied to a simple square cavity. To be of use in the industrial field, this method should be applicable to any vehicle's interior geometry. However, due to the lack of a visibility coefficient allowing taking into account non-convex geometries and interior obstacles such as car seats, this application is not yet possible. However, the theory for the implementation of this coefficient has already been formulated and explained in Appendix D. The only remaining step is its programming into the improved MES script. This is thus an expansion that could be applied easily at short-term.

The second suggested expansion refers to an enlargement of the actual model, to better represent the effect of the entire extruded seal on the sound level in the interior of the vehicle cavity. For the modeling scheme described in this dissertation, some simplifications have been made. For starters, only a vertical compression of the door seal when the door is closed is taken into account. However, this is not the case for the sections of door seal near the hinge. Additionally, for a faster, simplified model, we have only considered a 2D section. Due to the fact that the seal is extruded in a loop, some sections have a participation different than others, either because of its position (they can be upside down in the lower part of the door frame, or sideways in the hinge), or the different mentioned compression trajectories. Hence a 2D model cannot predict the full participation of the entire extruded seal. The inclusion of these two factors would lead to several improvements. To begin with, the implementation of the compression trajectory on the Transmission Model could ameliorate the choice of the optimal seal. We could consider the sound reduction capacity of each type of compressed section as criteria for the optimization, and give them weighting coefficients depending on the length of the portion of the extruded real seal where each particular type of compression is found. This way, we would assure that the chosen seals are optimal throughout the entire seal extrusion. Additionally, a 3D simplified model could be built by extruding the results of several 2D models with the different possible compressions and positions, and introducing them in a 3D MES cavity model. This would lead to a model that, although too heavy to be used in an optimization, would be capable of predicting the sound level inside the entire 3D vehicle cavity in a fast and accurate manner.

Appendix A

Dynamic material data for the compressible and incompressible rubbers

The dynamic characterization given by the providers is only available for the incompressible rubber. The results of the experimental tests are shown in Figure A.1

Frequency	E	tgδ
628	3,84231	1,53E-01
661	3,928219	1,38E-01
694	3,9706	1,57E-01
728	3,776038	1,46E-01
760	3,845549	1,37E-01
793	3,828181	1,40E-01
827	3,820265	1,42E-01
860	3,844847	1,43E-01
893	3,863936	1,42E-01
926	3,89036	1,43E-01
959	3,911574	1,42E-01
992	3,938562	1,43E-01
1025	3,951353	1,40E-01
1058	3,96799	1,44E-01
1091	3,972843	1,43E-01
1124	3,991862	1,45E-01
1157	3,99944	1,45E-01
1190	4,019607	1,47E-01
1223	4,028597	1,48E-01
1255	4,036499	1,47E-01
1289	4,047696	1,46E-01
1321	4,055866	1,48E-01
1356	4,060829	1,50E-01
1389	4,046759	1,51E-01
1420	4,073408	1,51E-01
1454	4,067864	1,52E-01
1488	4,077096	1,55E-01
1521	4,057581	1,59E-01
1555	4,045751	1,60E-01
1586	4,08609	1,55E-01
1619	4,09193	1,59E-01
1653	4,103769	1,58E-01
1685	4,094353	1,59E-01
1717	4,125884	1,58E-01
1751	4,111198	1,60E-01
1786	4,094705	1,61E-01

Frequency	E	tgδ
1751	4,98E+00	0,1406237
1786	5,00E+00	0,149412
1817	5,00E+00	0,14423
1849	5,05E+00	0,1461843
1882	5,03E+00	0,1518721
1917	4,98E+00	0,1447644
1953		
1984	5,06E+00	0,1498722
2016	5,10E+00	0,14796
2049	5,10E+00	0,143457
2083	5,11E+00	0,1474586
2119	5,05E+00	0,1567879
2148	5,04E+00	0,1568409
2185	5,06E+00	0,1662526
2216	5,07E+00	0,1509126
2248	5,04E+00	0,1558139
2281		
2315	4,98E+00	0,1654905
2350	5,03E+00	0,1398958
2386	5,01E+00	0,1662597
2413	5,06E+00	0,1432119
2451	5,03E+00	0,1650091
2480	5,07E+00	0,1580985
2510	5,08E+00	0,1584228
2551	5,14E+00	0,1595954
2583	5,07E+00	0,1456521
2615	5,14E+00	0,1462712
2648	5,14E+00	0,1499156
2682	5,09E+00	0,1584007
2717	5,13E+00	0,1662727
2741	5,10E+00	0,1701974
2778	5,08E+00	0,1650837
2815	5,08E+00	0,1637589
2841	5,05E+00	0,162317
2880	5,06E+00	0,1663771

Frequency	E	tgδ
2907	5,01E+00	0,1648284
2948	5,07E+00	0,168541
2976	5,06E+00	0,174676
3005	5,07E+00	0,1651656
3049	5,07E+00	0,1684772
3079	5,06E+00	0,1670636
3109	5,10E+00	0,1735259
3141	5,06E+00	0,1753488
3173	5,07E+00	0,1690597
3205	5,13E+00	0,178245
3238	5,05E+00	0,1800059
3272	5,04E+00	0,1778426
3307	5,01E+00	0,1719167
3342	5,11E+00	0,1838624
3378	5,10E+00	0,1777665
3415	5,10E+00	0,196928
3434	5,13E+00	0,1912996
3472	5,12E+00	0,1827701
3511	5,09E+00	0,2010062
3551	5,16E+00	0,2010835
3571	5,15E+00	0,1815323
3613	5,13E+00	0,1826489
3634	5,07E+00	0,1806094
3676	5,09E+00	0,1874944
3698	5,09E+00	0,1847676
3742	5,07E+00	0,1824484
3765		
3811	4,97E+00	0,1760241
3834	5,05E+00	0,1900693
3882		
3906	5,03E+00	0,2018307
3931	5,05E+00	0,1949158
3981	5,06E+00	0,2157452
4006	5,08E+00	0,2072213
4032	5,08E+00	0,2074175

Frequency	E	tgδ
4085	5,05E+00	0,2130032
4112	5,06E+00	0,2022749
4139	5,10E+00	0,2043744
4167	5,02E+00	0,1911399
4195	5,11E+00	0,1925225
4252	5,06E+00	0,176528
4281		
4310	5,14E+00	0,1746489
4340	5,18E+00	0,1720134
4371	5,01E+00	0,1793125
4401	5,06E+00	0,1754543
4433	4,98E+00	0,1884033
4464	5,04E+00	0,1860243
4496	4,95E+00	0,2081669
4529	4,96E+00	0,2661164
4562	5,02E+00	0,2626835
4596	5,15E+00	0,2301792
4630	5,13E+00	0,1926735
4664	5,23E+00	0,1967932
4699	5,18E+00	0,1866254
4735	4,86E+00	0,1779036
4771	4,99E+00	0,1779348
4808		
4845	4,96E+00	0,1824147
4883	4,82E+00	0,1890984
4921	4,99E+00	0,1847146
4960	5,00E+00	0,1893553
5000	5,01E+00	0,1933587
5040	4,96E+00	0,1887732
5081	4,99E+00	0,1866922
5123	4,83E+00	0,1903512
5165		
5208		
5252	4,97E+00	0,2053119
5297		

Frequency	E	tgδ
5342	4,83E+00	0,2073977
5388	4,82E+00	0,2155165
5435	4,83E+00	0,2132263
5482	4,96E+00	0,2221201
5531	4,88E+00	0,225991
5580	4,96E+00	0,2255897
5631	4,80E+00	0,2335785
5682	4,78E+00	0,2333101
5734	4,82E+00	0,2152003
5787	4,97E+00	0,214531
5841	4,85E+00	0,2261986
5896	4,94E+00	0,2285616
5952	4,84E+00	0,228442
6010	4,73E+00	0,2435864
6068	4,83E+00	0,2318918
6127	4,88E+00	0,2302301
6188	4,82E+00	0,2518149
6250	4,78E+00	0,2485492
6313	4,89E+00	0,2420984
6378		
6443	4,60E+00	0,2687003
6510	4,82E+00	0,2674346
6579	4,65E+00	0,301656
6649	4,69E+00	0,2815978
6720	4,79E+00	0,2819621
6794	4,91E+00	0,2675216
6868	4,74E+00	0,2764311
6944	4,74E+00	0,312409
7022	4,58E+00	0,3267607
7102	4,97E+00	0,2975932
7184	4,85E+00	0,3722895
7267	4,77E+00	0,3572621
7353		
7440	5,32E+00	0,3359476
7530		

Figure A.1: Dynamic material data for incompressible EPDM

Appendix B

Calibration of the viscoelastic material characterization setup

The additional mass off the system in Figure 2.15 is calibrated by comparison to the experimentally obtained modes on a 200mm beam excitation experiment. Given the location of the sensor, only odd modes can be found. These are depicted in Table B.1.

Mode	Frequency (Hz)
	109
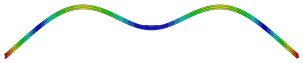	672
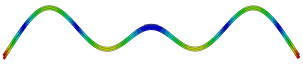	1858

Table B.1: Experimental modes for the excitation of a single beam

The point mass is placed in the middle of the piece in Figure 2.15. For $m = 17gr.$, Table B.2 shows the comparison between the experimental modes in table B.1 and the those of the numerical model.

Mode	Frequency
	109 109.02
	672 672.35
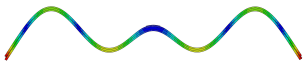	1858 1862.8
Maximal error	$\approx 0,3\%$

Table B.2: Experimental(black) and Numerical(blue) modes correlation for 200mm beam test

Appendix C

Experimental prototype for door seal transmission loss

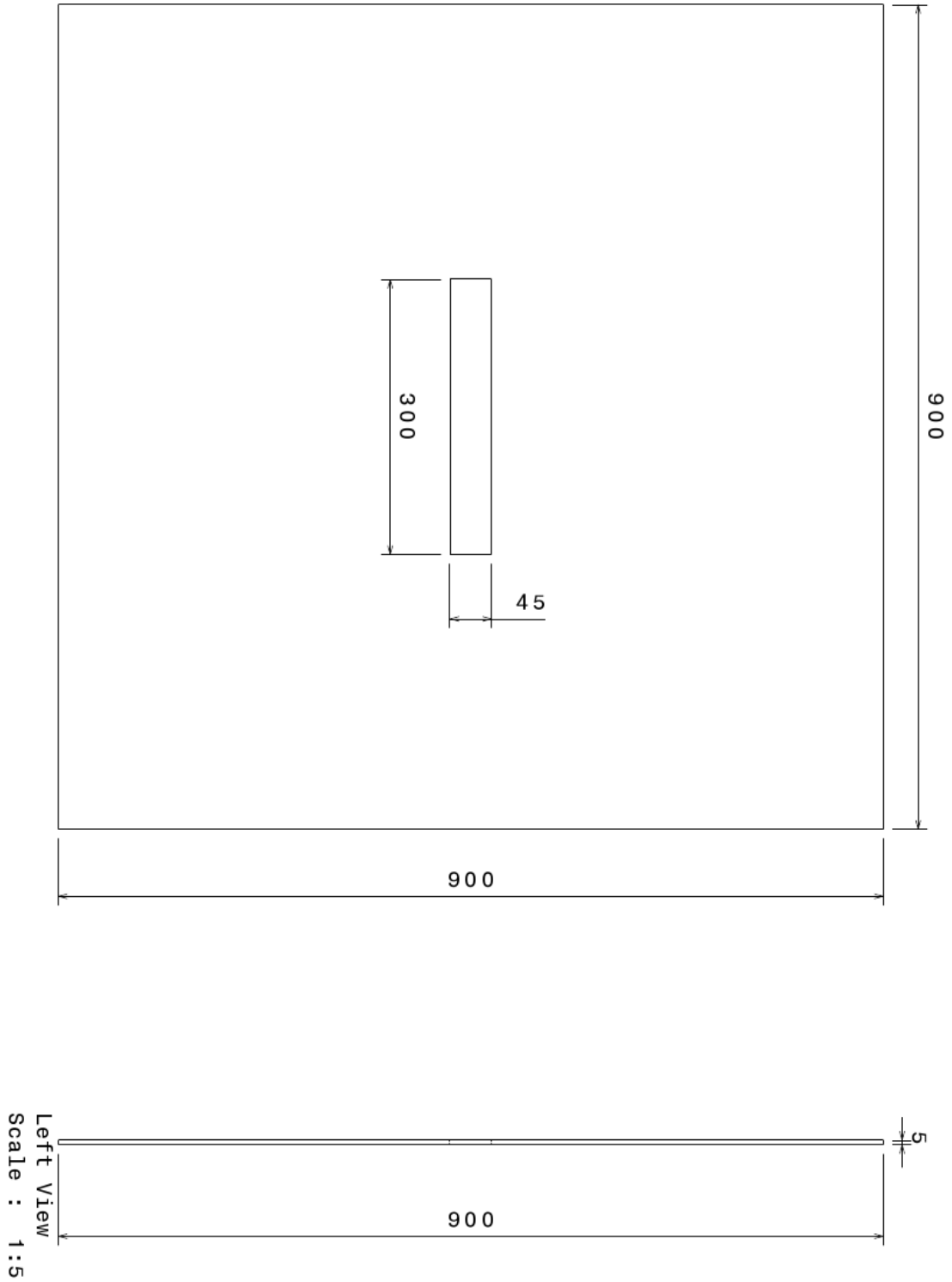

Figure C.1: Sketch of the plate-like part for the acoustic experiments with main dimensions

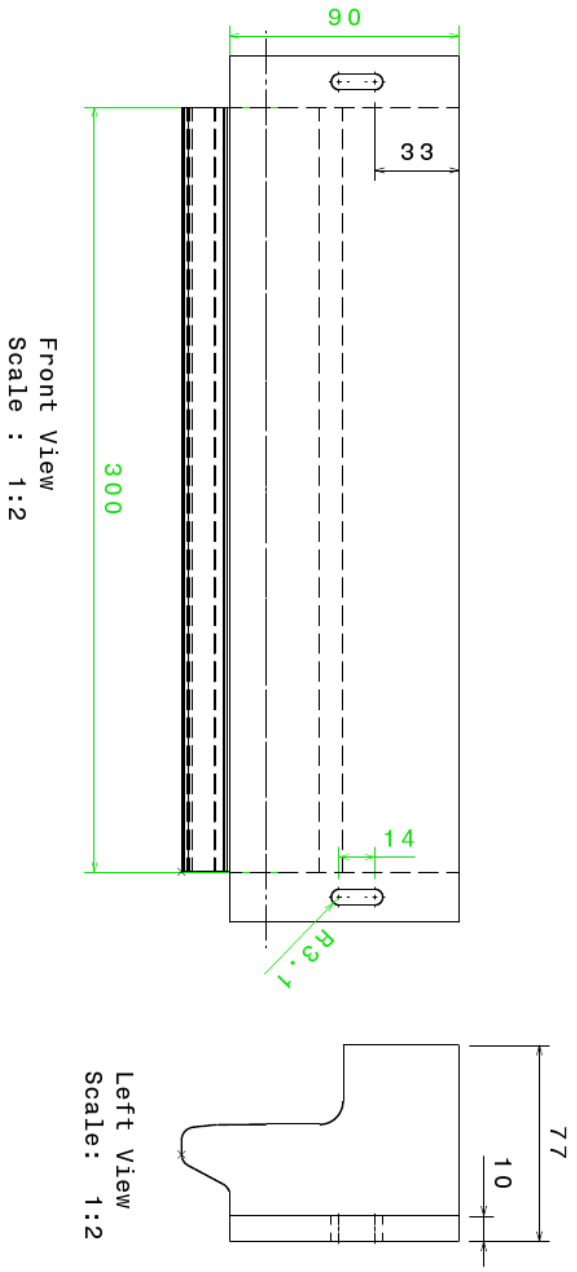

Figure C.2: Sketch of the part simulating the door for the acoustic experiments with main dimensions

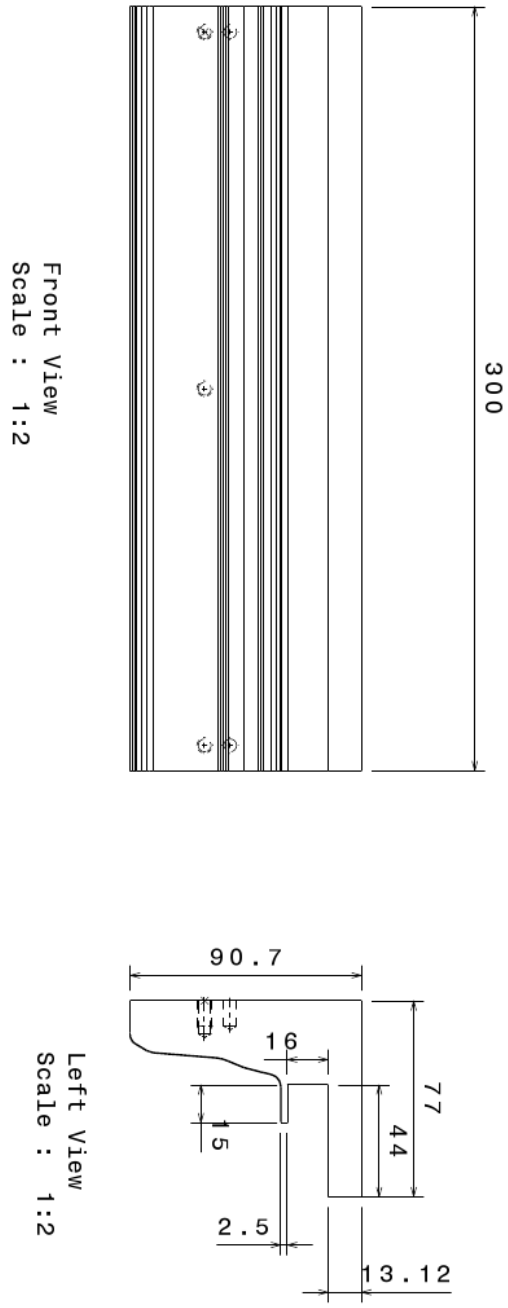

Figure C.3: Sketch of the part simulating the frame for the acoustic experiments with main dimensions

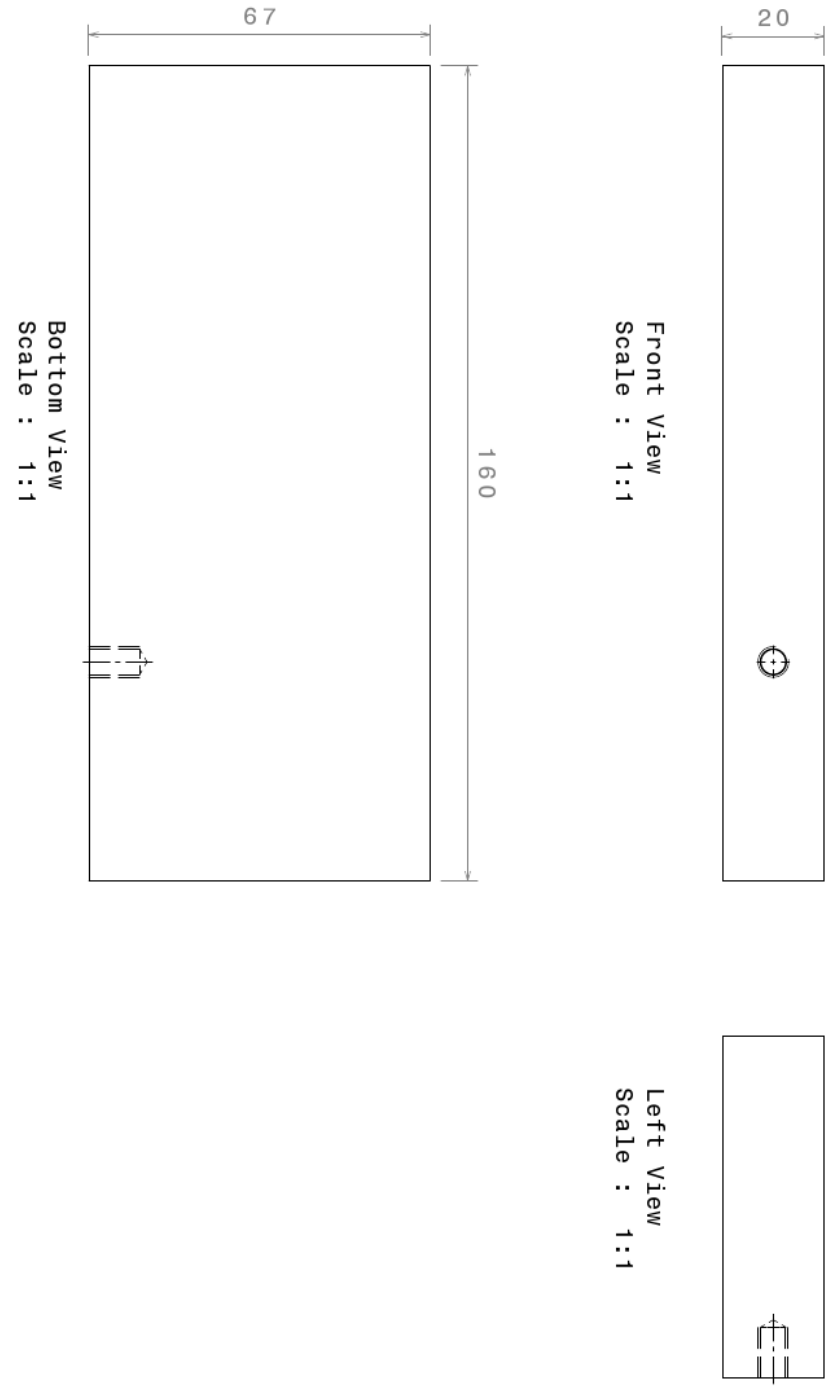

Figure C.4: Sketch of the door part guides for the acoustic experiments with main dimensions

Appendix D

Visibility solution

The implementation of the visibility coefficient introduced in equation 3.27 needs to take into account the 2 kinds of obstruction described in Section 3.1.3.

The first issue is easily solved by modifying matrix T so that

$$\begin{aligned} v_{ij} &= 1 \text{ for } \theta_i \in \big[-90, 90 \big] \\ v_{ij} &= 0 \text{ for } \theta_i \notin \big[-90, 90 \big] \end{aligned} \tag{D.1}$$

The second issue is more complex. Imagine a point M where the sound power is calculated, a source in a point P of the surface of the cavity, and an obstruction element E, composed of nodes E_1 and E_2 and different from the source element. We call θ_i the angle between MP, and the vertical axis, and α_1, α_2 the angles between respectively ME_1 and ME_2 with the same axis. This is schematized in Figure D.2. To determine if the energy from M to P is obstructed, we need to check every other element E in the cavity surface. If at least one of these elements is in the middle of the path between M and P, then there is no visibility between these points. The solution that we propose involves 2 conditions to determine if there is obstruction or not.

The first condition says that, in order for element E to be an obstacle between M and P, θ_i must be between α_1 and α_2. However, this necessary condition is not sufficient. It can happen that, although the angles satisfy said condition, the element checked for obstruction is further away from the point M than point P. In this case the visibility is not compromised, as can be seen in the left picture of Figure D.2. Another condition is thus necessary.

The second condition states that, if the first condition is satisfied, then if the angle between $P - E_1 - M$ is bigger than the angle defined by $E_2 - E_1 - M$, there will be obstruction and $v_{ij} = 0$. This condition is depicted in Figure D.2, where these angles are β_i and β_E respectively.

The problem with this approach is that for every point M it needs to check every element E of the surrounding cavity for every surface source P. This, if wrongly implemented, can increase time simulation importantly and calls, hence, for a very meticulous programming. However, once the cavity geometry is fixed, the visibility

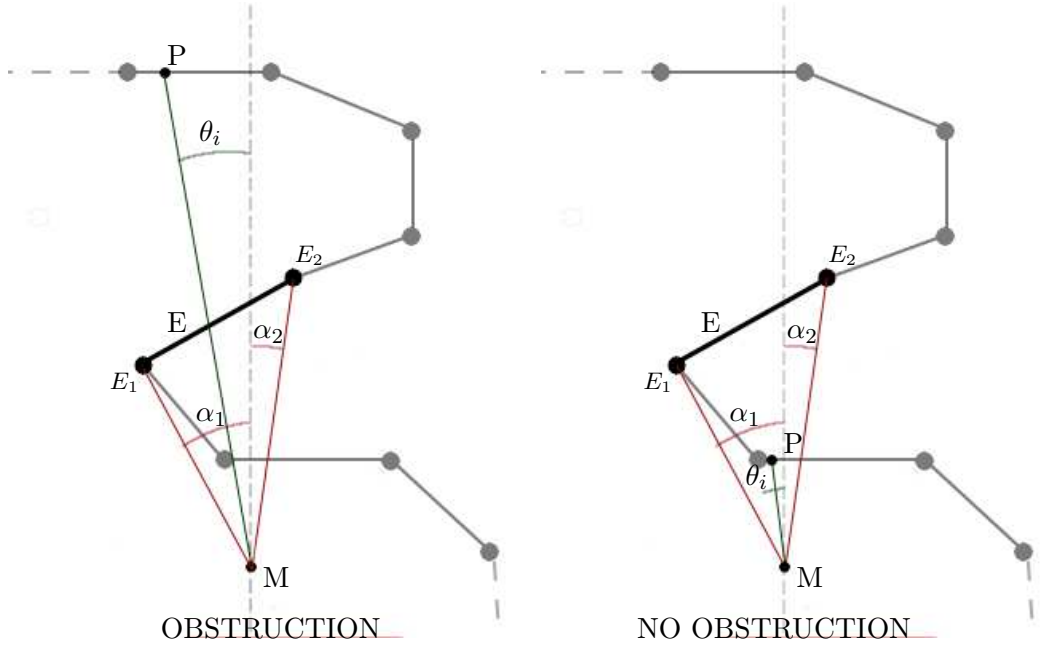

Figure D.1: First condition examples. Case where element E obstructs the energy flow between P and M (left) and case where it does not (right)

matrix does not change, and thus any modification of the primary sources or absorption coefficients can be implemented without need of recalculating this matrix.

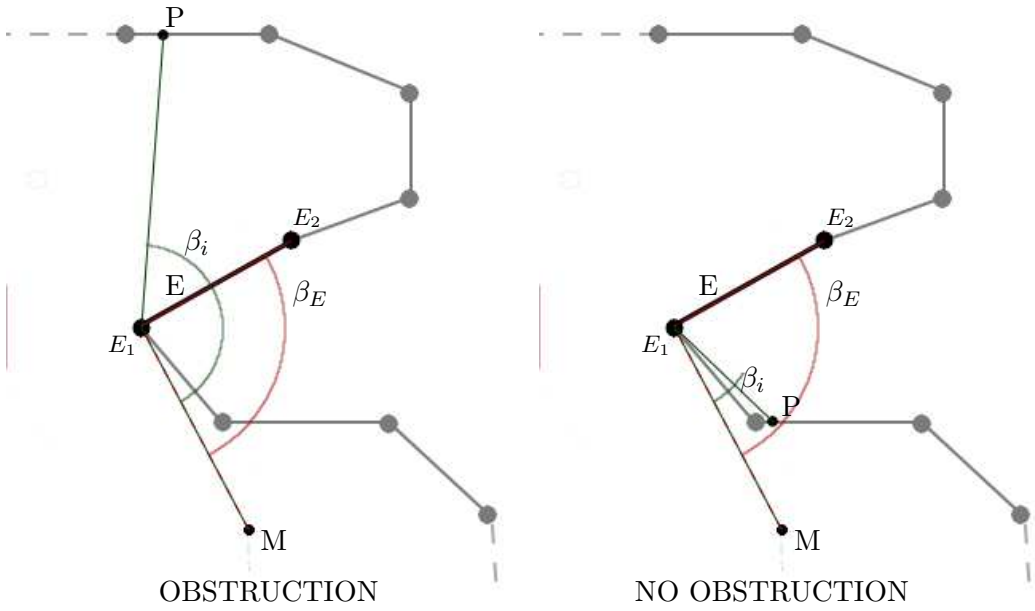

Figure D.2: First condition examples. Case where element E obstructs the energy flow between P and M (left) and case where it does not (right)

AUTORISATION DE SOUTENANCE

Vu les dispositions de l'arrêté du 7 août 2006,

Vu la demande du Directeur de Thèse

Monsieur L. JEZEQUEL

et les rapports de

M. A. LEGAY
Maître de Conférences HDR - CNAM - LMSSC Mécanique - case courrier 2D6R10
292 rue Saint-Martin - 75141 PARIS cedex 03

et de

M. C. PEZERAT
Professeur - Université du Maine - LAUM - Rue Aristote - 72085 LE MANS cedex 09

Madame OLIVER SERNA Clara

est autorisée à soutenir une thèse pour l'obtention du grade de **DOCTEUR**

Ecole doctorale MECANIQUE, ENERGETIQUE, GENIE CIVIL ET ACOUSTIQUE

Fait à Ecully, le 29 août 2016

P/Le directeur de l'E.C.L.
La directrice des Etudes

ECOLE CENTRALE DE LYON
Service Scolarité
ECULLY

M-A. GALLAND